Digital image analysis: predictive biomarkers for chemoimmunotherapy in malignant pleural mesothelioma

Author: Alexandra Hill (31089104)

Bachelor of Science (Biomedical Science Hons.)

THE UNIVERSITY OF WESTERN AUSTRALIA

National Centre for Asbestos Related Diseases
an Australian Research Cooperative

Declaration:

I Alexandra Hill, declare that this thesis is my own account of my research and contains as its main content work which has not previously been submitted for a degree at any tertiary education institution.

Alexandra Hill

21/10/2019

Abbreviations:

ADP – adenosine diphosphate

ATP – adenosine triphosphate

APC – antigen presenting cell

Bcl-xL – B cell lymphoma-extra large

CD – cluster of differentiation

CPS – combined proportion score

Cy5 – cyanine 5

DAMPs – danger associated molecular patterns

DAPI – 4',6-diamidino-2-pheylindole

DC – dendritic cell

DCR – disease control rate

DNA – deoxyribonucleic acid

DREAM – **D**u**R**valumab with first line ch**E**mother**A**py in **M**esothelioma with a safety run in.

FDA – federal drug administration (USA)

FFPE – formalin-fixed paraffin-embedded

FITC – fluorescein isothiocyanate

H&E – hematoxylin and eosin

HMGB-1 – high mobility group box -1

HRP – horseradish peroxidase

IASLC – international association for the study of lung cancer

ICD – immunogenic cell death

ICPB – immune checkpoint blockade

IHC –immunohistochemistry

IFN-γ- interferon gamma

IL – interleukin

ITIM – immunoreceptor tyrosine-based inhibition motif

ITSM – immunoreceptor tyrosine-based switch motif

JAK/STAT – janus kinase/signal transducers and activators of transcription

LDT – laboratory developed test

LED – light emitting diode

MAPK – mitogen-activated protein kinase

MHC – major histocompatibility complex

mRECIST – modified response evaluation criteria in solid tumours

NHMRC – national health and medical research council

NFAT – nuclear factor of activated T-cells

NLRP3 – nod-like receptor family pyrin domain containing 3

PFS – progression free survival

PRR – pattern recognition receptor

P2RX7 – P2 purinoceptor 7

RAS MEKERK – ras mitogen-activated protein kinase extracellular signal-regulated kinase

ROI – region of interest

ROS – reactive oxygen species

SCID – severe combined immunodeficiency

SHP-2 – src homology-2

TAM – tumour associate macrophage

TCR – t cell receptor

TMA – tissue micro array

TME – tumour microenvironment

TGF – tumour growth factor

TNF – tumour necrosis factor

TPS – tumour proportion score

TSA – tyramide signal amplification

ORR – overall response rate

OVA – ovalbumin

PD – progressive disease

PD-1 – programmed death – 1

PD-L1- programmed death – ligand 1

PD-L2 – programmed death – ligand 2

PI3K/Akt – phosphoinositide 3-kinase/protein kinase B

PR – partial response

MDSCS – myeloid-derived suppressor cells

MPM – malignant pleural mesothelioma

NF – $\varkappa$B –

NK – natural killer

NSCLC – non-small cell lung carcinoma

OS - overall survival

SD – stable disease

TILs – tumour infiltrating lymphocytes

TLR – toll-like receptor

TPS – tumour proportion score

Tregs – regulatory T cells

VEGF – vascular endothelial growth factor

ABSTRACT

Background:

Prognosis in MPM has remained poor, with median overall survival ~ 9 months. Immune checkpoint inhibitors (anti-PD-1/L1) have shown promising results, but only for a minority of patients', with response rates in mesothelioma ~ 15 – 20%(1). In other solid cancers, clinical outcomes have been improved by treating with a combination of chemotherapy and anti-PD-1/PD-L1.

Problem/solution:

While response rates to treatment improve in combined treatment, there remains a proportion of patients who still do not respond to treatment. Considering the potential for adverse treatment events, coupled with the substantive financial cost of treatment, it would be beneficial to predict patients most likely to respond to treatment.

Method:

Digital images analysis quantifies pre-treatment tissue biopsies of study participants (n=48). Slides are prepared using a TSA tagged multiplex immunofluorescent assay. A 5-panel of markers (CD8, PD-1, PD-L1, Cytokeratin and DAPI) identifies immune reactions that stratify SD and PR groups. Statistical analysis includes the mann u whitney test of difference for marker expression between clinical outcomes and the fisher exact test of association between PD-L1 and $CD8^{+}PD\text{-}1^{+}$ expression.

Results:

PD-L1 density on tumour epithelium is significantly different between SD and PR groups (p value 0.0214), as is the trend for % of PD-L1 expression (5% cut-off) between SD and PR groups (p value 0.0135). In the PR group there was a significant association between PD-L1 and $CD8^{+}PD\text{-}1^{+}$ and tumour types (Type 1 = $PD\text{-}L1^{+}HighCD8^{+}PD\text{-}1^{+}$, Type 2 = $PD\text{-}L1^{-}LowCD8^{+}PD\text{-}1^{+}$, Type 3 = $PD\text{-}L1^{+}LowCD8^{+}PD\text{-}1^{+}$ and Type 4 = $PD\text{-}L1^{-}HighCD8^{+}PD\text{-}1^{+}$)(p value = 0.009). In the PR group 87% of $PD\text{-}L1^{+}$ participants had high $CD8^{+}PD\text{-}1^{+}$ expression.

Conclusion:

The hypothesis generated is that patients demonstrating pre-existing "adaptive" immune resistance in the TME are more likely to respond the chemoimmunotherapy in MPM compared to patients who do not have pre-existing "adaptive" immune resistance. A potential predictive biomarker for chemoimmunotherapy in MPM is the $PD\text{-}L1^{+}HighCD8^{+}PD\text{-}1^{+}$ signature.

CONTENTS

1.0 INTRODUCTION/LITERATURE REVIEW

1.1 SUMMARY OF INTRODUCTION/LITERATURE REVIEW

The scope of literature reviewed was limited to the following:

- Malignant pleural mesothelioma (MPM) epidemiology and asbestos exposure.
- MPM histology.
- Clinical presentation and treatment.
- PD-1/PD-L1 axis mechanisms and influence on T cell signalling.
- T cell anergy.
- Previous and current immunotherapy (anti-PD-1/PD-L1) trials in MPM.
- Biological tipping point: initial non-responsive phase, pre-transitioned phase and new state phase.
- Quantification of the tumour microenvironment (TME).
- Inherent variability of PD-L1 as a biomarker
- Mechanisms of digital image analysis.

The review highlighted three key questions to answer:

1) Why are treatment response rates to immune checkpoint blockade (ICPB) poor in MPM?
2) Is it possible to identify those MPM patients in the pre-transitioned phase, that could be tipped into a new state phase in response to chemoimmunotherapy?
3) Should a 1% or 5% PD-L1 positive cut-off threshold be used and, should only PD-L1 expressed on tumour cells or PD-L1 expressed on both tumour and stromal cells be measured when used as a predictive biomarker?

This review addresses these three questions and a summary of the findings are as follows:

1) Three key causes attributed towards poor response to ICPB in MPM include:
    - Low mutation rates.
    - A “cold” TME
    - Adaptive immune resistance, also indicative of a supressed “hot” TME.

2) At the time of writing no studies had attempted to identify predictive biomarkers for patients likely to transition from a pre-transitioned state, into a new state in response to chemotherapy plus anti PD-L1 treatment in MPM.

3) A lack of consensus exists as to what the optimal thresholds and expression patterns are for PD-L1 as a predictive biomarker.

1.2 MPM AND THE CARCINOGENIC NATURE OF ASBESTOS

MPM is a rare, aggressive and incurable cancer arising from mesothelial cells lining the pleura of the lungs, caused by exposure to asbestos fibres(2). The commercial name asbestos refers to approximately 400 forms of naturally occurring mineral silicate fibres(3). Six of these forms are regulated including chrysotile (white asbestos), actinolite, amosite (brown asbestos), anthophyllite, tremolite and crocidolite (blue asbestos). These six forms are further divided into two structural types of asbestos: serpentine or amphibole. The serpentine structure includes only chrysotile made of curled fibres and is responsible for approximately 95% of asbestos products used globally(4). The remaining five fibres are slender, needle-like in structure and included in the amphibole group. Any form of airborne asbestos fibre can be inhaled, however only a small proportion of individuals exposed to asbestos go onto develop MPM(3)(5).

The amphibole-type fibres can migrate through the lung tissue, pierce the pleura and become embedded within the pleura space(3). Scavenging macrophages are incapable of fully engulfing these fibres due to their long length, macrophages resort without success to other elimination techniques(6). A constant cycle of irritation with production of ROS and IL-1β drives DNA damage with the breaking of strands and abnormal repair resulting in chronic inflammation(2)(7)(8). Failure of macrophages to clear the non-degradable asbestos fibres initiates a cascade of pro-inflammatory cytokines including VEGF(2). Cellular necrosis instigates the release of HMGB-1 into the extracellular matrix which recruit macrophages that in turn secrete inflammatory TNF-α to trigger NF-κB signalling, promoting oncogene activation and tumour suppressor gene deactivation(8). Chronic inflammation over several decades causes scarring, plaques, and increases the probability that malignant transformation of mesothelial cells will take place, the average disease latency period is approximately 40 years(2)(4).

1.3 ASBESTOS MINING AND CONSUMPTION IN AUSTRALIA

Australia by 1954 had the highest per capita consumption of asbestos cement products globally, and was the 4th largest gross consumer of asbestos after the U.S, U.K and France(9). The rate of MPM disease incidence in Western Australia is 4.5 cases per 100,000 people, well above the national average of 2.8 cases per 100 000 people(9). This is largely attributed to Wittenoon, a W.A mining town that closed in 1966, a mine that had predominantly produced crocidolite or “blue asbestos” the most

carcinogenic of the fibres(10). Asbestos consumption peaked in the mid 1970'-s and was all but phased out during the 1980'-s, however a complete ban on its importation and use was not implemented until 2003(10). The occupational nature of asbestos exposure makes it a male dominated disease at a ratio of 4:1, with women also having a more favourable prognosis(2).

1.4 GLOBAL ASBESTOS DISEASE INCIDENCE RATES

The International Agency for Research on Cancer reports MPM is responsible for 25,576 deaths globally, and disease burden remains substantial with 30,443 cases according to GLOBOCAN in 2018(11) Disease incidence rates per capita are highest in the U.S.A, U.K and Australia, but this is expected to change and be replaced with countries that have yet to ban asbestos(2). Asbestos consumption has been banned in 55 countries reflecting only 16% of the world's population(9). Countries yet to ban asbestos use include Russia, Kazakhstan, India, China, Brazil and other developing countries(5). It is estimated that the next 35 – 40 years the direct and indirect cost of MPM care in the U.S. alone will cost over $200 billion US dollars presenting a considerable public health issue(2)(12).

1.5 MPM SUBTYPES & HISTOLOGY

MPM is densely cellular, usually accompanied by stromal invasion and occasional necrosis(13). MPM can be further divided into epithelioid, sarcomatoid or biphasic subtypes according to the updated 2015 WHO classification(13). Epithelioid MPM accounts for ~ 60% of MPM cases and generally has a longer life expectancy with a median overall survival of approximately 13.1 months, histologically epithelioid cells appear oval, cuboidal or polygonal as seen in figure 1(2)(14)(15). The less common sarcomatoid subtype accounts for ~ 20% of MPM cases and has a worse prognosis, with a median overall survival of approximately 4 months(2)(14). Histologically, the sarcomatoid subtype contains solid sheets of spindle shaped cells as seen in figure 2, but may also contain lymphohistiocytoid cells and mimic mesenchyme tumours(13). The biphasic subtype accounts for ~ 20% of all cases and is a mixture of both the epithelioid and sarcomatoid subtypes within the same tumour as seen in figure 3(14). The sarcomatoid and biphasic subtypes tend to be less amenable to treatment(13).

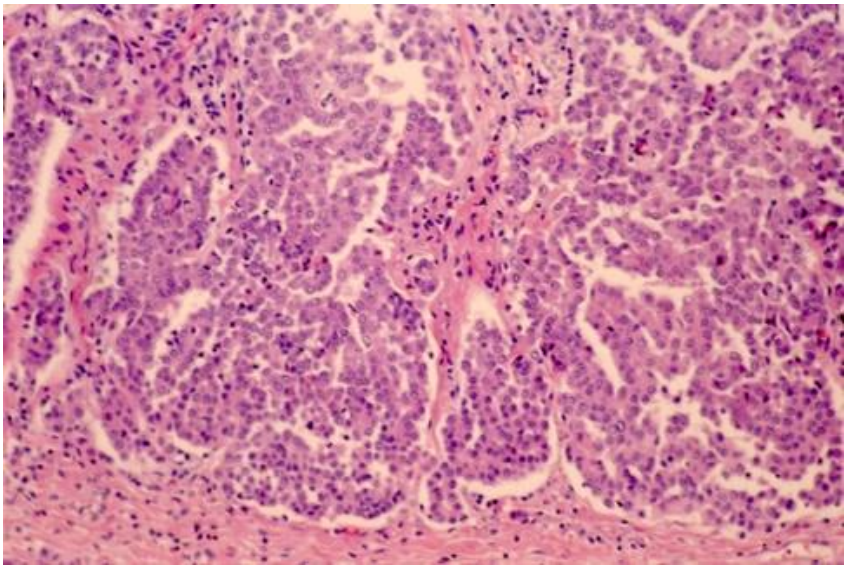

Figure 1. 20x magnification. Epithelioid histological subtype (H&E stain). Cuboidal cells forming papillo-tubular structures(16).

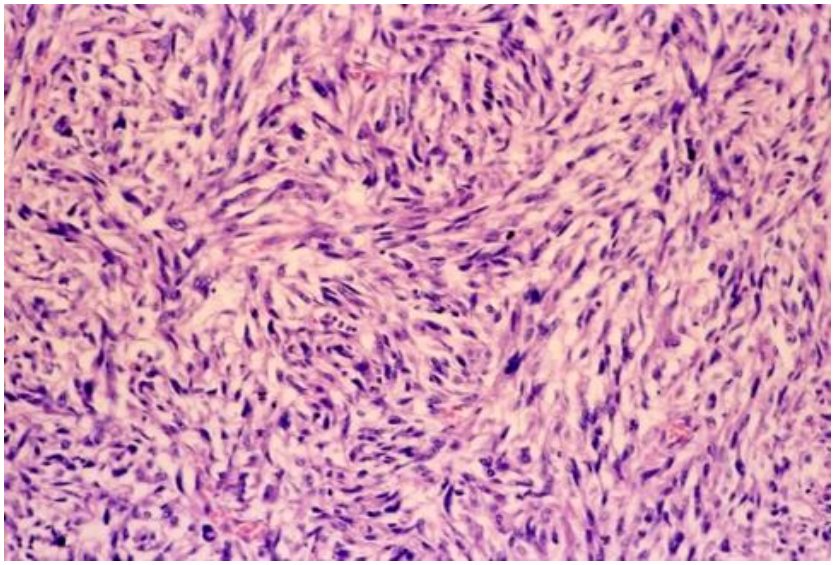

Figure 2. 20x magnification. Sarcomatoid histological subtype (H&E stain). Sheets of spindle shaped cells(16).

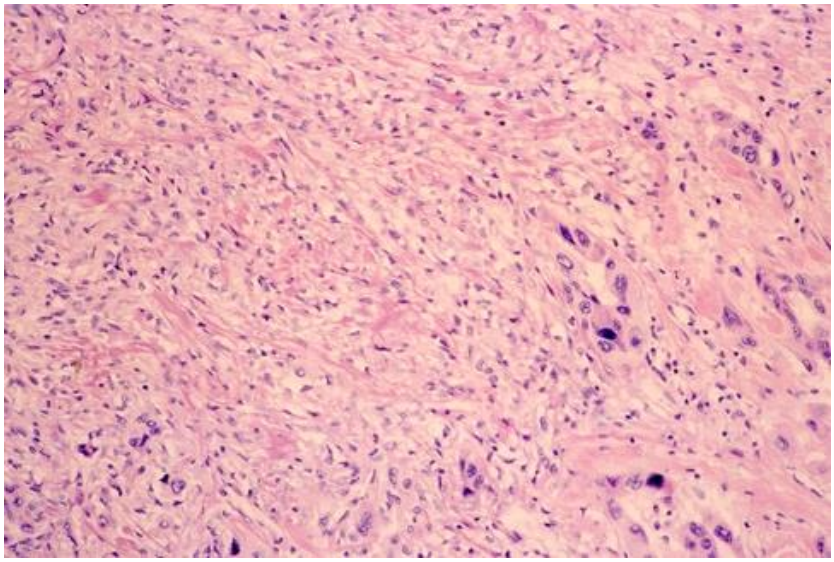

Figure 3. 20x magnification. Biphasic histological subtype (H&E stain). Hybrid of sarcomatoid and epithelioid histology(16).

1.6 CLINICAL PRESENTATION & TREATMENT

Clinically, MPM presents as either:

a) Diffuse MPM, this predominantly occurs in the epithelial subtype(2)(17).
b) A localised pleural tumour with or without effusion(2).

Effusion is diagnosed in 70% of patients and can fully encapsulate the lung, filling the pleural space and resulting in pain (2). Pleural thickening can occur causing shortness of breath due to restricted respiratory movement, pleuritic pain may arise from pleural irritation(2)(3).

1.7 SURGICAL INTERVENTION FOR MPM

Surgical intervention is rare and limited to healthy patients with early stage disease, only 10-15% of MPM meet eligibility requirements at time of diagnosis, as patients typically are not diagnosed until the later disease stages as symptoms are often misinterpreted(18)(19)(20). Surgery is controversial, as less than 15% of patients are alive 5 years post-surgery(3)(21). It was reported in a study that operating with the intention of cure had a median OS rate of 18 months (stage I: OS of 21 months, stage II: OS of 19 months, stage III: OS rate of 16 months and Stage IV: OS rate of 12 months) vs a median OS rate of 12 months with palliative intention(3). Two surgical procedures are available, the

more conservative pleurectomy which removes all visible disease from the lungs visceral and parietal pleura, and the radical extra-pleural pneumonectomy(3). The latter option removes all surrounding mesothelial tissue by removal of the pleura, lung, pericardium and diaphragm(2)(3).

1.8 RADIOTHERAPY

Radiotherapy is offered either palliatively or as an adjuvant to surgery or chemotherapy. Palliatively it can ease symptoms by reducing tumour bulk and side chest pain, by reducing the pressure of pleural effusions on nerve or blood vessels(2). Prophylactic radiation can delay metastases by preventing seeding and spread of tumour nodules along tracts, while radiation post-surgery can prevent seeding at the wound site(2)(3)(4). Radiation induced toxicity remains a concern, a phase II study showed 30% (27 MPM patients) suffered radiation associated pneumonitis(22).

1.9 CISPLATIN PLUS PEMETREXED: 1ST LINE TREATMENT

The current 1st line treatment for MPM is a chemotherapy platinum doublet of cisplatin plus pemetrexed, with the aim to reduce tumour bulk and alleviate symptoms(2). A study in 2003 by Vogelzang *et al*. of

456 chemotherapy naïve MPM patients was the first to provide statistical power. The study found median survival in the pemetrexed plus cisplatin arm was 12.1 months versus 9.3 months in the control arm of cisplatin alone(21). Initially toxicity rates were high, but with the addition of prophylactic dexamethasone plus folic acid supplements and vitamin B12 to the regime, toxicity became manageable(2)(4). The more recently completed randomized, phase III, MAPS trial, added bevacizumab to cisplatin plus pemetrexed(23). Patients were randomly assigned to either the pemetrexed, cisplatin and bevacizumab arm (PCB) (n = 223) or the cisplatin plus pemetrexed arm (CP) (n = 225). In the PCB arm OS was significantly longer with median OS of 18.8 months (CI: 15.9 - 22.6) compared to the median OS of 16.6 months (CI: 14.0 - 17.9) in the PC arm(23). The current 1st line treatment regime provides modest improvements to OS and has remained unchanged for the last 15 years. It is widely acknowledged throughout the field that new therapeutic options beyond chemotherapy need to be identified to treat MPM.

1.10 IMMUNE CHECKPOINT: PD-1/PD-L1 AXIS

1.10.1 T cell tolerance

The immune system distinguishes self-tissue from non-self-tissue, or self-tissue that has become mutated i.e. tumour cells(24). This occurs first in the lymph node and later in peripheral tissue during the T cell effector stage (25)(26). Central tolerance ensures self-reactive T cells with high avidity TCRs are eliminated, however some self-reactive T cells escape central tolerance and enter into the periphery were they are either deleted or tolerized into a state of T cell anergy(24)(25)(27). The PD-1/PD-L1 axis is a physiological checkpoint acting as a "brake" on the immune system, in a healthy host it modulates immune response duration and amplitude to prevent bystander tissue damage and autoimmune disease(28)(29)(30). This is done by promoting tolerance to self-antigens both during T cell induction in the lymph nodes and effector phase in the peripheral tissue respectively(25)(31). The immune checkpoint maintains equilibrium between peripheral tolerance and T cell activation(25). PD-1 receptor ligation on activated immune cells dampens that cells ability to attack tumour cells, studies show mice deficient in PD-1 lack peripheral tolerance and display features of autoimmune disease(26)(32).

1.10.2 Principle of ICPB: Mechanisms of action

Immunotherapy has changed the treatment landscape over the last decade with the translation of ICPB inhibitors from the laboratory into the clinic. Human monoclonal antibodies, anti PD-1 drugs (pembrolizumab and nivolumab) and anti PD-L1 drugs (durvalumab, atezolizumab and avelumab) block PD-1 and PD-L1 interaction. The success of immunotherapy relies on a key principle of tumour immunology, that activated cytotoxic T cells kill cancer(33). The blocking action provided by the ICPB inhibitors releases the "brakes" of the immune system, as seen in figure 4, enabling activated cytotoxic CD8 T cells to kill tumour cells.

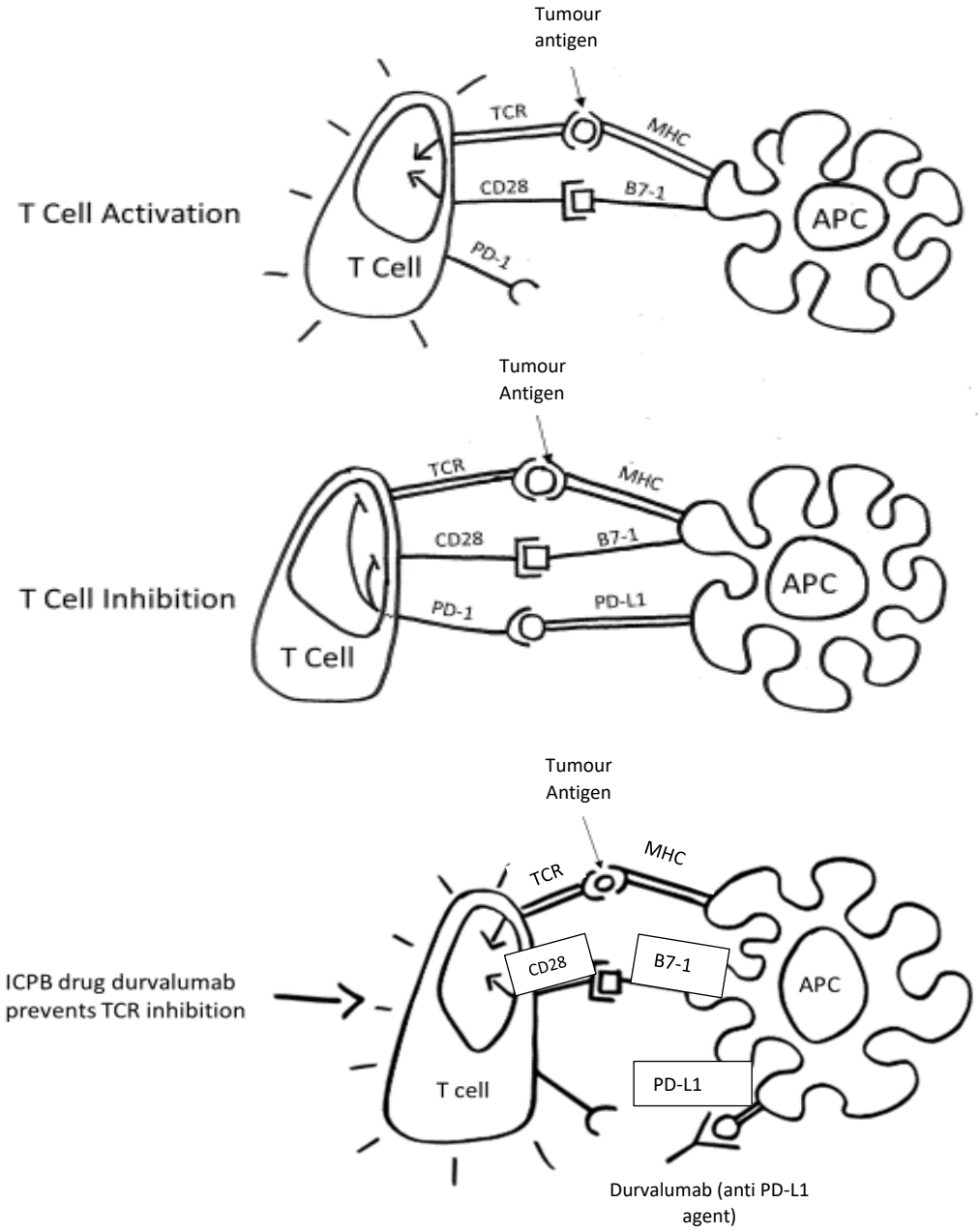

Figure 4. T cell activation requires 3 signals, tumour antigen presented on MHC to its respective TCR is signal 1, CD28 binding to B7-H1 is signal 2 & cytokines provide signal 3. T cell inhibition occurs by the binding on PD-L1 to PD-1 on the T cell, inhibiting TCR signalling and placing the "breaks" on the immune system. ICPB drugs, i.e. durvalumab block PD-1/PD-L1 binding, thereby releasing the breaks and preventing T cell inhibition(24)(33)(34).

1.10.3 PD-1 ligation in non-inflamed tissue is restricted to immune privileged sites.

PD-1 has two ligands PD-L1 (B7-H1) and PD-L2 (B7-DC), both are glycoproteins containing Ig C and Ig V domains(31)(34). PD-L1 expression, in normal physiology is absent from most tissues with the exception of the placenta, tonsil, heart, skeletal muscle and a small amount of macrophages in the

liver and lung(26)(28)(35). Minimal level PD-L1 mRNA can be detected in almost all tissue types(26)(34). The dominant ligand PD-L1 in response to inflammation can be expressed on a subset of macrophages, APCs, lymphocytes and epithelial and vascular cells in response to inflammation(6)(36)(37). PD-L2 is primarily expressed on activated macrophages and DCs in the spleen and lymph nodes and also binds PD-1, however its role within the immune context is not completely understood(25)(34).

1.10.4 PD-1 a marker of activated T cells.

PD-1 (CD279) a member of the CD28 family, is a type I trans-membrane protein transcriptionally induced on activated T cells, B cells, NK cells, monocytes and DCs, potentially PD-1 can be upregulated by gamma chain cytokines IL-2, IL-7, IL-15 & IL-21 (26)(28)(31)(32)(38)(39). PD-1 is not detected on resting T cells but once activated PD-1 appears on the T cell surface within 24 – 48 hours(27)(40)(41). Tsushima *et al*. demonstrated in a *in vivo* mouse model that PD-1 up-regulation occurs within 48 hours after naïve CD8 T cell activation, via cross-priming/presentation within secondary lymphoid organs(41). Naïve $CD8^+$ OT-1 TCR transgenic T cells were transferred into B6 mice, OT-1 T cells specifically recognize a restricted epitope of chicken OVA(41). Soluble OVA peptide was administered intravenously without adjuvant as a tolerogen(41). OT-1 T cells were not detected in peripheral blood until 72 hours after antigen administration, while OT-1 T cells in lymph nodes and spleen expressed high levels of PD-1 within 48 hours of antigen exposure(41). PD-1 expression even preceded early T cell activation markers CD25 and CD69(41).

1.11 T CELL ACTIVATION

1.11.1 T Cell activation requires 3 signals

T cell activation requires three signals, the first signal is induced by the precise binding of a specific antigen displayed on the MHC of an APC to a specific TCR(31). The second signal is a co-stimulation signal between the T cell CD28 and APC CD80 (B7-1) or CD86 (B7-2)(31). PD-1 on activated T cells can amplify the co-stimulatory signals CD28 and CD80/(B7-1) or CD86/(B7-2), if it is not blocked by PD-L1 and the third signal is provided by cytokines(42). The outcome of the PD-1/PD-L1 interaction is determined by the strength of T cell CD28 and TCR signals(26). If CD28/TCR signaling is increased, the T cell may be able to bypass the inhibitory repercussion of the PD-1/PD-L1 interaction at the activation stage(26). Accordingly, with no PD-1/PD-L1 interaction the TCR signaling threshold to activate T cells is lowered.

1.11.2 PD-L1 binding PD-1 inhibits TCR signalling pathway

PD-1 interacting with PD-L1 negatively regulates T cell activity at different stages of an immune response, through phosphatase activity, inhibiting the kinase signaling pathway responsible for T cell activation(36). The PD-1/PD-L1 axis generates inhibitory proteins that recruit SHP-2, a protein containing tyrosine phosphatases. There are two intracellular immune-receptors located in the PD-1 cytoplasmic tail, as seen in figure 5, including ITIM a tyrosine-based signal and ITSM formed by a c-terminal TEYATI sequence(32). SHP-2 binding to phosphorylated ITSM is pivotal in mediating PD-1 inhibition of the TCR(38). This occurs through reduced phosphorylation of ζ-chain-associated protein kinase 70, quashing the p13K/Akt and RAS MEKERK signaling pathways(32)(38)(43). This generates numerous downstream effects on the Bcl-xL and NFAT pathways, manipulating cell survival and proliferation causing an increase in anergic T cells characterized by poor IL-1 and IFN-γ production capabilities as a result of PD-1 ligation (31)(38)(43)(44).

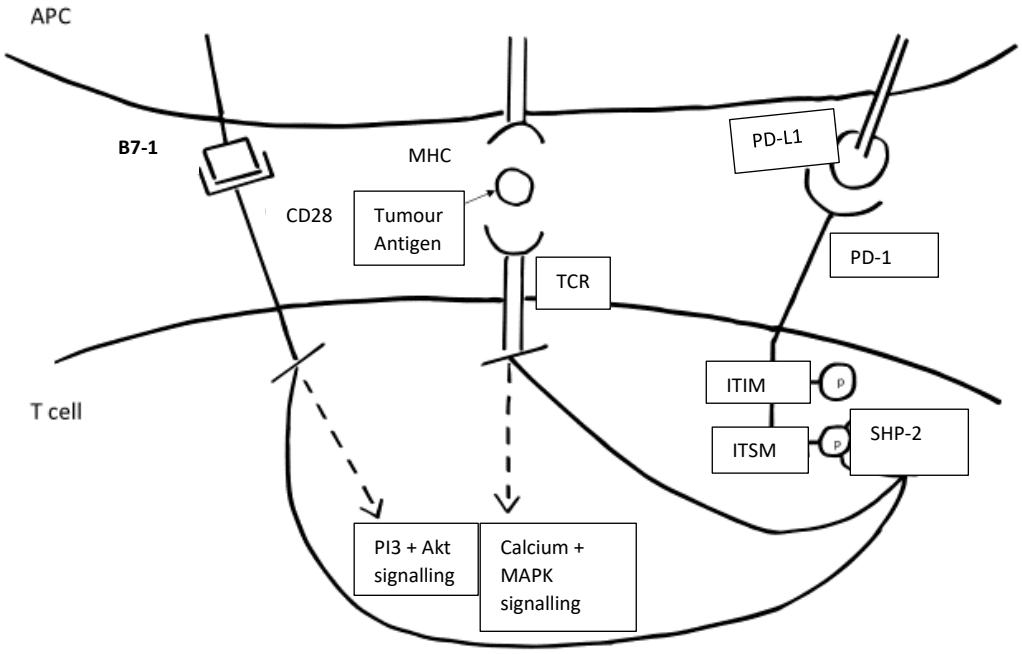

Figure 5. PD-1 binding PD-L1, generates inhibitory molecule SHP-2, dephosphorylating TCR signalling pathway molecules. Phosphorylation occurs in two intra-cellular immune receptors within the PD-1 cytoplasmic tail, including ITIM and ITSM, SHP-2 binds phosphorylated ITSM which triggers inhibition of TCR via quashing the p13k/Akt pathway and MAPK signalling(32)(39)(44).

1.12 CAUSES OF T CELL ANERGY

1.12.1 PD-1/PD-L1 Interaction

Previously described in section 1.10.

1.12.2 Cross-priming & cross-presentation between CD8 T cells and immature DCs

Classically, antigen is presented on MHC II molecules to CD4 helper T cells which then produce IL-2, IFN's and helper cytokines to activate CD8 cytotoxic T cells(45)(46). DCs can present internalised antigens on MHC I directly to CD8 cytotoxic T cells in a process known as cross-presentation(45). To optimally activate cytotoxic T cells, cross presentation needs to occur via mature rather than immature DCs. Mature DCs express the required co-stimulatory molecules CD80, CD86 and CD70 needed for complete T cell activation, "licensing" the CD8 T cell to kill tumour cells(46). Activated cytotoxic T cells secrete perforin/granzyme and cytotoxic cytokines lethal to tumours and also provide Fas-FasL

interaction(46). In the tumour draining lymph nodes, cross-priming of naïve CD8 T cells into effector T cells occurs via cross-presentation from mature DCs(46). Cytotoxic T cells migrate out of the LN and travel to the tumour site (47). Additionally cross-presentation of tumour antigen to CD8 T cells can occur in the TME by mature tissue resident DCs (27)(47). If a naïve T cell is presented tumour antigen from an immature DC this may induce T cell anergy as immature DCs lack the necessary co-stimulatory molecules(25). Tumour cells can also induce T cell anergy as they also lack the cell surface B7-1 molecules needed to provide a 2nd co-stimulatory signal, when presenting tumour antigen on MHC I(48). In non-immunogenic tumours such as MPM, DCs generally do not have the capacity to fully activate CD8 T cells, enabling tumours to remain protected from CD8 T cell attack(7).

1.13 ICPB RESPONSE RATES IN MPM PATIENTS

ICPB therapy in MPM produces a durable response in some patients, yet overall response rate remains low at ~ 9-20% as seen in table 1(6).

Table 1. Completed immunotherapy (anti-PD-1/PD-L1) clinical trials for MPM (15)(49)(50)(51)(52)(53)(54).

	Drug	Study	*n*	ORR (%)	OS months (median)	PFS months (median)	PR (%)	SD (%)
Anti PD-1	Nivolumab (BMS-936558)	NivoMeso. Single arm, phase II trial. Primary endpoint was DCR at 12 weeks. NCT02497508	34				24	24
		MERIT. Open-label, single arm, phase II trial. Primary endpoint was ORR according to mRECIST. JapicCTI-163247	34	29	17.3	6.1		
		MAPS 2. Randomised, parallel assignment, open-label phase II trial. Primary endpoint was DCR at 12 weeks. NCT02716272	54	19		5.6	27	26
	Pembrolizumab (MK-3475)	KEYNOTE-028. Non-randomised, open-label, phase 1b trial. Primary endpoint was ORR. NCT02054806	25	20		5.4	20	52
		Chicago-Phase II. Open-label trial. Primary endpoint was ORR in a PD-L1 positive population. NCT02399371	64	19	11.5	4.5	19	47
Anti PD-L1	Avelumab (MSB0010718)	JAVELIN. Phase 1b, open-label. Dose escalated trial. Primary endpoint was best ORR according to mRECIST. NCT01772004	53	9	10.7	4.1	12	
Anti PD-L1 & Anti CTL-4	Nivolumab (anti-PD-L1) & Ipilimumab (anti-CTL4)	INITIATE. Single arm, phase II trial. Primary endpoint was DCR at 12 weeks. NCT03048474	34				29	38

Table 2. Current immunotherapy trials (anti-PD-1/PD-L1) recruiting MPM participants.

	Drug	Study	n
Anti PD-1	Pembrolizumab (MK-3475)	Single group assignment, open-label, evaluating predictive biomarkers in solid tumours. Estimated completion, April 2023. NCT02628067	1350
	Pembrolizumab (MK-3475) versus standard chemotherapy	PROMISE-meso. Phase III, randomised, parallel, open-label trial. Estimated completion, December 2020. NCT02991482	144
Anti PD-L1	Atezolizumab (MPDL3280A)	Phase II, open-label, multi cohort study in advanced solid tumours. Estimated completion, December 2019. NCT02458638	477

1.14 Why are response rates to ICPB low in MPM?

A review of the literature identified three key potential causes for poor patient response to ICPB in MPM, including low tumour mutation rates, a "cold" TME and IFN-γ induced adaptive immune resistance. These are all tumour-driven mechanisms to avoid destruction by the immune system.

1.14.1 Immunosurveillance Theory

Studies using SCID and athymic mice show a depleted T cell population is associated with a higher frequency of cancer, underscoring the pivotal role T cells play in immunosurveillance(27). The immune system recognizes and eliminates pre-malignant and early malignant cells through three phases of immunosurveillance, the elimination phase, equilibrium phase and escape phase(31)(40). In the initial elimination phase, immunogenic tumours that have developed from abnormal genes or tissue repair processes are detected, the immune system responds with cytotoxic lymphocytes to eliminate the abnormal cells(40)(55). The equilibrium phase is period of latency, in cancers such as MPM it can last decades, the tumours status quo is upheld, maintaining immune mediated balance between pro-tumour and anti-tumour cells within the TME(6)(55). Towards the end of the equilibrium phase the TME increasingly becomes pro-tumour, this allows malignant cells to avoid immune system attack and enter into the escape phase(56). In this final escape phase, the TME has been tipped away from an anti – tumour environment to a pro – tumour environment that facilitates tumour metastases.

1.14.2 Low tumour mutation rate

A low tumour mutation rate can hamper the immune system's ability to launch an effective immune response against the tumour(27). It has been suggested that ICPB therapy provides limited success in MPM due to the tumours low mutation rate(57). MPM, as seen in figure 6, has relatively low frequency of 0.79 mutations per mega base, compared to other environmental carcinogenic tumours i.e. lung cancer and melanoma (58)(59).

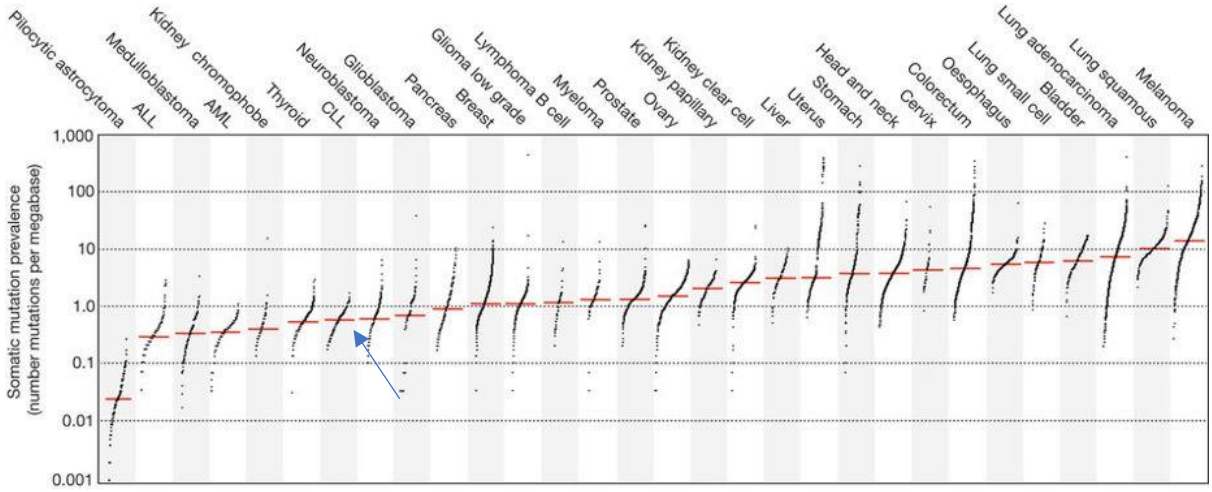

Figure 6. Figure adapted from Alexandrov et al. showing somatic mutations per megabase across tumour types, MPM has 0.79 mutations per megabase and its position is indicated by the blue arrow(59).

1.14.3 TME favoring a "cold" tumour

The TME is broadly either "hot" (inflamed) providing an anti-tumour environment or "cold" (non-inflamed) supporting a pro-tumour environment. Inhibitory and stimulatory signals of varying ratios comprise the tumour milieu, reflecting the host's immune status.

Hot tumours are generally distinguished by:

- Pre-existing cytotoxic CD8 T cells(60).
- Tumour PD-L1 expression induced by IFN-γ, in contrast to the non-IFN-γ induced PD-L1 expression seen in cold tumours(61).

- Type 1 macrophages that secrete proinflammatory cytokines (44).
- An abundant concentration of type I IFNs that aid DC maturation, cross priming of CD8 T cells, tumour cell MHC I expression and enhancement of NK cell function(7).

Positive correlations have been shown between CD8 T cell frequency and OS in MPM, lung, breast, melanoma, colorectal and brain cancer(27). Theoretically tumour infiltration of cytotoxic CD8 T cells should successfully eliminate the tumour, however this can be prevented by the immunosuppressive factors on the TME(44).

Tumour cells and associated APCs contain high concentrations of inhibitory molecules that can directly activate CD8 T cells and induce the anergic phenotype(27). MPM typically are cold tumours with highly immunosuppressive cell types including:

- Tregs
- Anergic T lymphocytes
- MDSCs
- TAMs
- Type 2 macrophages(14)(62)

Natural Tregs, differentiated in the thymus are part of central tolerance preventing autoimmunity, whereas secretion of TGF-β from tumour cells converts naïve T cells into "adaptive" Tregs in peripheral tissues or blood(63)(64). Tregs aggregate and form a barrier around DCs to prevent any interaction with T cells and hinder antigen presentation(65). MDSCs dampen CD8 T cell anti-tumour activity, through inhibiting the TCR – ξ chain(64). In response to IL-4, macrophages can become alternatively activated into type 2 macrophages and carry out immune regulation and tissue remodeling and repair(63). TAMs closely resemble type 2 macrophages and also show defective NF-$\varkappa$B activation in the presence of pro-inflammatory cytokines(44)(63). Stromal TAMs produce matrix metalloproteases which degrades the extra cellular matrix, this entices endothelial cell growth and migration resulting in angiogenesis to support tumour cell growth(63). Ectonucleotidases CD39 and CD73 can be expressed on the surface of tumour cells, metabolizing ATP to ADP and finally to adenosine which halts the trafficking and function of CD8 T cells in the tumour(44). A mechanism by the tumour to halt T cell activation and impair immunosurveillance.

1.14.4 Adaptive immune resistance vs innate immune resistance

PD-L1 expression can be stimulated by IFNγ, IFNα, IFNβ, IL-4, IL-10, VEGF, granulocyte macrophage colony stimulating factor and bacterial lipopolysaccharide(28). IFN-γ potently induces PD-L1 on tumour cells, suggesting tumour cells detect raised levels of IFN-γ in the TME and interpret it as a danger signal(6)(25). The tumour responds through a negative feedback loop by increasing expression of PD-L1(66). Protracted immune stress can cause PD-L1 expression on both tumour cells and immune cells in the TME. Inflammatory INF-γ released from CD8 effector T cells induces PD-L1 expression via the JAK/STAT signaling pathway(42). PD-L1 upregulation on melanoma cells was found to be dependent on CD8 T cells and IFN-γ in the TME, indicating that PD-L1 expression may be driven by the active immune system of a "hot" tumour(25). A theory further supported by Senol *et al*. who studied melanocytic lesions using laser - capture microdissection at the invasive tumour margin and found expression of IFNγ mRNA correlated with tumour PD-L1 expression(28). Additionally, Taube *et al*. detected IFNγ at the interface of PD-L1^{+} tumours but not in PD-L1^{-} tumours(34). These findings all support the notion that PD-L1 expression is a negative feedback mechanism directed by the tumour(34).

It is widely acknowledged that PD-L1 expression on tumour cells is due to either "adaptive immune resistance" in response to IFN-γ or "innate immune resistance" in response to oncogenic signaling(60)(67). PD-L1 provides a "shield", protecting tumour cells from to attack by cytotoxic CD8 T cells of the adaptive arm of the immune system(28). Tumours with constitutive PD-L1 expression due to "innate immune resistance" often are associated with higher levels of organized peritumoural stromal tissue that provides a physical barrier between the tumour and T cells(68). The prevailing notion is that ICPB therapy will be successful in patients whose PD-L1 expression is the result of immunogenic "adaptive immune resistance" (28)(49)(68)(69). Patients whose TME lacked immune infiltrates were found to be non-responsive to ICPB therapy compared to patients with immune rich tumours in NSCLC and melanoma(68). It has been shown that improved patient outcomes to ICPB therapy require pre-existing CD8 T cells negatively regulated by the PD-1/PD-L1 axis at the invasive tumour margin(14)(30)(33)(60). Response rates to ICPB in MPM have remained low, suggesting that ICPB alone is not enough to generate a response in MPM.

1.15 TIPPING POINT

ICPB therapy elicits a response in some but not all patients. Lesterhuis *et al*., refers to an ecology systems model, in which patients undergoing treatment will be in one of three phases:

1) Initial non-responsive phase (no response to treatment).
2) Pre-transitioned phase (could/could not respond to treatment).
3) New state phase (responds to treatment)(70).

This model assumes patients will either respond or not respond to treatment. Patients in the initial non-responsive phase and the new state phase have their outcome to treatment pre-determined, but those in the pre-transitioned phase may either respond or not respond to treatment. The factor instigating change may be very small, but significant enough to tip patients out of the pre-transitioned state into the new state phase(70). The likelihood that patients will respond to treatment increases the closer a patient is to the tipping point, which once reached will see the patient move from the pre-transition phase to a new state phase.

To increase patient response to treatment two key questions, need to be addressed:

a) How do you to identify patients in the pre-transitioned phase?
b) What can be done to tip those patients in the pre-transitioned phase into a new state phase?

1.16 WHAT CAN BE DONE TO TIP PATIENTS FROM THE PRE-TRANSITIONED PHASE TO TRANSITIONED PHASE?

1.16.1 Chemoimmunotherapy may prevent T cell anergy

Chemotherapy given in conjunction with immunotherapy can generate immunogenic cell death (ICD) which in turn can activate immature DCs to become mature DCs, and potentially avert T cell anergy. Tsushima *et al.* showed that in addition to blocking the PD-1/PD-L1 interaction with antibodies, antigen signaling was required to break T cell anergy, as treatment with anti-PD-1/PD-L1 in the

absence of peptide did not elicit a response(41). These results support the notion that unless chemotherapy is given prior to or during immunotherapy to generate ICD, immunotherapy will not work in non-immunogenic "cold" tumours (41). Anti-PD-1/PD-L1 drugs block early phase tolerance occurring in the lymph nodes by blocking PD-L1 expressed on APCs. In this scenario naïve CD8 T cells are cross-primed and leave lymph nodes fully "licensed" as effector T cells, not anergic cells. Late phase tolerance is prevented from occurring as PD-1 expressing T cells, B cells, N.K. cells are prevented from binding to PD-L1 on the surface of any remaining tumour cell clusters due to the blocking action of ICPB inhibitors.

1.16.2 ICD

Historically, it was thought that chemotherapy induced immunogenically silent tumour cell death(71). Certain chemotherapies elicit ICD and unlike physiologically programmed cell death which promotes tolerogenic cell death, ICD can launch a fully activated cytotoxic CD8 T cell response to kill tumour cells(72). Chemotherapy induced ICD can drive the translocation of specific intracellular components known as danger associated molecular patterns (DAMPs) to the outer cell membrane or into the extracellular matrix(73). A DAMP binding to its respective pattern recognition receptor (PRR) provides the maturation signaling needed to activate immature DCs(47). PRR binding to its associated DAMP activates inflammasome NLRP3 triggering IL-1β secretion by DCs and activation of IFN-γ secreting CD8 T cells(73). The now fully activated DC can provide a co-stimulatory signal strong enough to fully activate CD8 T cells when presenting engulfed tumour antigen on MHC I to the TCR(25). TLR signaling promotes antigen presentation and Type I IFN production and prevents T cell anergy(74).

Three key DAMPs shown in figure 7 generate ICD including HMGB-1, extracellular ATP, and endoplasmic reticulin stress induced calreticulin exposure(47). The ubiquitously expressed non-histone binding protein HMGB-1 regulates gene transcription and DNA repair to stabilizes nucleosomes(71)(75). HMGB-1 is translocated from the nucleus to cytoplasm and then passively released into the extracellular matrix during the late stage of cell death(76). HMGB-1 binds to TLR4 on DCs enhancing antigen presentation by DCs and production of IL-1β to activate cytotoxic CD8 T cells(71)(76). Intracellular ATP released during mechanical stress from dying tumour cells into the extracellular space both attracts immune cells to the tumour site and activates the inflammasome pathway(71). Extracellular ATP binds to PRR purinergic receptor P2RX7 on DCs, aiding recruitment and differentiation of monocytes and DCs in the TME (25)(73). Immature CD8αCD134^{+}DCs recruited

to the tumour site due to extracellular ATP, engulf dying cells and at the same time receive maturation signals necessary to activate anti-tumour activity(71)(72). The maturation signals occur with binding of extracellular ATP to the P2RX7 receptor, a potent activator of the NLRP3 inflammasome pathway in DCs and macrophages(71). The protease caspase-I is activated by the NLRP3 pathway resulting in the secretion of mature pro-inflammatory cytokines IL-1β and IL-1α which activates CD8 cells (57)(71).

The soluble protein calreticulin acts as a chaperone regulating Ca^{2+} in the lumen of the endoplasmic reticulin and aids in assembling MHC I molecules(75). Physiological stress induced by increased demands on the proteins secretory load can lead to endoplasmic reticulin stress, causing the translocation of calreticulin to the plasma membrane, and its very presence serves as a signal to be engulfed by DCs(71)(72)(75).

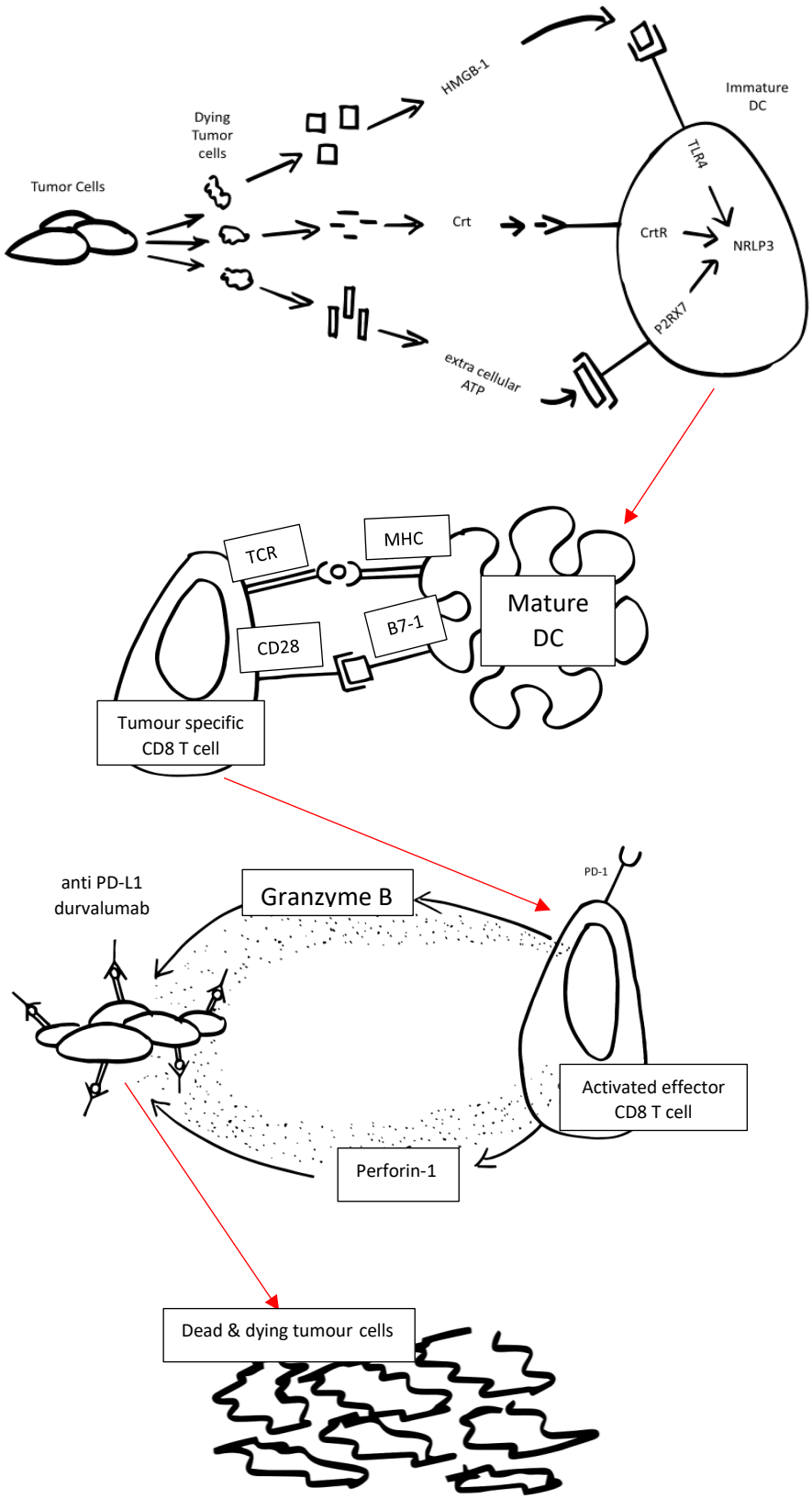

Figure 7. Chemotherapy induces release of DAMPs from dying tumour cells that bind to their respective PRRs on immature DCs, triggering mature DCs to induce an effector CD8 T cell response to lyse tumour cells(57)(71)(73).

1.17 CISPLATIN MECHANISM OF ACTION

Cisplatin upregulates mannose-6-phosphate receptor expression on the extracellular membrane of tumour cells causing an increase in the membranes permeability to granzyme-β, a serine protease realized from cytotoxic lymphocytes(77)(78). The drug inhibits cell proliferation by entering the cell and forming reactive platinum complexes that promote intra strand DNA crosslinks damaging the DNA and resulting in cell cycle arrest(75)(79). Cisplatin can encourage tumour cell death by abrogating Treg and MDSC activity through increased MHC I expression on tumour cells and boosting the number of $CD11^{+}$ DCs in tumour cells capable of inducing tumour specific cytotoxic lymphocytes(73)(80).

1.18 PEMETREXED MECHANISM OF ACTION

Pemetrexed is a drug noted for its anti-tumour activity in MPM, a cancer generally considered to be chemotherapy resistant(81). The antimetabolite drug deprives folate carries of the enzymes required for formation of precursors purine and pyrimidine, thereby preventing RNA and DNA synthesis(82). The drug gains cell entry via a reduced folate carrier and once inside switches into a polyglutamated form to aid retention and increase the drug's half-life (81). Marq *et al*. demonstrated in an immunodeficient mouse model that pemetrexed works through activation of CD8 T cells rather than direct killing of tumour cells(83). It has been reported that pemetrexed can increase TIL leukocytes, enhanced antigen presentation and reduce the frequency of MDCS, and in pancreatic cancer activate IFN-y producing NK cells(79)(84).

1.19 DAMPS RELEASED BY CISPLATIN PLUS PEMETREXED

Schaer *et al*. showed pemetrexed *in vitro* instigated a strong release of HGMB-1 in MC38 and Colon26 tumour cells (84). Cisplatin is widely reported as a trigger for the release of extracellular ATP and HMGB-1, however it does not produce endoplasmic reticulin stress induced calreticulin (85). There is a lack of consensus within the field about what defines ICD, with several studies siting that *bona fide* ICD requires extracellular ATP, HMGB-1 and endoplasmic stress induced calreticulin(71)(85). As cisplatin does not generate endoplasmic reticulin stress induced calreticulin it is claimed by some not to generate true ICD(72). However the release extracellular ATP and HGMB-1 have been shown to

generate immune responses(71). To date no reports in the literature show that pemetrexed produces extracellular calreticulin, however pemetrexed has been reported as inducing endoplasmic reticulin stress in human esophageal squamous carcinoma cells(82). Interestingly, a recent study by Xu *et al*. showed cells acquiring chemotherapy resistance in MPM displayed low levels of endoplasmic reticulin stress(86).

1.20 BEST OF BOTH WORLDS: CHEMOTHERAPY AND IMMUNOTHERAPY TRIALS

Chemotherapy can work in synergy with immunotherapy, combining the high initial response rates of chemotherapy with the more durable long-term response of immune checkpoint blockade (25)(73). Results in the field have been promising, higher proportions of patients are responding to combined treatment compared to immunotherapy alone(73). Responses to treatment have been witnessed in cancers previously thought not to be susceptible to immunotherapy i.e. thoracic cancers(25). It has been hypothesized that chemotherapy-induced lymphocyte depletion may allow the reconstitution of a new T cell population following chemoimmunotherapy(46). After the first few cycles of chemotherapy, there is an increase in cytotoxic CD8 T cells and a reduction in immunosuppressive Tregs (46). An opportunity exists at this point to incorporate immunotherapy to remold a new cellular population and tip the TME into a “hot” environment favouring durable cytotoxic CD8 T cells.

Table 3. Active combined chemotherapy & immunotherapy (anti-PD-1/PD-L1) trials in MPM.

Drugs	Description	*n*	Start & estimated completion
Nivolumab (anti PD-1), cisplatin & pemetrexed.	Phase II. Multicentre Japanese trail. Testing efficacy of nivolumab with current 1st line treatment in unresectable MPM.	18	Commenced January 2018.
Pembrolizumab (anti PD-1), cisplatin & pemetrexed.	Phase II/III, randomised, parallel assignment in advanced MPM. Cisplatin/pemetrexed arm. Cisplatin/pemetrexed/pembrolizumab arm. Pembrolizumab arm (phase II). NCT02784171	126	Commenced October 2016. Estimated completion February 2021.
Atezolizumab (anti PD-L1), cisplatin, pemetrexed and surgery with/without radiation.	Phase I, single group, open-label interventional study in MPM. NCT03228537	28	Commenced November 2017. Estimated completion June 2020.
Durvalumab (anti PD-L1), cisplatin & pemetrexed.	Phase II, non-randomised, open-label study in unresectable MPM. NCT02899195	55	Commenced June 2017. Estimated completion December 2020.
Durvalumab (anti PD-L1), cisplatin & pemetrexed.	DREAM. Phase I/II non-randomised, open-label study in unresectable MPM. ACTRN12616001170415	54	Commenced November 2016. Estimated completion October 2019.

The DREAM trial described in table 3 is one of two studies, and the first Australian study to combine chemotherapy and durvalumab to treat MPM(87). In the U.S.A a similar independent study phase II study, MED14736 (NCT02899195), commenced in June 2017 also combined durvalumab with cisplatin plus pemetrexed, also measuring overall survival in 55 MPM patients.

1.21 PD-L1 AS A BIOMARKER

To date, the most widely studied predictive biomarker in MPM and cancer in general has been PD-L1, in MPM PD-L1 expression is found in 16 – 65% of patient biopsies(14). High PD-L1 expression in the absence of treatment is generally associated with poor prognosis(14)(88). High PD-L1 expression is also predictive for response to anti-PD-1/PD-L1 monotherapy treatment in MPM and a number of other cancers (89). The only FDA approved treatment requiring positive PD-L1 expression (>50% TPS) is pembrolizumab for the 1st line treatment of metastatic NSCLC(90). Pembrolizumab in combination with carboplatin plus pemetrexed is approved as a 1st line treatment for metastatic NSCLC regardless of patient PD-L1 expression(90). Interestingly in combined chemotherapy/ICPB therapy PD-L1 has been shown to no longer be predictive(91).

There is a great deal of discordance in published data and concerns have been raised within the literature about the suitability of PD-L1 as a biomarker for cancer. This is chiefly because some PD-L1$^-$ tumours respond to anti-PD-1/PD-L1 treatment while many PD-L1$^+$ tumours remain unresponsive(35)(92)(89). There are four FDA registered PD-L1 IHC assays that use four different PD-L1 antibodies (22C3, 28-8, SP263 and SP142) across two different platforms (DAKO and VENTANA) with each employing their own scoring system(90). The Blueprint project, an initiation of the international association for lung cancer, compared commercially available PD-L1 assays and found that 37% of published results would have be given a different PD-L1 classification depending on the assay and scoring system used(93). The variability of antibody clones and platforms used for each approved anti-PD-1/PD-L1 treatment hinders comparisons across clinical trials.

1.21.1 Key issues surrounding PD-L1 as a biomarker:

- Heterogeneity: acquisition of a representative tumour sample reflecting a patients PD-1/PD-L1 profile is problematic (49)(89)(90). Solid tumours contain micro niches with varying levels of perfusion and oxygenation, within each niche are microenvironments composed of a dominating cell type for that microenvironment(29). PD-L1 expression varies over time and amongst and within tissues samples, this hinders accurate reflection of a patients TME and PD-1/PD-L1 profile when examining only one tumour biopsy at one point in time.

- There is variability in PD-L1$^+$cut-off values which range from 1 – 50% positive staining(94). The trend in clinical trials across various cancers has been to use either a 1% or 5% cut-value value to determine positive PD-L1 expression(49)(51)(52).

- The TPS measures tumour PD-L1 expression vs the CPS which measures both tumour and stromal PD-L1 expression. Different studies have found correlations with response to either tumour PD-L1 or combined PD-L1 expression(89). PD-L1 expression is assessed in gastroesophageal junction adenocarcinoma and advanced gastric cancer via the PD-L1 IHC 22C3 pharmDx assay using a CPS(95). Alternatively the TPS is used to assess PD-L1 expression in metastatic NSCLC patient samples(95).

- The type of assay used can impact on the level of PD-L1 expression recorded, as seen in a recent retrospective trail that analyzed 4868 FFPE NSCLC biopsy samples that had recorded >

50% PD-L1 expression(96). The study found no significant difference in measured PD-L1 expression between the 2C3 and 28-8 assays, however discordance was reported for the SP142 and LDTs assays(96). Suggesting the SP142 and LDTs assays could potentially underestimate high PD-L1 positivity(96). The Blueprint phase I feasibility study found that PD-L1 tumour cell expression was concordant for 22C3, 28-8 and SP263 assays, however the SP142 assay consistently stained fewer PD-L1 positive tumour cells(97).

PD-L1 IHC assays are the current benchmark for predicting response to anti PD-1/PD-L1 treatment, however clinical utility is questioned. In addition to assay discordance resulting in underestimation of high PD-L1 positivity, there is the potential for differences to occur between laboratories and pathologists manually scoring PD-L1. Discordant inter-pathologist scoring has been reported, particularly at lower PD-L1 cut-off points(98)(99). This highlights the need to standardize PD-L1 testing, particularly in the clinical setting were PD-L1 expression may be used to guide treatment options.

1.22 DIGITAL IMAGE ANALYSIS

1.22.1 Advantages of digital image analysis over manual image analysis

An advantage of digital image analysis over manual image analysis is that it can isolate, extract and quantify molecules in far greater detail than a visual estimation. Studies have shown improved performance of automated over manual image analysis(99)(100)(101)(102). Automated systems can detect very low abundance molecules from big data sets containing many layers and fields of view, quantifying cellular co-localization and relationships at a more nuanced level. The human eye has evolved poorly to discriminate staining intensity, if Inter-observer variability is removed, human error can be minimized, and the workflow standardized to increase analysis reproducibility.

1.22.2 Overview: Fluorescent microscopy

An LED light laser beam generated by the fluorescent microscope is focused into an excitation filter cube which separates the light beam into different wavelengths ranges(103). The wavelengths then exit through respective filters to flood the tissue sample, with wavelengths of differing ranges exciting

specific fluorophores bound to target antibody(103)(104). Fluorescent multiplexing relies on the basic principle of stokes' shift to measure emitted light of different spectral peaks against a dark background(105). The fluorophore, on returning to its lower energy ground state emits energy in the form of a photon producing a longer wavelength(105). The emitted longer wavelength is channelled into its respective emission filter, specific to its wavelength range(104). Emission and excitation filter cubes work as pairs rather than individual filters, to emit and then capture light/photons within a specific wavelength range corresponding the fluorophore(103)(104).

1.22.3 Translation of fluorescent light into pixels, the building block of digital images

Photons pass through the emission filter and are focused onto a detector referred to as a charge-coupled device(103). Photons striking the detector are recorded as hits and release an electrical charge that is quantified over a fixed time interval to determine a pixel value(103)(106). A pixel is a measurement of light and the smallest unit from which a digital image is composed(104). Pixels are boxes of equal size that form a two-dimensional matrix within the microscope's sensor (charge-coupled device) that detect hits from electrons(104). The digital image is produced from the optical image formed by the microscope, of the specimen using the two-dimensional matrix of pixels, with each pixel representing a specific area of the specimen(103). The photons/electrons in each pixel are then quantified by the sensor and converted into a digital value reflective of the signal intensity(104). The intensity of this value is proportional but not equal to the number of detected electrons/photons(103)(104). Therefore, the higher the intensity value of the pixel the greater the concentration of fluorophores within the corresponding area of specimen tissue. The shaded squares forming the visual image are not measurements but a fast, convenient impression of the image content. This concept is represented visually by Pateria *et al*. in figure 9, demonstrating a greyscale image composed from a matrix of pixel numbers(106).

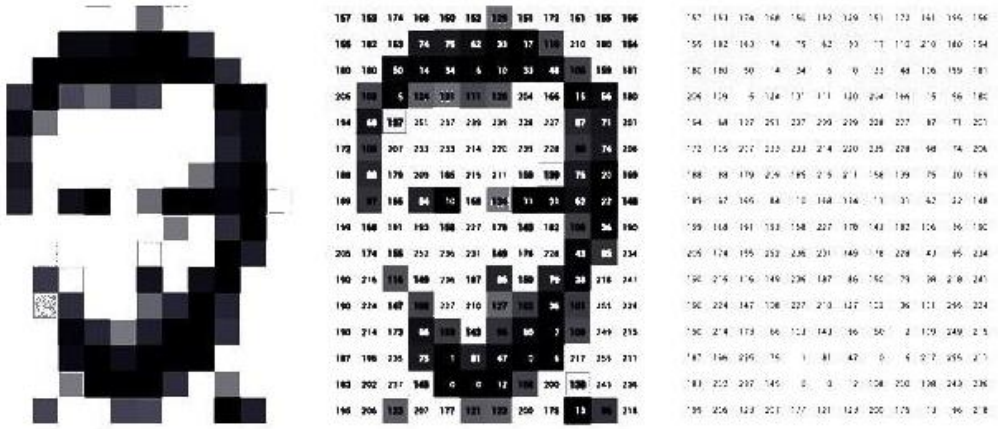

Figure 8. An imaging capturing system design by Pateria et al. to capture low light. A matrix of pixel numbers (far right), each represent a box varying in grey intensity (middle), the quantifiable pixel numbers digitally create a visual image(far left) for quick reference and ease of comprehension(106).

The image cannot be directly seen, instead object shape and size are determined indirectly by measuring the charge(103). A sensor within the fluorescent microscope scanner digitally assigns a pixel value to the quantity of photons or light, that has been captured by each filter cube allowing pixel values to be recorded for fluorophore channels(103)(104). If 16-bit image files are imported, the highest value a pixel will be is 65 535 (2^{16}) which produces a white image and the lowest pixel value of 0 produces a black image, all values in between are displayed as a gradient of grey. The numerical pixel value is the real data on which image analysis is based, not the display data of the grey square gradient. Visualising the data as shaded gradient boxes of differing shaded gradients on a computer screen allows identification and comparison of fluorophore expression within and between tissue samples.

1.23 NEXT GENERATION DIGITAL IMAGE ANALYSIS: MAPPING TME IMMUNE CONTEXTURE

Research in recent years has looked at the distribution of tumour infiltrating lymphocytes (TILs) in the TME and correlation of this distribution to known patient treatment outcomes. CD8 T cell density at the tumour invasive margin has been considered a good potential candidate for a predictive biomarker for anti-PD-1/PD-L1 treatment in a number of cancers(32)(107).

1.23.1 Immunoscore

The traditional cancer staging system has been one tool used to predict patients clinical outcomes, this approach focuses solely on tumour cells and assumes tumour progression is a largely cell autonomous process(108). Literatures supports the importance of the immune system on tumour growth and thus analysis of the immune contexture can be a tool to both predict prognosis and treatment response(109). The immunoscore was initially developed in 2006 by Galon *et al*. and numerates CD8 and CD45RO cell density both in the central tumour region and at the invasive margin(110). A score of 0 indicates low density of both cell types in both regions and a score of 4 indicates high cell densities in both regions(110). The immunoscore was applied to two large independent sample populations with colorectal cancer (n = 602) and it found 86.2% of patients with an immunoscore of 4 were alive after 5 years compared 27.5% of patients with an immunoscore of 1(110). The immunoscore has since been demonstrated in advanced melanoma, breast, lung, head and neck, kidney, colon, ovary and prostate and amongst various cancer cell types including, adenocarcinoma, squamous cell carcinoma, large cell carcinoma and melanoma (108).

1.23.2 Scoring tumour types

In 2012 Taube *et al*. classified patient sample FFPE melanocytic biopsies into 4 groups (PD-L1^{+}TIL^{+}, PD-L1^{+}TIL^{-}, PD-L1^{-}TIL^{+} and PD-L1^{-}TIL^{-}) and found high PD-L1^{+} expression was significantly associated with high TIL density while PD-L1^{-} tumours were significantly associated with low TIL density(111). Higher levels of INF-γ in PD-L1^{+} tumours was detected compared to PD-L1^{-} tumours, supporting the hypothesis of adaptive immune resistance(111). In 2015 Teng *et al*. developed this model further by assigning four distinct tumour types based on PD-L1 and TIL expression in the TME as seen in figure 8(92). Type I (PDL1^{+}TIL^{+}) indicates adaptive immune resistance, Type II (PD-L1^{-}TIL^{-}) indicates immune ignorance, Type III (PD-L1^{+}TIL^{-}) indicates intrinsic induction and Type IV (PD-L1^{-}TIL^{+}) indicates other suppressors are promoting immune tolerance(92).

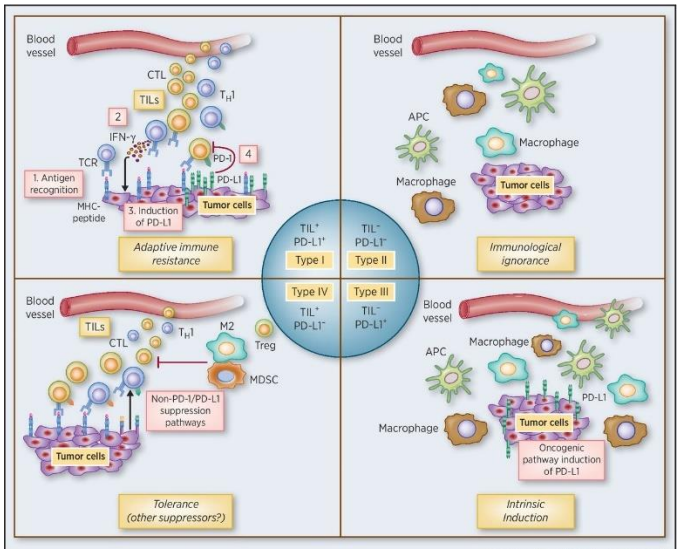

Figure 9. Tumour types defined by expression of PD-L1 and TIL expression proposed by Teng et. al.(92).

Several studies since have used the approach developed by Taube *et al*. and Teng *et al*. to stratify patients of various cancer types into groups based on $CD8^+$ T cell and PD-L1 expression(92)(112)(113)(114)(115)(116). These two variable parameters of the pre-treatment TME are combined to give a predictive tumour score that in contrast to PD-L1 expression alone can predict the probability of adaptive verses innate immune resistance. Patients with adaptive immune resistance already contain an active immune environment and may be closer to the tipping point for moving from the pre-transitioned phase into a new state phase. Numerous studies site that $PD\text{-}L1^+TIL^+$ tumours respond best to anti PD-1/PD-L1 therapy while $TIL^-PD\text{-}L1^+$ and $TIL^-PD\text{-}L1^-$ tumours show poor treatment response and $PD\text{-}L1^-TIL^+$ tumours may not be suitable for treatment(72)(92)(117)(100)(118)(119).

2 RESEARCH RATIONAL AND AIMS

2.1 RESEARCH RATIONAL

Preliminary data from the DREAM study has shown promising results, however there were still a proportion of participants that did not respond to chemoimmunotherapy. Given the risk of adverse events and the high financial cost of treatment there is a need to identify those participants most likely to respond to treatment. The first step to identify DREAM study participants most likely to respond to treatment is to associate the treatment ecosystem to treatment response. This association is demonstrated in model 1, a model that has been adapted from models previously described by Lesterhuis *et al.* and Dakos *et al*. In this model a participant in response to treatment will find themselves in 1 of 3 phases(70)(120). The non-responsive phase is associated with PD, the pre-treatment phase is associated with SD and the new state phase is associated with PR.

The rational for applying this 3-phase ecosystem model to treatment response is that within the pre-treatment phase there is a tipping point. The application of a strong enough force i.e. chemoimmunotherapy into the model may be sufficient to nudge those patients who are already close to the tipping point into a new state phase and achieve PR i.e. participant A. Alternatively for participant B who is further away from the tipping point the force may not be enough and they will remain in the pre-transitioned phase with SD. Quantification of patient's pre-treatment TME can be correlated to clinical outcomes (PD, SD and PR). Differences in immune contexture between the PD, SD and PR groups could be used to conduct hypothesis generating research, to explain why following chemoimmunotherapy, some participants achieve PR opposed to the SD. Is there evidence of a stronger immune reaction for the PR group, matched by a comparable but weaker immune reaction in the SD group? Quantifying immune markers for each treatment response group could identify potential biomarkers. Study design should consider variability in PD-L1 positive thresholds (1% vs 5%) and differing patterns of PD-L1 expression (tumour, stromal and combined tissue).

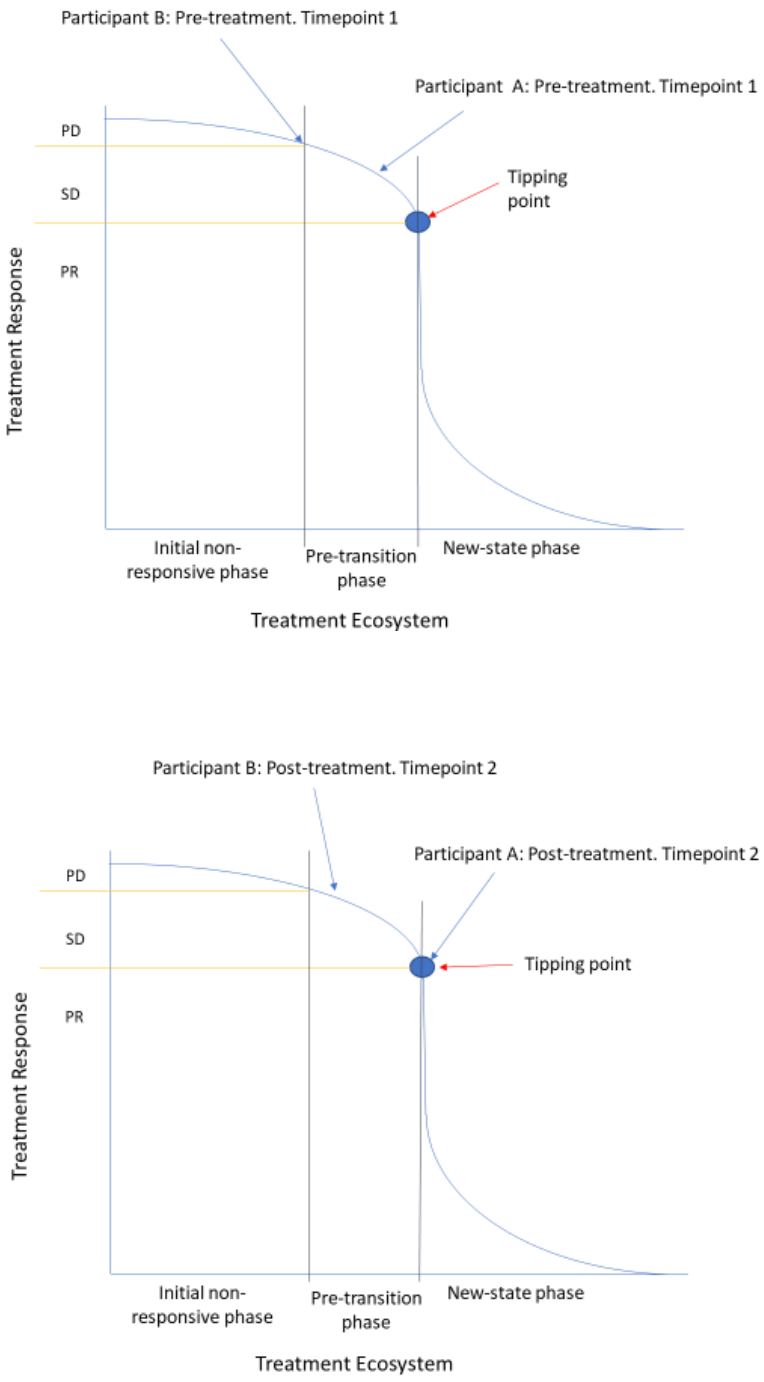

Model 1. Treatment ecosystem versus treatment response for chemoimmunotherapy in MPM. Prior to treatment is represented by timepoint 1 and post treatment is represented by timepoint 2. This model has been adapted from models previously described by Lesterhuis et al. and Darko et al(70,120).

2.2 HYPOTHESIS GENERATING RESEARCH AIMS

1. Compare the sensitivity of manual PD-L1 scoring against automated PD-L1 scoring.

2. Quantify PD-1, CD8 and PD-L1 cell populations in tumour cells, stromal cells and combined tissue and correlate to known patient outcomes including PD, SD and PR in response to chemoimmunotherapy in MPM.

3. Generate a hypothesis, from the quantification of pre-treatment immune contexture, to explain why a patient is tipped from the pre-transitioned state into a new state phase (responder) and identify predictive biomarkers.

3 METHODS

3.1 SAMPLE POPULATION (*N = 54*)

FFPE pre-treatment tumour biopsies were obtained from 54 confirmed cases of MPM from the DREAM open label, single arm, phase II clinical trial. The NHMRC Clinical trials centre (CTC; Protocol CTC 0142/AILTG 15/003)(ACTRN 12616001170415) recruited 54 participants from 10 Australia sites between December 2016 and October 2017(87). Median age was 68 and comprised 82% male participation, inclusion criteria for recruitment is described in table 4.

Table 4. Inclusion criteria and treatment regime for participants enrolled on the DREAM study.

Inclusion Criteria	Treatment Regime
• Ineligible for intent to cure surgery.	• Cisplatin (75 mg/m2) plus pemetrexed (500 mg/m2) and anti-PD-L1 durvalumab (1125 mg).
• Chemotherapy naïve.	
• Expected life expectancy > 24 weeks.	
• Minimum 5-years disease free from prior malignancies.	• Durvalumab administered during/following final chemotherapy stage.
• No previous MPM immunotherapy treatment.	
• PD-L1 expression not a requirement for recruitment.	• Drug combination repeated every 3 weeks for a maximum of 6 cycles or until disease progression.
Treatment immune related adverse events (any grade)	
• Hypothyroidism 9% (5)	• After 6 treatment cycles, participants with no disease progression received durvalumab (1125 mg) alone every 3 weeks for 12 cycles (18 cycles in total) or until disease progression.
• Increased lipase/amylase 4% (2)	
• Pneumonitis 4% (2)	
• Adrenal inadequacy 2% (1)	
• Hyperthyroidism 2% (1)	
• Renal impairment 20% (11)	
Clinical Assessment	
• CT scans were performed at baseline then weeks 6, 12, 18, 24, 30 and then every 9 weeks until disease progression.	

3.1.1 Ethics

The DREAM study was conducted according to NHMRC statement on ethical conduct in human research 2001, NHMRC Australian code for the responsible conduct of research 2007 and the principles of the world medical assembly in the declaration of Helsinki, 2008.

3.1.2 Variables measured

1. PR: requires tumour shrinkage exceeding 30% of tumour mass and have occurred twice at least 4 weeks apart from each other.
2. PD: requires an increase in tumour mass of 20%.
3. SD: participants that did not achieve PR or PD.

3.1.3 Statistical analysis of DREAM study participants

A safety run-in of 6 participants (3 + 3 design) was analysed using a simons 2 stage minimax design. Stage I contained 31 participants (including the 6 initial safety run patients) and stage II added another 23 recruits to the existing 31 participants (*n = 54*). A type 1 error rate of 5% gave > 90% statistical power. The studies primary endpoint was PFS rate of 45% at the end of stage II. The null hypothesis stated true PFS rate at 6 months is 45%, the expected rate of standard chemotherapy treatment. PFS was measured from the time of registration or until disease progression determined by a positive scan. Results displayed in figure 11 show most participants achieved a reduction in tumour size from the baseline. As reported at the IASLC mesothelioma meeting, July 2019, New York, the studies primary endpoint was met (using mRECIST). The null hypothesis was rejected as 57% (31) participants achieved median PFS at 6 months as shown in figure 10. Median survival was 18.4 months (95% CI 12.6 months – not reached), 12-month OS was 65% (95% CI 53-79%) and the 24-month OS estimate is 42% (95% CI 30-59%). Confirmed response using mRECIST identified 0 CR, 46% (25) PR, 39% (21) cases of SD and 15% (8) cases of PD.

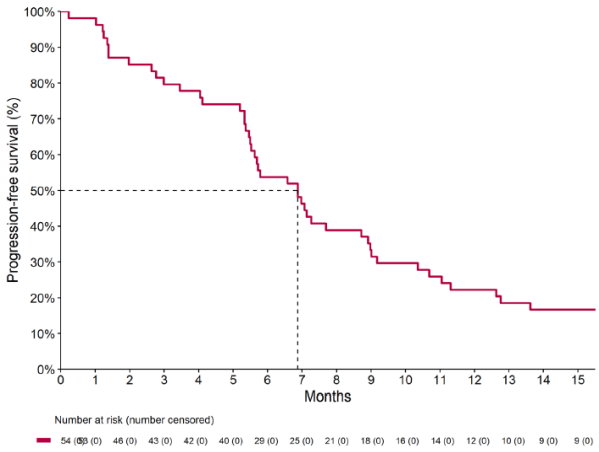

Figure 10. PFS at 6 months, according to mRECIST. Preliminary results from DREAM study presented at the IASLC mesothelioma meeting, July 2019, New York. PFS was > 6 months based on mRECIST criteria for 50% of study participants.

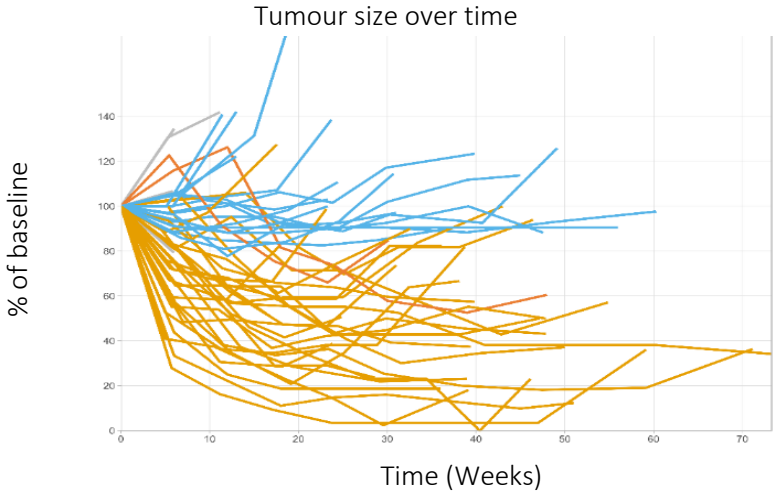

Figure 11. Spiderplot displaying changes to tumour size from the baseline over time. Blue lines indicate PD while orange lines indicate patients with SD or PR.

3.2 ASSOCIATING PRE-TREATMENT SAMPLES AND CLINICAL OUTCOMES TO IDENTIFY PREDICTIVE BIOMARKERS.

The scope of research reported within this thesis is limited to the correlation of digitally analysed pre-treatment histological samples to known treatment outcomes for participants of the DREAM study. De-identified FFPE tissue samples, were a mixture of excisional (5), core (14) and fragmented (29) biopsies and predominantly epithelioid (figure 12). A TSA based multiplex immunofluorescence assay

was used to identify potential predictive biomarkers PD-1, PD-L1 and CD8. Fluorescent images were analysed using bespoke semi-automated pathology digital image analysis software StrataQuest™. Clinical treatment outcomes correlated to patient outcomes including PD, SD and PR.

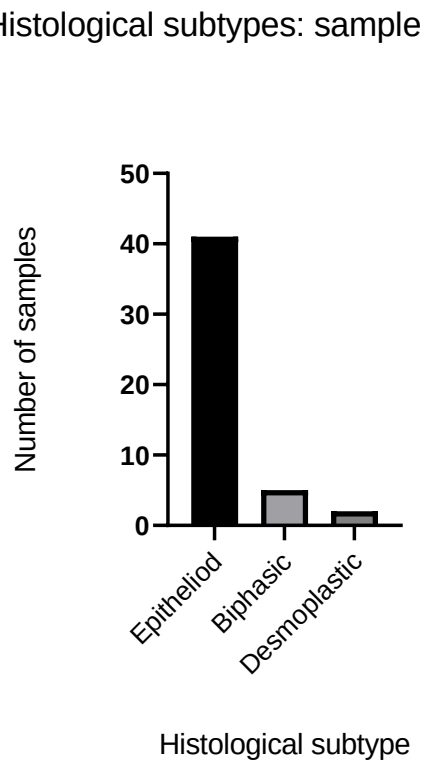

Figure 12. Percentages of histological subtypes in sample population. Epithelioid = 41, Biphasic = 5 and desmoplastic = 2.

3.3 METHOD OUTLINE

1. Slide Preparation

Figure 13. Preparing immunofluorescent slides.

2. Image Acquisition

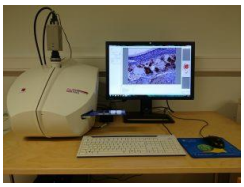

Figure 14. Pannoramic MIDI II Slide Scanner.

3. Image Analysis

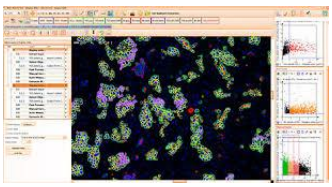

Figure 15. Strata Quest software screenshot.

3.4 SLIDE PREPARATION

3.4.1 Tissue samples available for multiplex immunofluorescent staining.

A total of 51 participant samples were available from the 54 participants recruited into the DREAM study for multiplex immunofluorescent staining. This is due to one participant withdrawing from the study itself, and insufficient material to prepare slides for another two participants. A further three participants were excluded at the digital image analysis stage. In one case this was owing to high levels of autofluorescence, while in another two cases there was insufficient material contained in the scanned images to analyse. In total 48 participants were included in the final statistical correlation and analysis. Each slide contained between 1 and 7 sections of tissue which all corresponded to the one participant. Multiplex immunofluorescent staining was carried out manually and spread over 4 batches to enable a manageable workflow. In batch one there were 14 slides, batch two had 14 slides (from which 1 slide was excluded), batch three had 18 slides (from which 2 slides were excluded) and batch four contained 5 slides.

3.4.2 TSA

TSA detects low-abundance molecules using amplified signalling, because this method requires lower amplification of secondary antibodies there is a reduction in background staining, giving a favourable signal to noise ratio(121). TSA covalently binds its target epitope in a highly specific manner, enzymatic HRP bound to the secondary antibody activates the inactive tyramide conjugated to its fluorophore as seen in figure 16(121). Activated tyramide can form covalent bonds with tyrosine sidechains at the antigen site, allowing for serial staining and stripping of primary/secondary antibody pairs while preserving fluorescence signal(121)(122). A key advantage the TSA technique is that multiple primary antibodies of the same species can be used in multiplexing without concern for cross talk, this simplifies panel design(122).

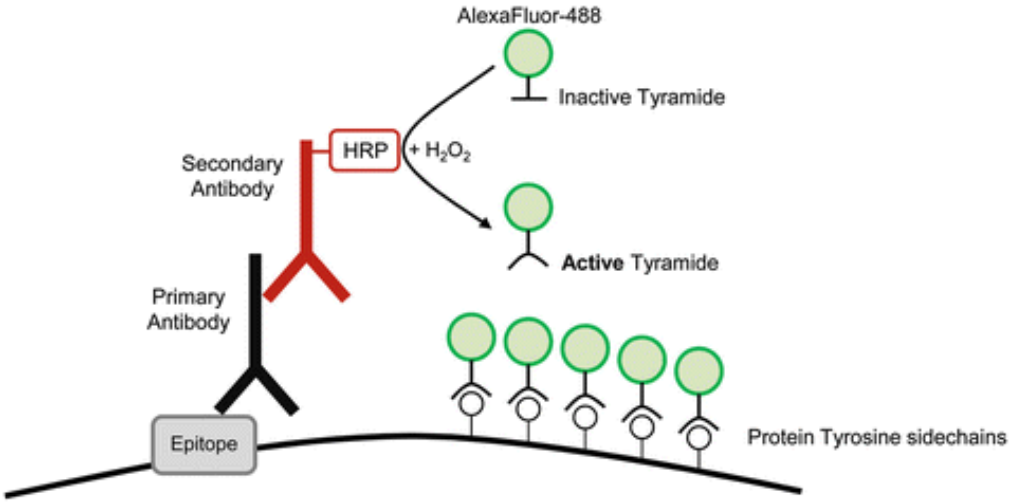

Figure 16. TSA tagged AlexaFlour-488 becomes activated by HRP and H_20_2 and is now capable of covalently binding tyrosine sidechains and emitting fluorescent signal. Signals stay covalently bound to tissue while primary/secondary antibody complexes are removed via antigen retrieval(121).

3.4.3 Panel summary

A 5-colour immunohistochemical-fluorescence panel (table 5) was designed and optimised by the St John of God, Cancer Research Group, Subiaco. Included in the panel are DAPI (nuclear counterstain), AF555 (detects cytokeratin/tumour epithelium), TSA-FITC (detects PD-1), TSA-Cy5 (detects PD-L1) and TSA-AF594 (detects CD8). The staining order reflects different fluorophore/antibody complexes ability to withstand multiple rounds of antigen retrieval. TSA-FITC, the most robust fluorophore can maintain signal strength after 3 rounds of antigen retrieval in contrast to the more sensitive TSA-Cy5 targeting PD-L1 which was placed 3rd in staining order to avoid diminished signal. Optimised working antibody concentrations and TSA fluorophore dilutions are described in table 6.

Table 5. 5-Panel of biomarkers used in multiplex immunofluorescence assay.

Target	Fluorophore	Staining order
PD-1	TSA – FITC	1st
CD8	TSA – AF594	2nd
PD-L1	TSA – Cy5	3rd
Cytokeratin	AF555	4th
Nuclei	DAPI	5th

Table 6. Slide Summary Template, optimised dilutions/working concentrations protocol.

Slide ID	1° Antibody (working concentration/dilution)	2° Reagent	TSA
Concentration Matched Isotype Control	Mouse IgGI (55.4 ng/mL; matches PD-1 concentration)	Mouse MACH-2	TSA FITC
	Mouse IgGI (1.57 µg/mL; matches CD8 concentration)	Mouse MACH-2	TSA AF594
	Rabbit IgG (1.7848 µg/mL; matches PD-L1 concentration)	Rabbit MACH-2	TSA Cy5
	Mouse IgGI (3.5 µg/mL; for cytokeratin)	Mouse AF555 (1:250)	_
Test Sample	PD-1 (55.4 ng/mL; 1:175)	Mouse MACH 2	TSA FITC
	CD8 (1.57 µg/mL; 1:100)	Mouse MACH 2	TSA AF594
	PD-L1 (1.748 µg/mL; 1:500)	Rabbit MACH 2	TSA Cy5
	Cytokeratin (3.5 µg/mL; 1:50)	Mouse AF555 (1:250)	_

A detailed explanation of manufacturer equipment and materials used and panel optimisation has been previously described by Anyaegbu et al. (123).

3.4.4 Workflow: Slide Preparation.

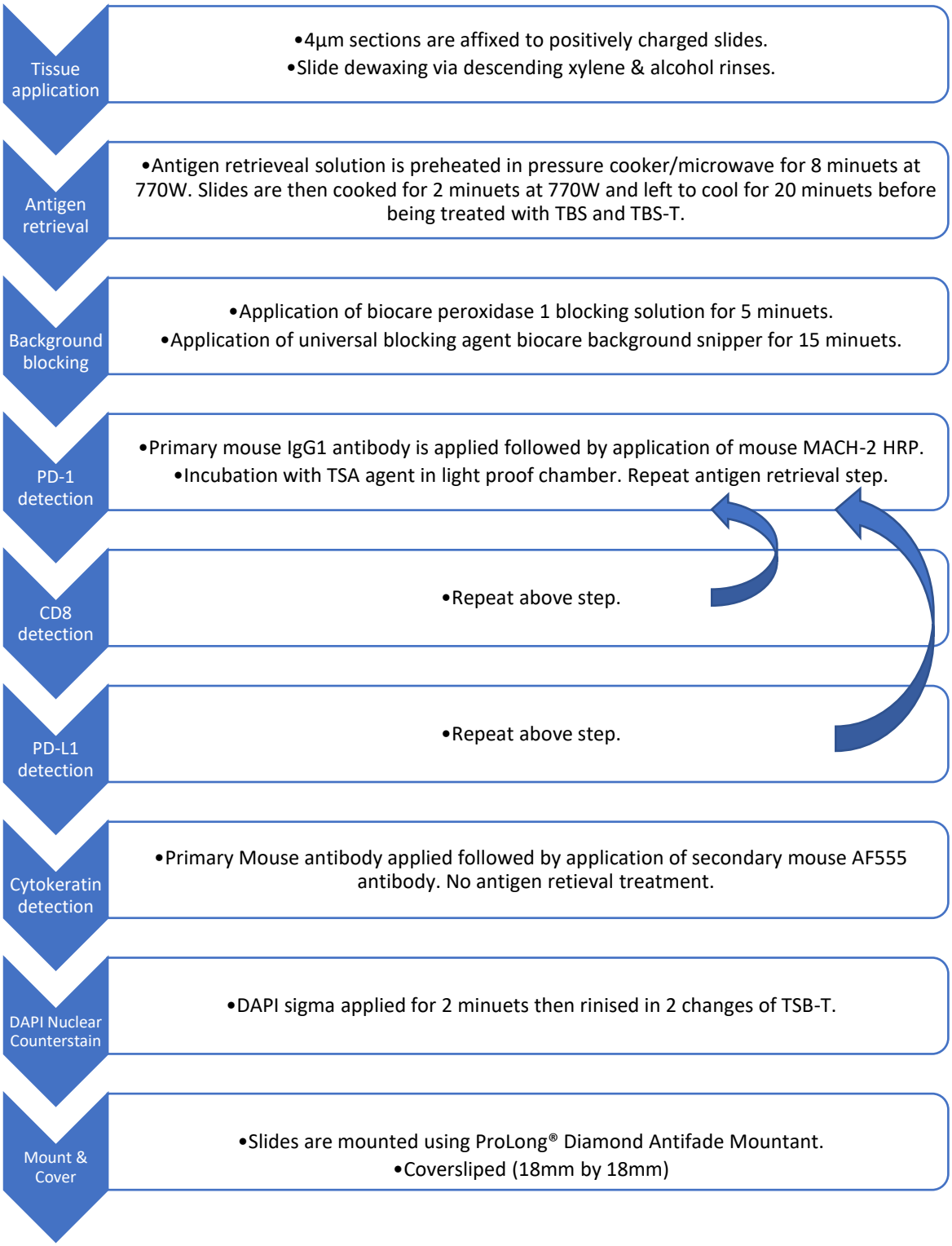

3.5 IMAGE ACQUISITION

Fully automated multispectral image analysis software can separate spectral overlap from multiple markers simultaneously by application of linear unmixing algorithms. This was demonstrated by Valm *et al*. through the spectral unmixing of 16 commercially available fluorophores(124). A fully automated model uses software to build a library of individual marker excitation and emission spectra that it then uses to separate out multiple markers with overlapping emission and excitation spectra. In non-fully automated fluorescent multiplexing system, unmixing algorithms are not used, instead bandpass filters are used to separate emission and excitation spectra when acquiring the image. This traditional method is limited by the number of filters that a scanning system can hold, typically to the simultaneous detection of 4 to 5 markers (125). The majority of TSA-based multiplex staining kits, are recommended for use with multispectral image analysis software that uses spectral unmixing algorithms(126).

3.5.1 Optimisation of TSA-multiplex immunofluorescent assay to be used in conjunction with traditional non-fully automated scanning systems.

The partially automated pathology image analysis software, StrataQuest ™ version 6 (TissueGnostics, Vienna, Austria) that is used for image analysis does not use spectra unmixing algorithms. TSA multiplex immunofluorescent images were acquired for this study using a traditional scanning system bandpass filters following an optimised protocol as previously described by *Anyaegbu et al.*(123). Narrow band-width filters of specific ranges detailed in table 7, ensured only maximum excitation and emission wavelengths passed through filters, reducing the need for spectral compensation or to "unmix" different wavelengths. This method also excludes dim fluorophores, giving a higher resolution image. Importantly this allows the researcher to bypass the more expensive machine learning software and use the more widely available traditional scanners to scan slides prepared with a TSA tagged assay.

3.5.2 Image Acquisition Parameters

Images were acquired using a plan-apochromat objective of 0.8 at 20x magnification (Carl Zeiss, Oberkochen, Germany) on a fluorescent Pannoramic MIDI II scanner (version 1.18.2.51404, 3D Histech, Budapest, Hungary). The scanner was equipped with a pco.edge sCMOS camera (PCO,

Germany) and LED Spectra 6 light engine (Lumencor, Beaverton, OR, USA). A total of 5 Semrock epifluorescence filter cubes were fitted with paired excitation/emission filter sets (table 7).

Table 7. 5-Colour Panel of markers and associated epifluorescent excitation/ emission optics. Designed and optimised by St John of God, Cancer Research Group, Subiaco.

Semrock Cube Filter Set	Fluorophore	Target	Excitation Filter Transmission Range (nm)	Emission Filter Transmission Range (nm)
LED-DA/FI/TR/Cy5-A-000	DAPI	Nuclei	378.3 – 406.8	412.2 – 451.0
LED-DA/FI/TR/Cy5-A-000	FITC	PD-1	459.0 – 489.7	497.1 – 532.9
SpGold-B-000	AF555	Cytokeratin	521.2 – 546,8	555.0 – 589.1
LED-DA/FI/TR/Cy5-A-000	Cy5	PD-L1	623.1 – 646.9	656.9 – 804.1
SpRed	AF594	CD8	573.1 – 599.0	608.9 – 647.1

Exposure times for each of 16-bit depth channel to LED light is described in table 8.

Table 8. Exposure time (s) per filter cube per batch of immunofluorescent scanned samples.

	Filter 1		Filter 2		Filter 3		Filter 4		Filter 5	
	Marker	Exposure Time (s)	Marker	Exposure Time (s)	Marker	Exposure Time (s)	Marker	Exposure Time (s)	Marker	Exposure Time (s)
Batch 1	FITC	10	DAPI	14	Cy5	22	SpGold	10	SpRed	10
Batch 2	DAPI	15	FITC	7	Cy5	7	SpGold	15	SpRed	15
Batch 3	DAPI	12	FITC	10	Cy5	7	SpGold	15	SpRed	10
Batch 4	DAPI	12	FITC	10	Cy5	7	SpGold	15	SpRed	6

3.6 IMAGE ANALYSIS: THE CONCEPT

- Define region of interest.
- Count all cells.
- Evaluate each individual marker for all detected cells.
- Generate scattergrams to quantify and compare positive and negative cells.

3.6.1 StrataQuest™: pixel quantification & visualisation

The real image data, in the form of a pixel value assigned number, is imported into StrataQuest™. Measuring pixel size and counting pixels identifies the objects size and position within the tissue sample, as a pixel is a proportion of the total field of view contained within the image. If the width of an image area is 400 µm, and contains 200 pixels in a horizontal direction, then the width of the pixel is 0.5 µm (200 pixels / 400 µm). Once a pixel size is known, size measurements can be calibrated. If a structure within an image is measured horizontally to be 20 pixels in length, with a pixel size of 0.5 µm then the actual length of that structure is 10 µm, as is seen by the cell diameter indicated in the bottom right of figure 17.

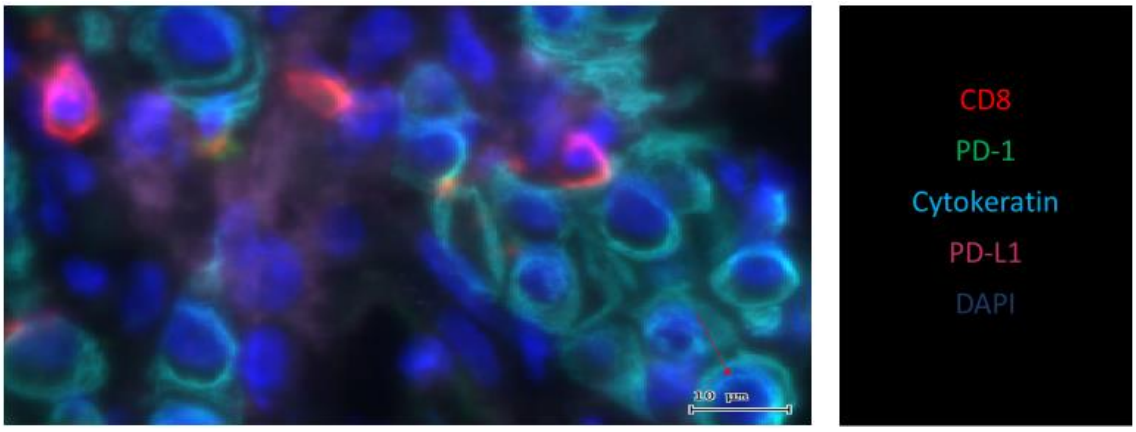

Figure 17. 20x Magnification. Lung tissue sample from a DREAM study participant. Average cell diameter as indicated by the red arrow is 10 µm.

Display values: configuring image brightness in StrataQuest™

In StrataQuest™ a display value is manually set for each fluorophore channel and this value dictates the level of brightness that the image is displayed on the screen. Display values range from 0 to 65 535 in order to correspond with pixel values, however display values, unlike pixels, are not a unit of measurement. Increasing a display value will make an image dimmer while decreasing the display value will make the image brighter. Adjusting the display value does not change the image data of the numerical pixel, it only changes how the data is viewed. The same image is displayed in figures 18, 19 and 20 of placenta tissue on the cytokeratin (SpGold) antibody isotype control slide, the image in each figure contains the same number of pixels. The variable in these images is the display value that has been assigned to display the cytokeratin fluorophore signal in each image. In figure 18 the display value is 600, in figure 19 it is 42,000 and in figure 20 it is 22,000. The value in figure 18 is to low, the image appears blurred, alternatively in figure 19 the value is too high, and the image appears dim. The optimal cytokeratin display value to distinguish tissue morphology and intensity of fluorophore signal is 22,000, as seen in figure 20.

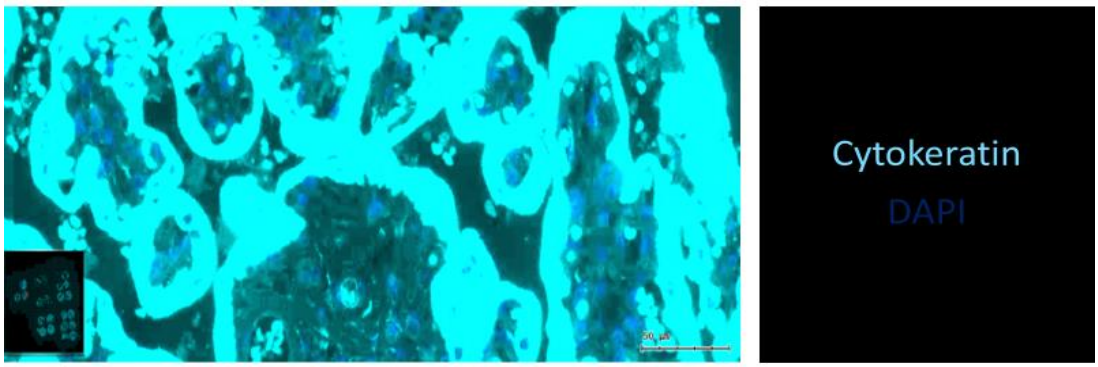

Figure 18. 20 x Magnification. Cytokeratin isotype control, placenta tissue TMA. Display levels set at 600 for cytokeratin (SpGold) channel in StrataQuest™.

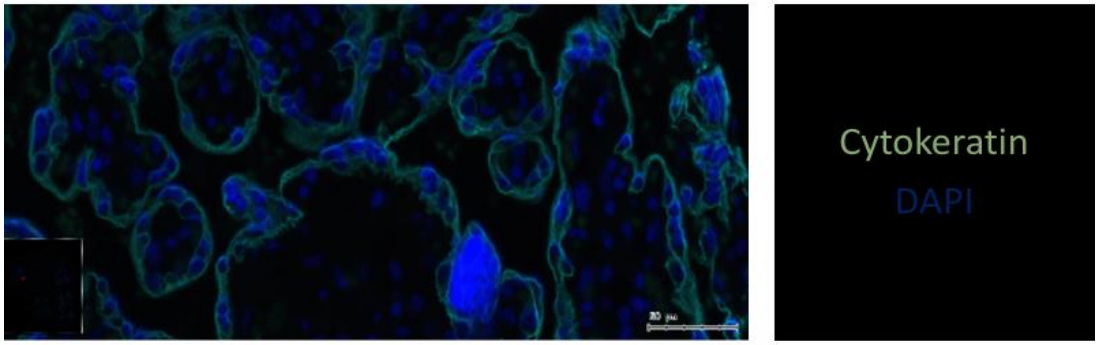

Figure 19. 20x Magnification. Cytokeratin isotype control, placenta tissue TMA. Display levels set at 42,000 for cytokeratin (SpGold) channel in StrataQuest™.

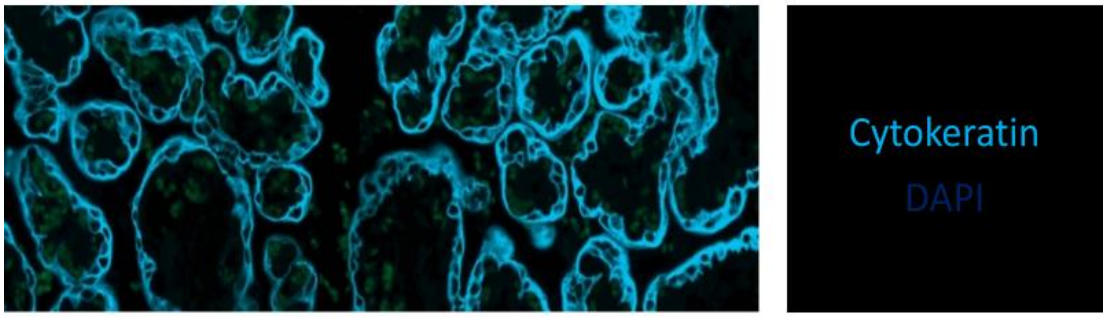

Figure 20. 20x Magnification. Cytokeratin isotype control, placenta tissue TMA. Display levels set at 22,000 for cytokeratin (SpGold) channel in StrataQuest™.

3.7 WORKFLOW: IMAGE ANALYSIS.

1. Create a project and build a cache in StrataQuest™ to separately analyse each batch.

2. Set display levels using biological controls.

3. Define ROIs corresponding to paired pathologist annotated H&E slides.

4. Remove staining artefacts i.e. tissue folds, or biological matter i.e. blood vessels.

5. Check thresholds for tissue, epithelium and PD-L1 masks and nuclear segmentation layer.

6. Analyse & update image data for ROIs.

7. Check adjustments made in steps 4 & 5 have been made to the appropriate mask by checking appropriate mask and the manual corrections mask.

8. Check nuclear segmentation layer and adjust nuclear size cut-off to correct for over segmentation and remove nuclear fragments.

9. Optimise cut-off values for PD-1(FITC), PD-L1 (Cy5), CD8 (SpRed) and Cytokeratin (SpGold) to reduced background staining and limit the number of false positive/false negative events.

10. Export Statistics (raw data) to excel.

3.7.1 Create project in StrataQuest™ and build cache

There are 4 projects created to analyse 48 slides in total, with each batch having been exposed to constant biological and technical controls.

Imported image files are saved in jpeg. format preserving both:

a) Image data i.e. pixel numbers and

b) Metadata i.e. image type (.jpeg), bit-depth (16-bit) and microscope settings (table 6).

3.7.2 Set display levels based on isotype controls.

Display levels are manually set for PD-1 (FITC), PD-L1 (Cy5), CD8 (SpRed), Cytokeratin (SpGold) fluorophore and DAPI channels when opening the project for the first time and remain the same for every sample in the batch to act as a technical control. Display levels are set by ensuring fluorophore signal from respective isotype controls can be clearly visualised in the digital image and the values set for each batch are listed in table 9.

Table 9. Fluorophore/DAPI display values set in StrataQuest™.

	DAPI	Cytokeratin (SpGold)	CD8 (SpRed)	PD-L1 (Cy5)	PD-1 (FITC)
Batch 1	23, 000	22, 000	30, 000	21, 000	13, 500
Batch 2	31, 264	9, 620	18, 939	22, 847	13, 000
Batch 3	45, 394	18, 939	20, 141	22, 870	13, 500
Batch 4	27, 356	18, 338	18, 037	18, 638	15, 322

3.7.3 Assign pseudo colours for overlay channel and check display levels accurately display gradient of fluorophore signal across samples

Monochromatic fluorophore channel signals are combined in an overlay channel as seen in figure 21. To differentiate between cell sub-populations and cellular co-localisation, appropriate pseudo colours are assigned to each fluorophore in the overlay channel. Bright red indicates low abundance CD8 (SpRed), green highlights PD-1 (FITC) and on colocalization a $CD8^{+}PD\text{-}1^{+}$ cell appears yellow. Magenta represents PD-L1 (Cy5), and aqua blue marks cytokeratin (SpGold) highlighting tumour epithelium and dim navy blue represents high abundance DAPI (nuclei) staining.

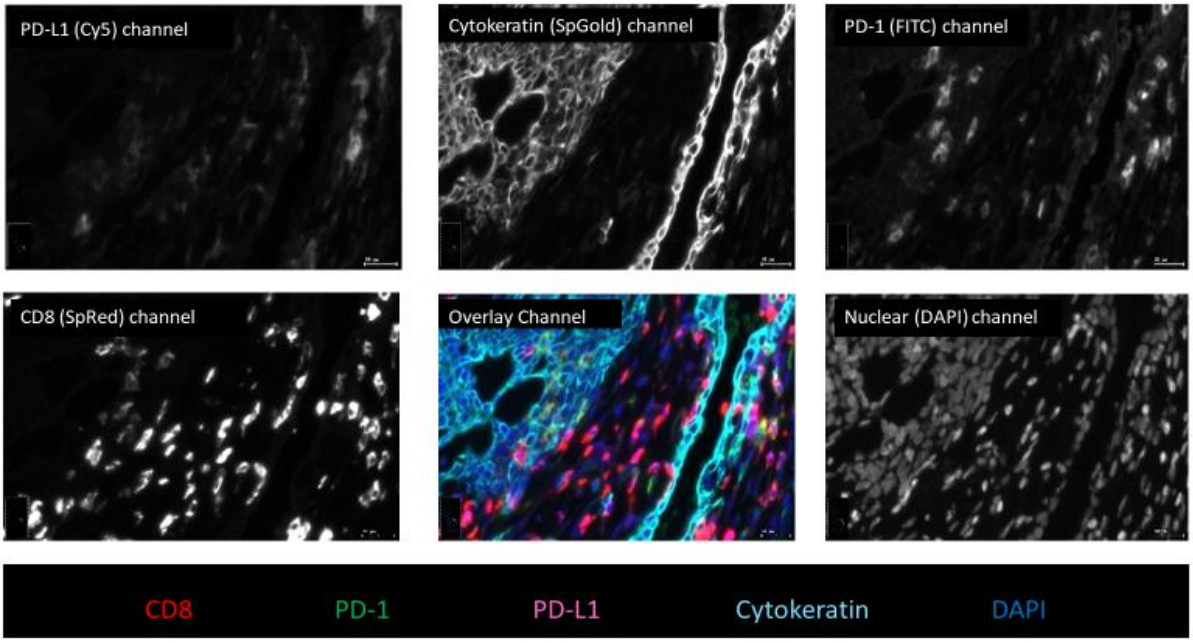

Figure 21. 20x magnification. Lung Tissue Sample, DREAM participant. Panel of DAPI/fluorophore markers and channel overlay.

Marker concentration is heterogeneously expressed amongst and within participant samples. This is evident when comparing the variation of Cy5 (PD-L1) expression between two different regions of interest originating from the same sample in figure 22. An optimal “fit” needs to be found and applied to all samples to minimising both extreme bright and dim signal. Fluorophore display levels of all samples are checked by viewing the fluorophore channels and adjusting accordingly while ensuring fluorophore signal for isotype controls remain clearly displayed.

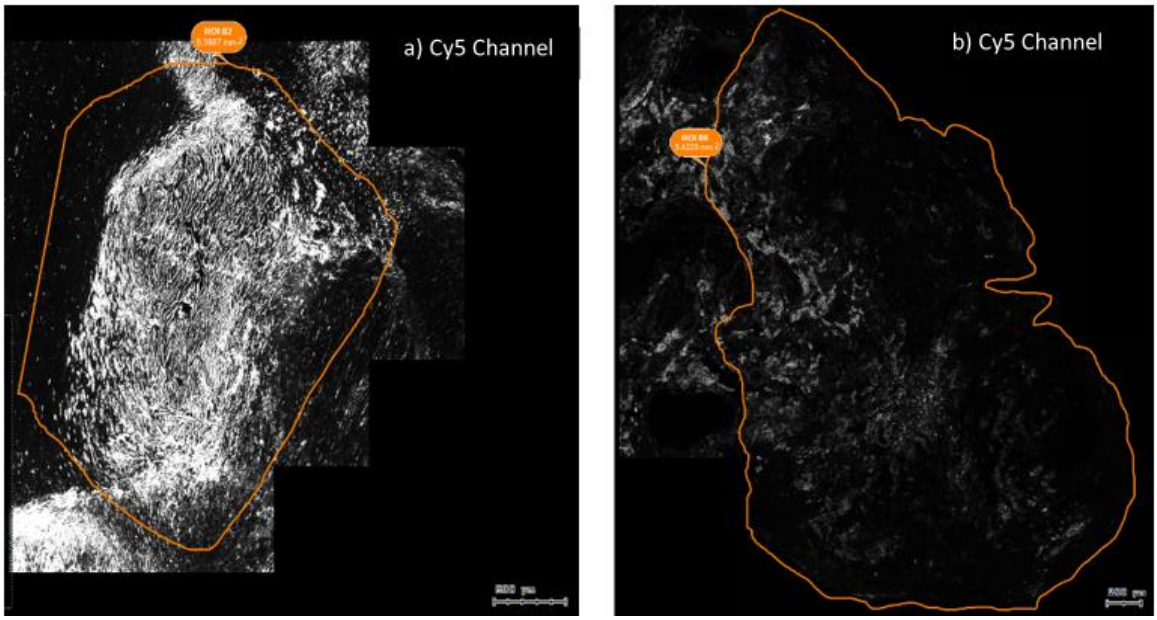

Figure 22. 20x Magnification. Lung tissue sample, DREAM study participant. Comparison of Cy5 expression between regions of interest within the same sample. a) Marked PD-L1 expression b) Modest PD-L1 expression.

3.7.4 Defining ROIs

Immunofluorescent staining does not present tissue architecture as clearly as H&E staining(127). H&E slides were produced from sections taken from the same FFPE tissue block used to produce immunofluorescent slides. H&E slides were scanned at 20x magnification, numerical aperture 0.75 (Olympus UPlanSAPO) using brightfield scanning system Aperio ScanScopeXT (Aperio; Leica Microsystems, Germany). Images viewed using Aperio ImageScope software (version 12.4, Leica BioSystems, U.S.A). Images viewed in TIFF (SVS) file format were annotated by a pathologist, marking viable tumour regions and excluding areas of necrosis and non-tumour tissue. The pathologist marked H&E annotations were manually copied (figure 23), using a mouse, onto the corresponding immunofluorescent image in StataQuest™ to create a ROI. Image analysis only calculates pixels within the defined area of each ROI. It is necessary to confine analysis to the area of interest due to the length of time taken to analyse tissue.

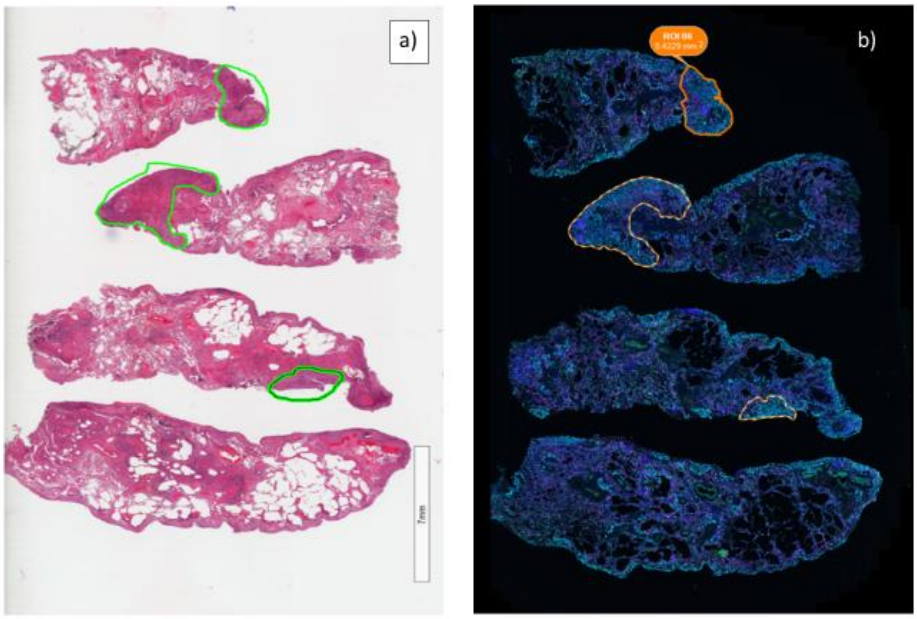

Figure 23. 20x magnification. Representative sections taken from same patient lung sample, DREAM study participant. FFPE tissue block. a) H&E stained section annotated by pathologist with areas of tumour marked in green b) Annotations copied onto immunofluorescent Image in StrataQuest™, creating ROIs.

3.7.5 Remove staining artefacts and blood vessels

Tissue folds are caused by a section of tissue folding over its self twice or more when placed onto a slide, forming a ridge that traps antibody causing inaccurate staining as seen in figure 24 a). Multifocal blotchy staining distorts nuclear staining as seen in the DAPI channel in figure 24 b). Histological artefacts are deleted from the software.

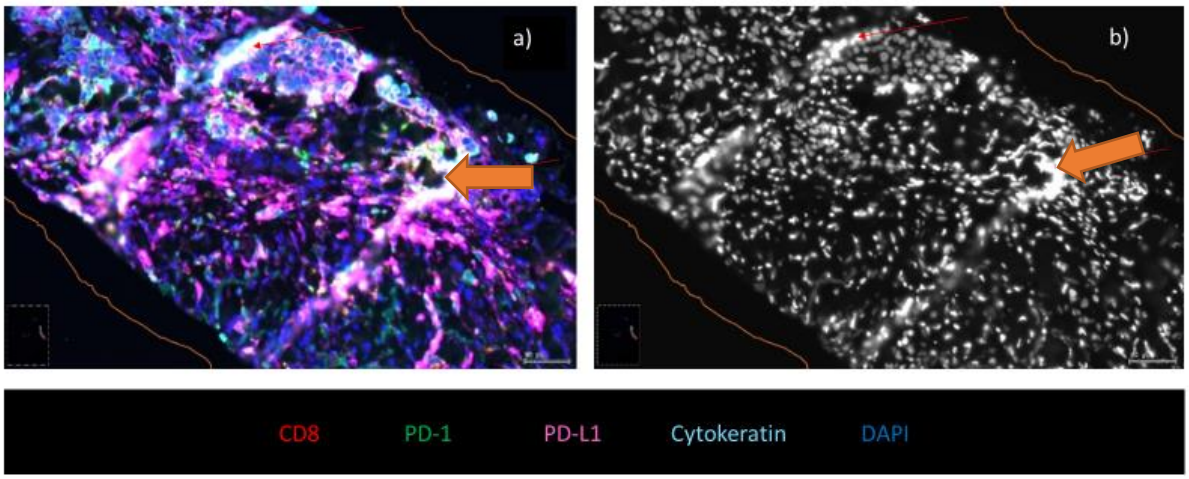

Figure 24. 20x Magnification. Core lung biopsy from participant of DREAM study. a) Overlay channel: diagonal strips of blotchy staining caused by tissue folds indicated by the orange arrow. b) DAPI Channel: algorithms are unable to accurately segment nuclei in areas were folds occur, as indicated by the orange arrow.

Red blood cells produce high levels of autofluorescence that are visible in the FITC channel as indicated by the red arrows in figure 25. b). To reduce the number of false positive PD-1 cells, blood vessels such as the one indicated in figure 25. a) are deleted from the tissue mask.

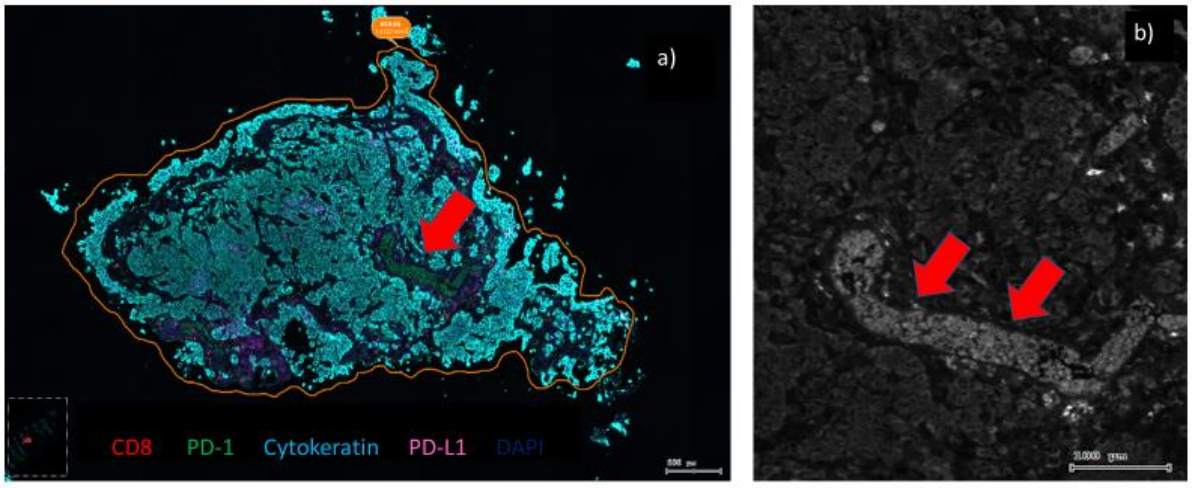

Figure 25. 20x magnification. Lung tissue sample, participant of DREAM study. a) Overlay channel: Red arrow indicating blood vessel. b) FITC channel: Red arrows pointing to autofluorescence red blood cells in a blood vessel.

3.7.6 Optimally adjust tissue, epithelium and PD-L1 masks and nuclear segmentation layers

Image analysis occurs through sequential layers or masks that segment tissue depending on distinct cell populations. A part of image processing is to detect objects via image segmentation, by creating a binary image a pixel can only have only 1 of 2 values, it is either on the mask or it is not. The binary image is created using thresholding to identify pixels above or below a certain value, the threshold is set in the software's layer editor profile. Creating a binary image is necessary to identify and measure cells on a mask. The advanced mode of the software app contains optimised thresholds previously determined by the St John of God, Cancer Research Group, Subiaco. These threshold values are described in table 10 and were applied to all 4 projects in analysing all 48 participant samples.

Table 10. Threshold levels for Tissue Mask, Epithelium Mask, PD-L1 Mask and Nuclear Segmentation.

Nuclear segmentation threshold	Tissue mask threshold	Epithelium mask threshold	PD-L1 mask threshold
2000 - 8000	4000	3000	5000

The Tissue Mask

A tissue mask is the first layer to be created it comprises signals of all 5 fluorophore channels, it acts as a boundary for cellular analysis as only cells contained within the tissue mask will be analysed. It is the parental mask layer from which all other layers of analysis are derived, any modifications made to this layer will be carried through to all subsequent layers of analysis. The tissue mask as seen in figures 26. a) and 26. b) shows the tissue mask in purple and tissue off the tissue mask is shown in red. The small red fragments are below the set tissue mask threshold of 4000 and are therefore excluded from analysis. Variation in the degree of tissue fragmentation within batches is evident when comparing figure 26. a) and 26. b).

Serial sections were cut from the same tissue block to produce diagnostic H&E slides, chromogenic IHC slides and multiplex immunofluorescent slides. Sections used for multiplex immunofluorescent

slides were the last to be cut from the tissue block, in some instance tissue quantity was scant and more prone to fragmentation. If the temperature of the flotation bath used for tissue sections, is higher than the melting point of wax by 4-5°C a section may overexpand and crack. Tissue separation can also occur if sections are left in the floatation bath for a period longer than 15 seconds. Additionally, poorly processed tissue can lead to excessive cracking of tissue.

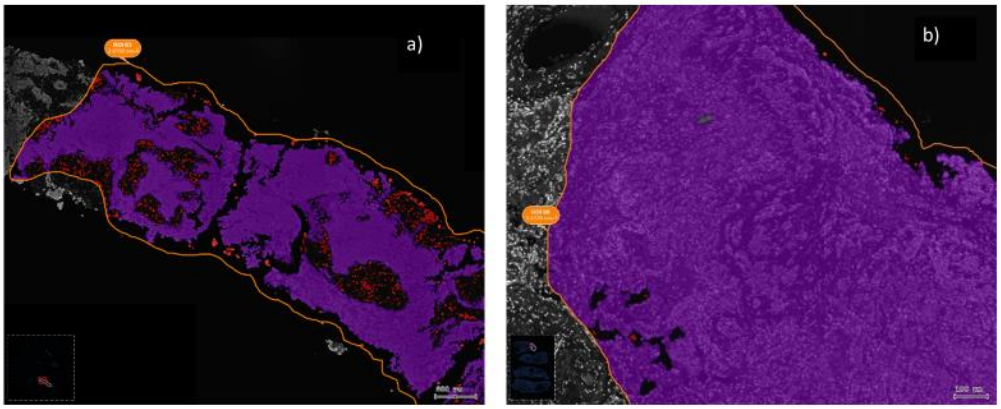

Figure 26. Tissue Masks from different DREAM participant samples within the same project, a) patches of tissue fragmentation seen by excluded tissue in red. b) Patient sample containing almost no excluded fragments.

The PD-L1 Mask

The PD-L1 mask denoted by purple in figure 27. b) detects PD-L1 expression on the tissue mask based on a threshold intensity value of 5000. This threshold is based on an algorithm that detects positive signal in in the PD-L1 (Cy5) channel as seen in figure 27. a).

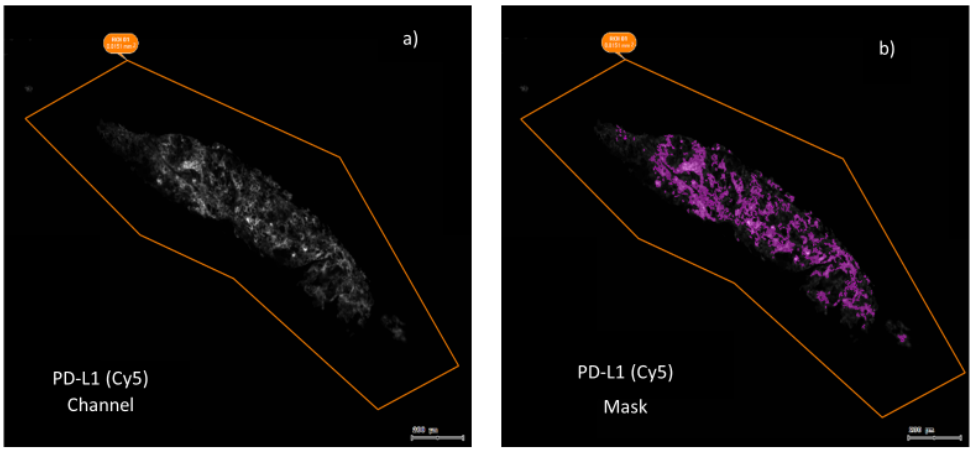

Figure 27. a) PD-L1 (Cy5) Fluorophore channel displaying signal for PD-L1 expression b) PD-L1 mask detecting cells expressing PD-L1 (Cy5) signal.

The Epithelium Mask

The epithelium mask denoted by aqua blue in figure 28. b) detects tumour epithelial tissue on the tissue mask based on a threshold of 3000. This threshold is based on an algorithm detecting positive staining in the cytokeratin (SpGold) channel seen in figure 28. a). Increasing the threshold will reduce the area of the epithelium mask and decreasing the threshold will increase the area of epithelium mask.

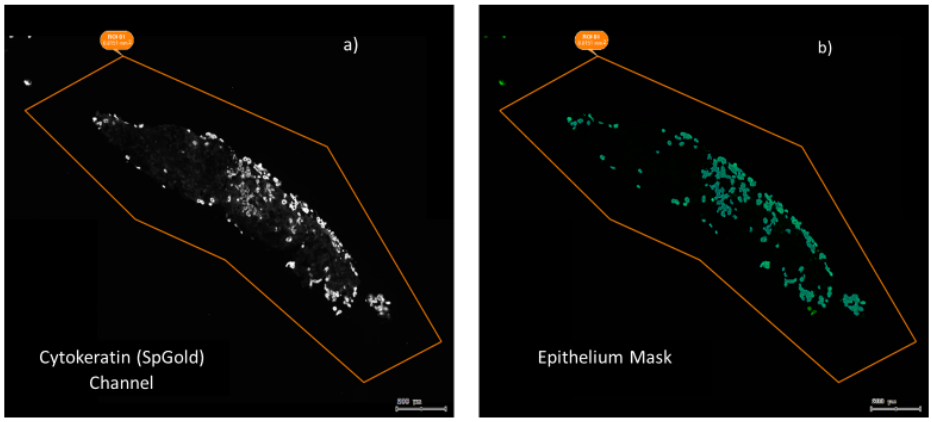

Figure 28. Lung sample, participant of DREAM study a) Cytokeratin (SpGold fluorophore channel, b) Epithelium mask detecting cells expressing SpGold signal, an indication of cytokeratin and tumour epithelium.

The Stromal Mask

The stromal mask denoted by green in figure 29. a) detects stromal tissue by subtracting the epithelial mask from the tissue mask. Adjustments made to the epithelium mask, which is displayed alongside the stromal mask in figure 29. b) will alter the stromal mask.

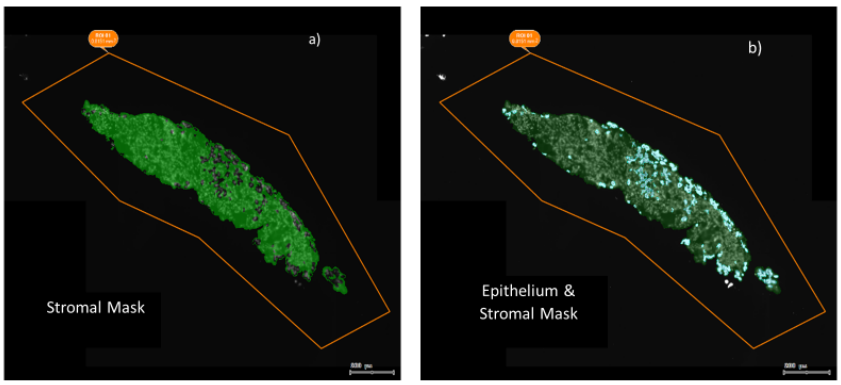

Figure 29. Lung Sample, Participant DREAM study. a) Stromal Mask, indicating all non-epithelial cells in green, b) Epithelial Mask (Aqua Blue) and Stromal Mask (Green).

The Nuclear Segmentation Layer

The software draws a green ring around the nuclei boarder based on the detection of the nuclear counter stain DAPI as seen in figure 30. b). The nuclear segmentation lower threshold is 2000 and the upper threshold is 8000. At this level all nuclei expressing a mean average DAPI staining between 2000 – 8000 pixels will be segmented and counted as a positive cell nucleus. The nuclear segmentation layer is also overlaid with masks i.e. tissue, epithelium, stromal or PD-L1 to determine the number of cells on that mask.

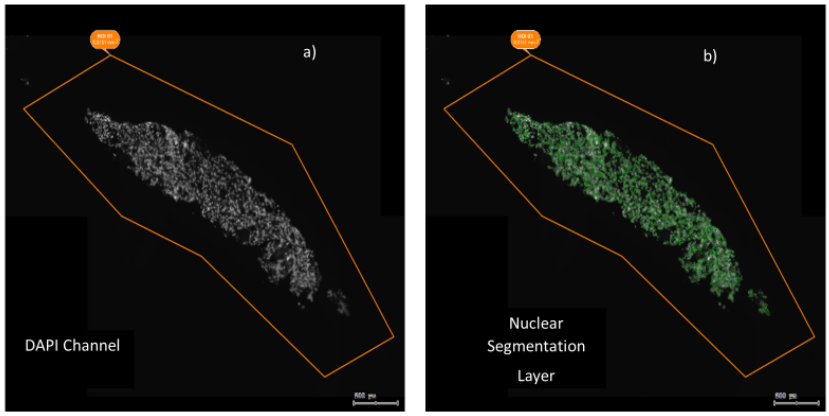

Figure 30. Patient Lung Sample. a) DAPI (nuclei) marker channel. b) Nuclear segmentation layer: green lines drawn around DAPI staining show segmented cell nuclei.

The Epithelium on PD-L1 Mask

This layer is produced by overlaying the PD-L1 mask, shown in figure 31. b), onto the Epithelium mask which in figure 31. a) is shown in aqua blue. The area where the two masks overlay is denoted in yellow as seen in figure 31. c). Cells on this mask are considered tumour epithelium expressing PD-L1^{+} cells (median 96.5% mask area cytokeratin^{+}PD-L1^{+} cell area). To be certain that PD-L1 is being expressed by epithelium at the epithelium/stromal border and not a stromal cell, a separate layer of analysis occurs. The epithelium mask is contracted inwards slightly as seen in figure 31. d). and the contracted area is marked by a yellow line as seen in figures 31. c) and 31. d).

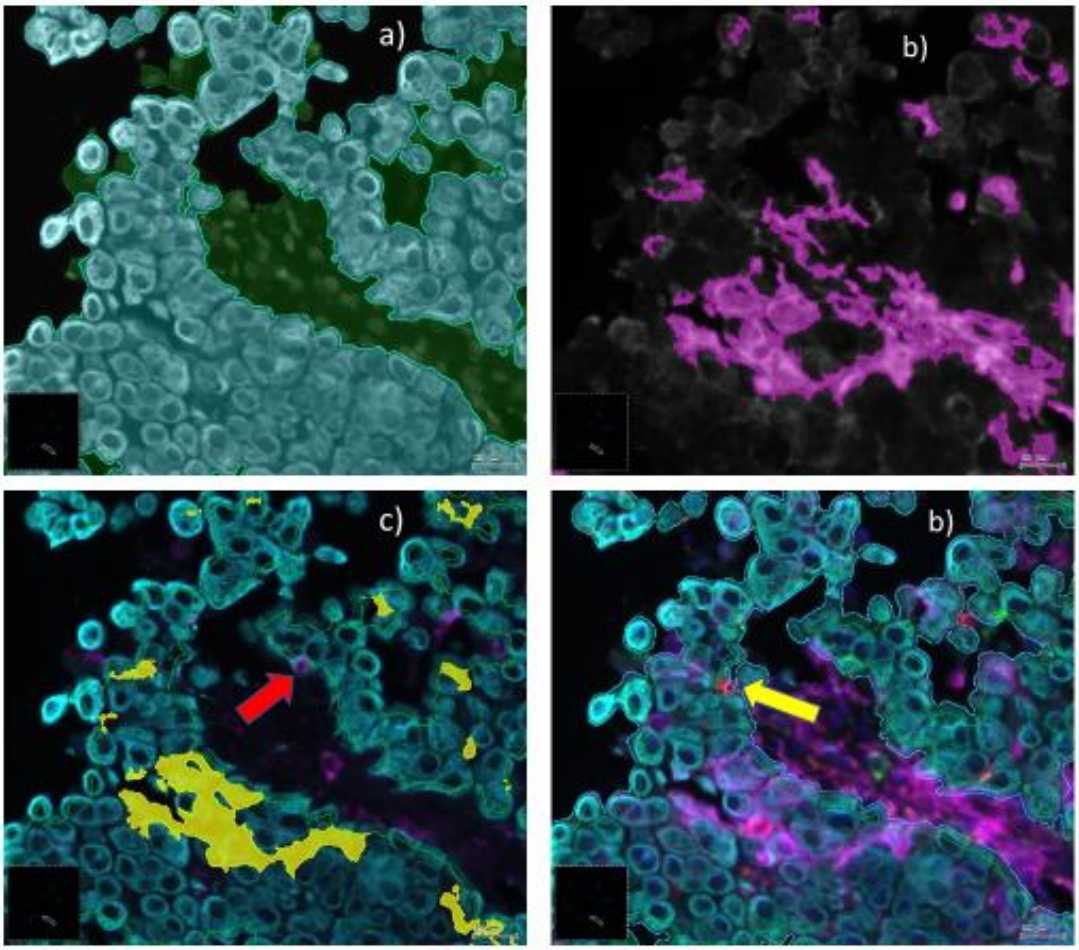

Figure 31. Lung sample, participant of DREAM study a). Epithelium (aqua blue) & stroma (green) mask, b) PD-L1 Mask (purple), c) Epithelium on PD-L1 Mask overlay (yellow), a red arrow indicates the exclusion of a PD-L1⁺ cell from the epithelium mask. d) Contracted epithelium mask, indicated by yellow line, with yellow arrow showing the exclusion of a CD8⁺ cell from the epithelium mask.

3.7.7 Analyse and update data in StrataQuest™.

Time taken to analyse individual ROIs is proportional to the fields of view in each ROI and analysis time per ROI ranged from 1.3 minutes to 19.6 hours.

Check adjustments made in steps 4 & 5 in image analysis workflow

On completion of analysis, amendments are checked in the layer editor menu to ensure results have been updated in appropriate masks/layers. The tissue mask layer is checked to ensure deleted sections have been removed. As seen in figure 32. c) the blood vessel removed in step 4 has been permanently deleted from the purple tissue mask. It has also been deleted from the nuclear

segmentation layer seen in figure 32 a) red blood cells can distort nuclear segmentation. Adjustments can be viewed in the manual correction layer seen in figure 32 b), deleted tissue is shown in yellow.

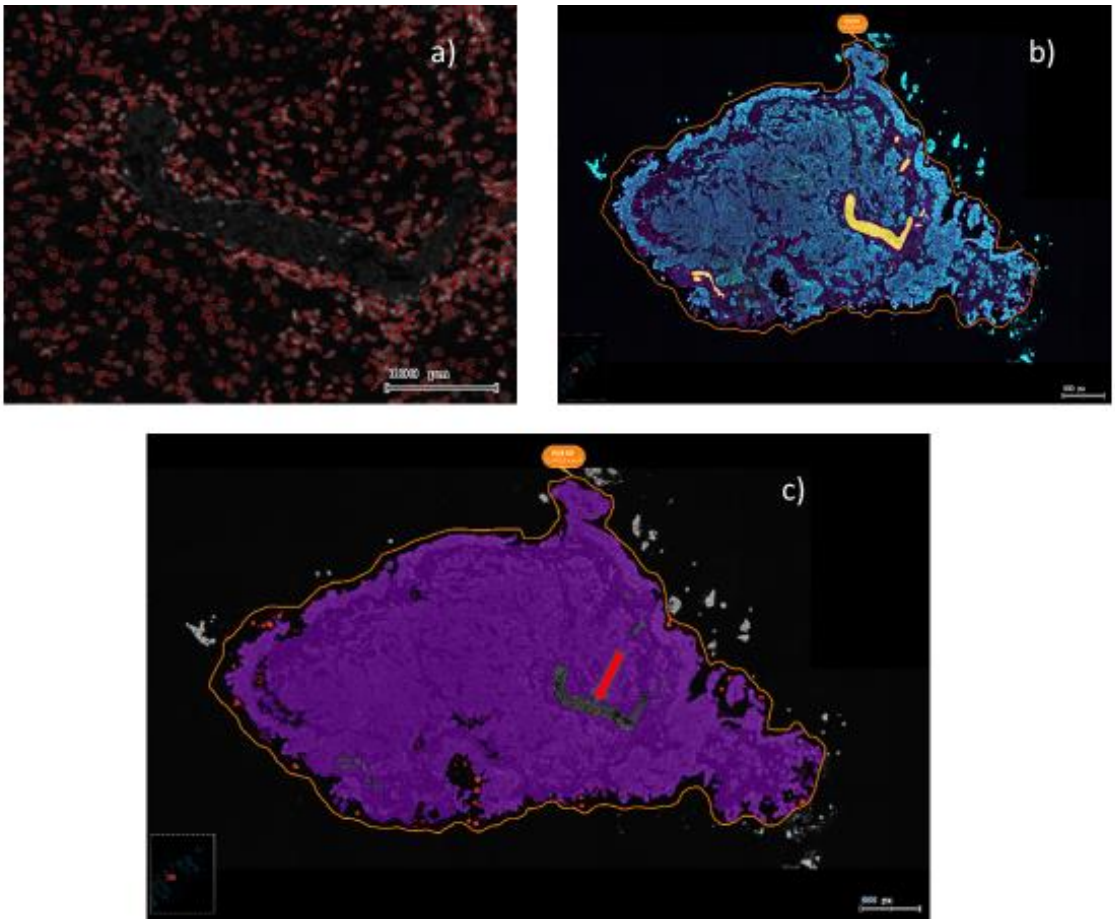

Figure 32. Lung Sample, participant of DREAM study, updated analysis after blood vessel removal. a) Nuclear Segmentation layer showing exclusion, b) Manual corrections layer: deleted tissue shown in yellow c) Tissue Mask, deleted tissue indicated by arrow.

3.7.8 Optimise nuclear size cut-off values to improve nuclear segmentation

Cut-off values

A cut-off value discriminates between true signals and false events according to cell size and intensity of fluorophore signal. An event refers to a single cell that is represented by a single dot on a scattergram, allowing for the visualisation of positive and negative cells in the source region of interest. An event is described as belonging to one of 4 sub-populations based on which quadrant the event is located.

Nuclear and Cellular Masks.

The software first creates a nuclei mask for segmented nuclei, as seen by the blue arrow in figure 33. b) and then creates a cell mask, as seen by the yellow arrow that surrounds and encompasses the nuclear mask. A nuclear mask is generated based on detection of DAPI and nuclear size measurements and is then applied to all cells on the tissue mask. The sum of individual fluorophore signals within the cell mask is normalised by dividing by area (μm^2). Scattergrams have been assigned a 75% upper mean threshold to exclude dim unrepresentative cells. The mean intensity of fluorophore signal in a cell mask is examined and cells with the lowest 25% fluorophore signal in the cell mask are excluded from appearing as events on scattergrams. Cell masks containing dim signal (< 25% mean fluorophore signal intensity) are considered not to be representative of a true positive cell.

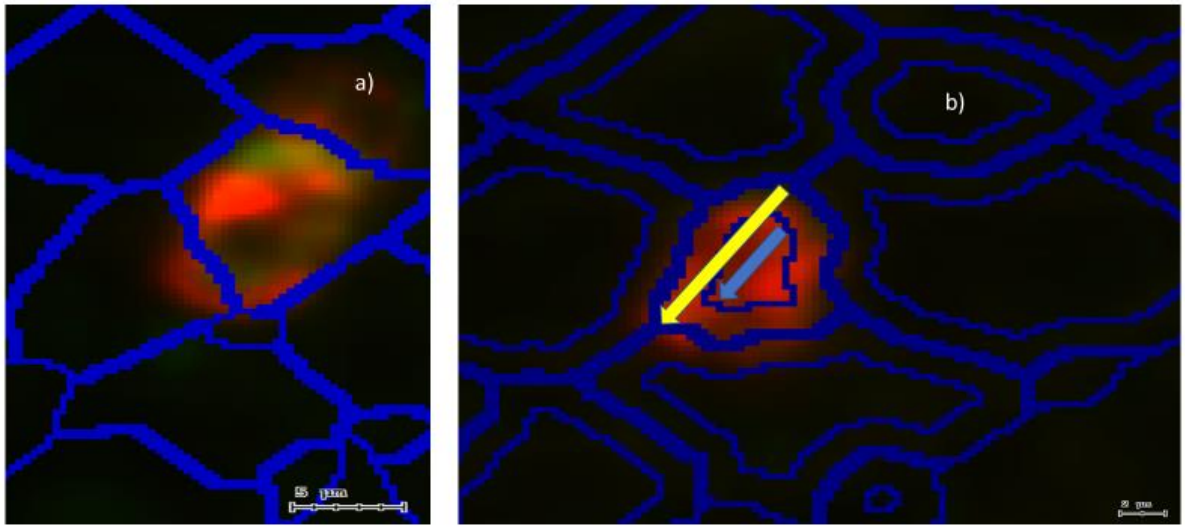

Figure 33. 20x Magnification. Lung sample, participant DREAM study participant. a) $CD8^+PD\text{-}1^+$ cell mask layer: segmented $CD8^+PD\text{-}1^+$ cell. b) Cell segmentation Mask layer: for CD8 cell showing inner nuclear mask with a blue arrow and outer cellular mask with a yellow arrow.

As the microtome blade cuts tissue block sections, it dissects nuclei at various angles, resulting in small nuclear fragments appearing in the nuclear segmentation layer as indicated by the yellow arrows in figure 34. b). Nuclear debris is not representative of nuclei in the cell population and must be excluded from analysis. Increasing the nuclear cut-off size for nuclei included on the tissue mask excludes smaller fragments, nuclear size cut-offs across samples ranged in size from 8 μm^2 - 30 μm^2. The scattergram in figure 34. a) plots $PD\text{-}1^+$ cells on the y-axis against nuclear size (um^2) on the x axis. It is

clear from the left-hand tail of the cell population there are numerous small nuclear fragments, that are represented by yellow arrows in figures 34.a).

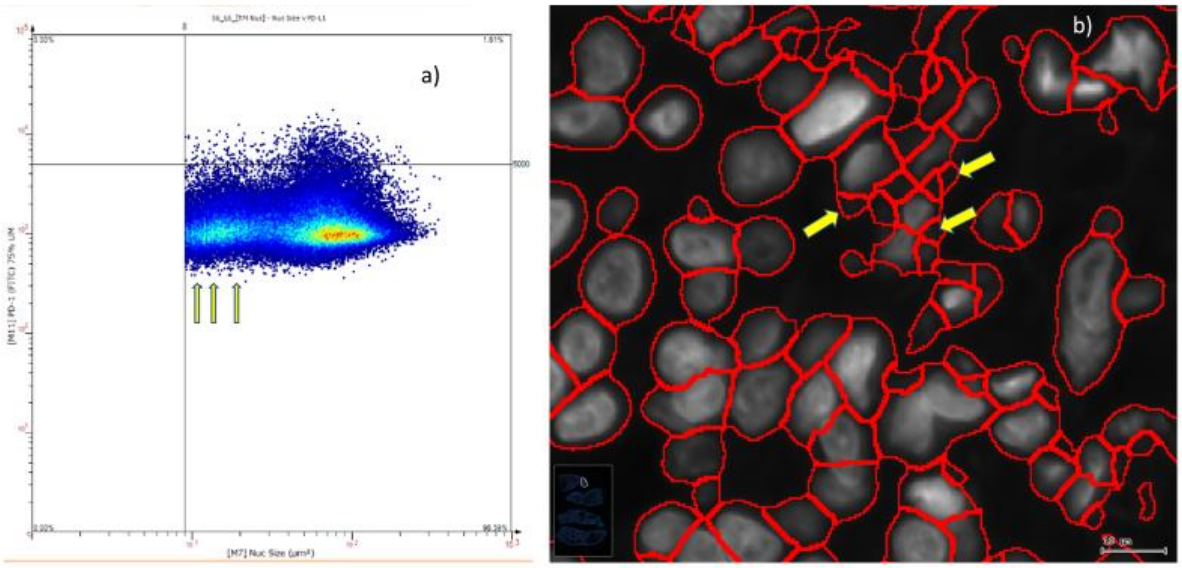

Figure 34. Lung Sample, participant of DREAM study a) Scattergram: PD-1+ expression vs. nuclear size (µm²), b) Nuclear segmentation layer: backward data showing all nuclei for right quadrants.

The real time backward gating tool links the data on the scattergram back to the image. Gated cell subpopulations are detected within the image. To determine the optimal nuclear size cut-off, a gate is drawn around the tail of the cell population as demonstrated in figure 35.a). Events contained within gate are indicated in red in the nuclear segmentation layer as seen in figure 35.b).

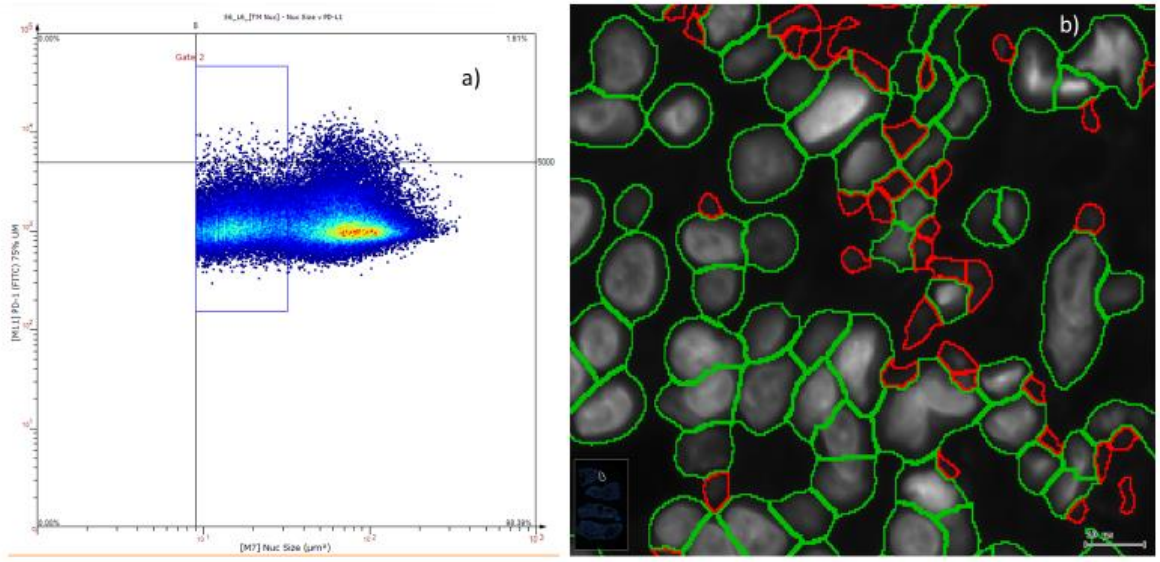

Figure 35. Lung sample, participant of DREAM study a) Scattergram: PD-1 expression vs nuclear size (µm²), gated cellular fragmentation population. b) Nuclear segmentation layer: backward data for gated cellular fragmentation population indicated in red.

The optimal nuclear size, having been validated through backward gating is then applied to the software and the nuclear segmentation layer is updated as seen in figure 36. a) and over segmentation is improved by the removal of nuclear debris as indicated in figure 36. b).

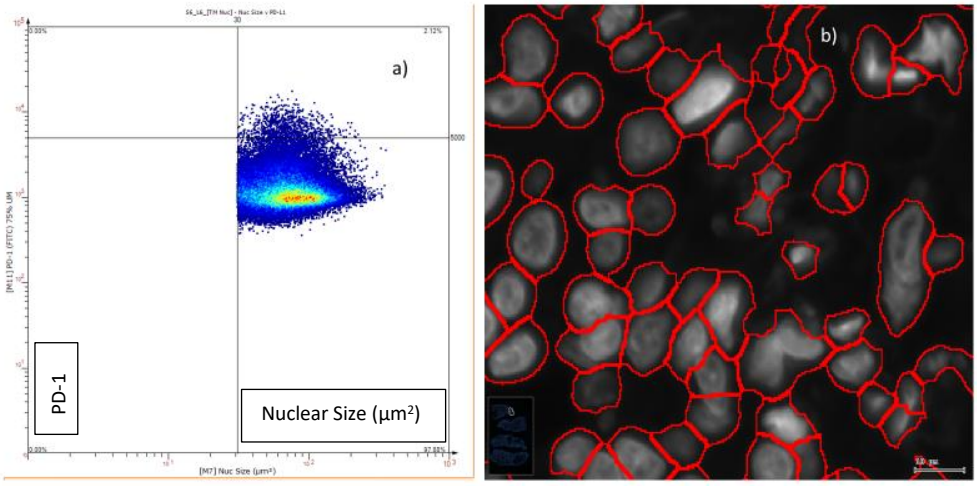

Figure 36. Lung sample, participant of DREAM study. a) Scattergram: PD-1 expression vs Nuclear Size Cut-off (µm²) vs. b) Nuclear segmentation layer: Backward data updated to show cells now excluded from the nuclear segmentation layer.

3.7.9 Optimise cut-off values for positive PD-1 (FITC), PD-L1 (Cy5), CD8 (SpRed) and Cytokeratin (SpGold) expressing cells

PD-1 (FITC) Channel

Biological autofluorescence is prevalent in the FITC channel as seen in figure 37 b). Cut-off values for FITC signal need to be high enough to exclude dim auto fluorescent cells, as indicated by yellow arrows in figure 37. b). Cut-offs must remain low enough to include true positive PD-1 expressing cells, indicated by red arrows in figure 37. b). The real time forward gating tool links data on the image back to the scattergram. Double clicking the mouse on any cell in the image (as indicated by the blue arrow in figure 37. b.) will shows the position of that cell on the scattergram as indicated by the red box in figure 37. a).

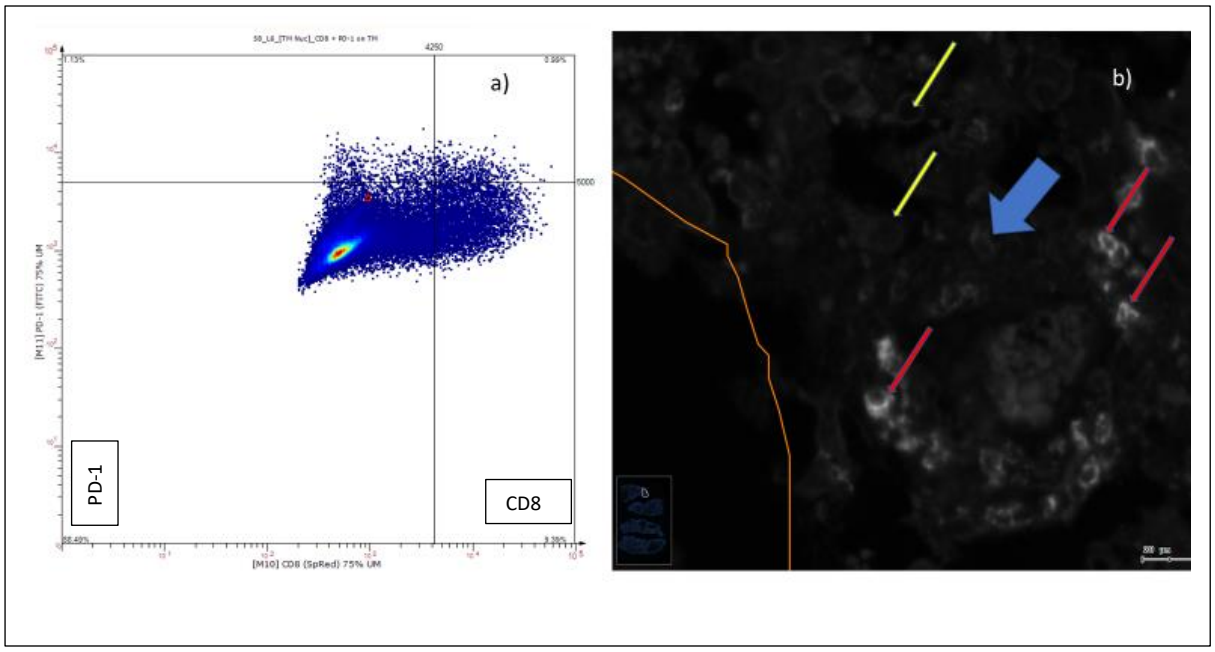

Figure 37. Lung sample, participant of DREAM study. a) Scattergram: PD-1 vs. CD8 cell population, with a single dim FITC expressing cell highlighted by a red box. b) FITC channel, showing dim FITC, indicated by the blue arrow, and represented by a red box when using forward gating as seen in figure 37. a). & yellow arrows indicate autofluorescence.

Forward gating is used as an initial guide to set cut-off values and ensure that true positive cells are being displayed in positive quadrants of the scattergram. Next backward gating is used to segment all cells in a red line that fall within the scattergram's positive quadrants, as seen in figure 38.

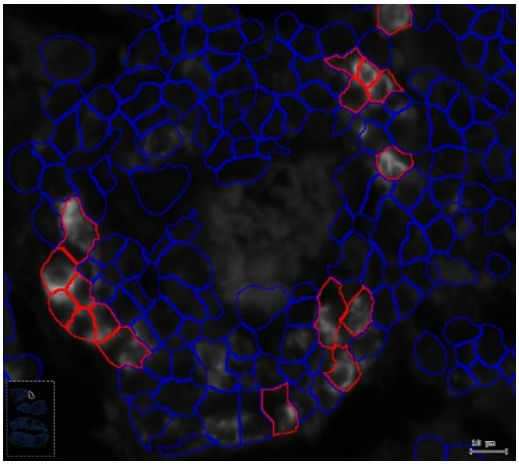

Figure 38. Lung tissue sample, participant of DREAM study. Nuclear segmentation layer overlaid onto PD-1 (FITC) channel: Shows backward data for positive quadrants from scattergram 38 a). red indicates segmented cells of positive quadrants.

To further refine cut-off values a narrow gate is configured to show cells that fall within a range of 1000 pixels below the cut-off value as seen in figure 39. a). The backward gating tool shows cells contained within this narrow gate indicated in red in the image as seen in figure 39. b). This is done to ensure the cut-off is not too high and that the excluded cells in this gate are true negative cells.

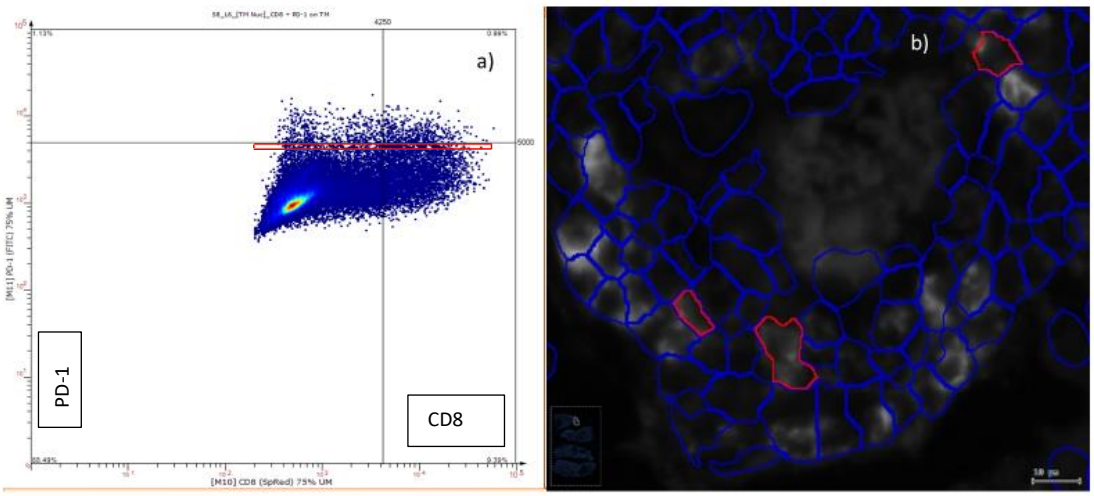

Figure 39. Patient lung Sample. a) Scattergram: CD8 vs PD-1, cell population gated just below PD-1 cut-off b) Nuclear segmentation layer overlaid onto PD-1 (FITC) channel: backward data shown for gated population in scattergram 39. a).

A narrow gate is also configured to include cells within a range of 1000 pixels above the cut-off value as seen in figure 40. a). Cells within this gate are indicated in red as seen in image 40. b) these are dim

true positive cells. If there are more false positive cells than true positive cells within the gate, the cut-off value needs to be increased. Background staining should be excluded to reduce the noise to signal ratio.

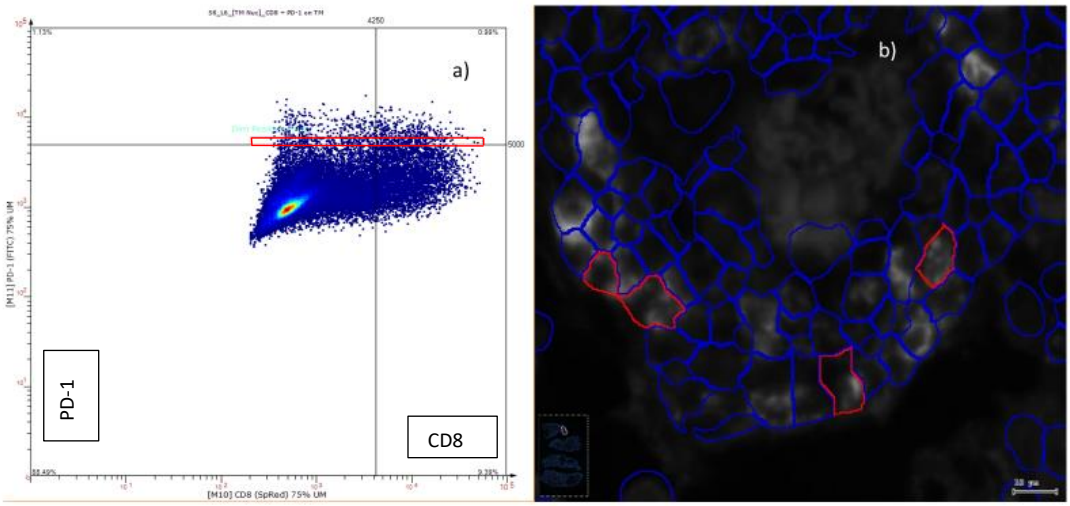

Figure 40. Lung Sample, participant of DREAM study. a) Scattergram PD-1 vs.CD8, cell population gated cell just above PD-1 cut-off. b) Nuclear segmentation layer overlaid onto PD-1 (FITC) channel: backward data for gated population in scattergram 40. a) is shown in red, indicating dim true positive PD-1 cells.

PD-L1 (Cy5) Channel

The cut-off for PD-L1 (Cy5) was determined using the same approach outlined for setting PD-1 (FITC) cut-off values.

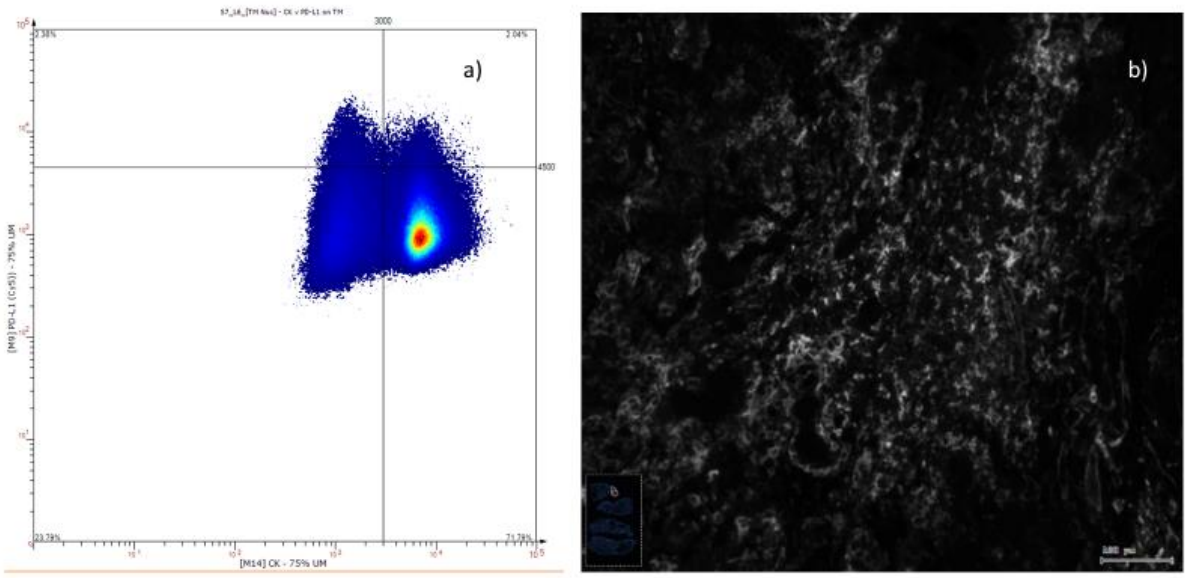

Figure 41. Lung Sample, participant in DREAM study. a) Scattergram PD-L1 vs. Cytokeratin b) PD-L1 (Cy5) channel.

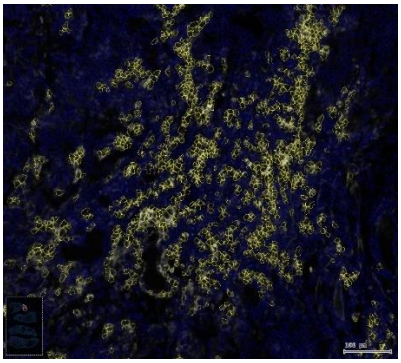

Figure 42. Lung sample, participant in DREAM study. Nuclear Segmentation layer overlaid onto PD-L1 (Cy5) channel: Showing backward gating for upper quadrants (PD-L1⁺ cells), gated cells in upper quadrants are segmented in yellow.

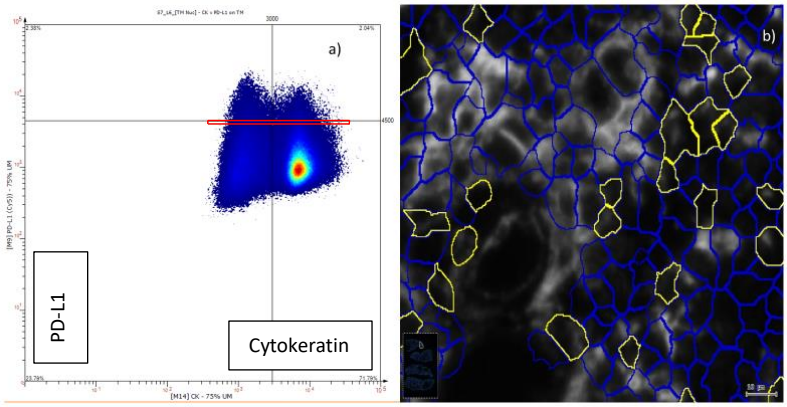

Figure 43. Lung sample, participant of DREAM study. a) Scattergram: PD-L1 vs. Cytokeratin expression, gated cell population just below PD-L1 cut-off. b) Nuclear segmentation layer overlaid onto PD-L1 (Cy5) channel: backward data for gate in scattergram 43 a).

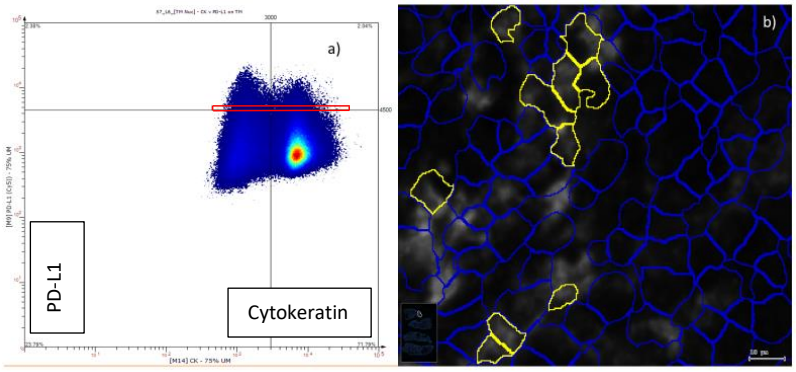

Figure 44. Lung sample, participant of DREAM study, a) Scattergram: PD-L1 vs Cytokeratin, gated cell population just above PD-L1 cut-off, b) Nuclear segmentation layer overlaid onto PD-L1 (Cy5) channel: backward data for gated population in scattergram 44. a) is displayed, cells within gate are segmented in yellow.

CD8 (SpRed) Channel

The cut-off for CD8 (SpRed) was determined using the same approach outlined for establishing PD-1 (FITC) cut-off values.

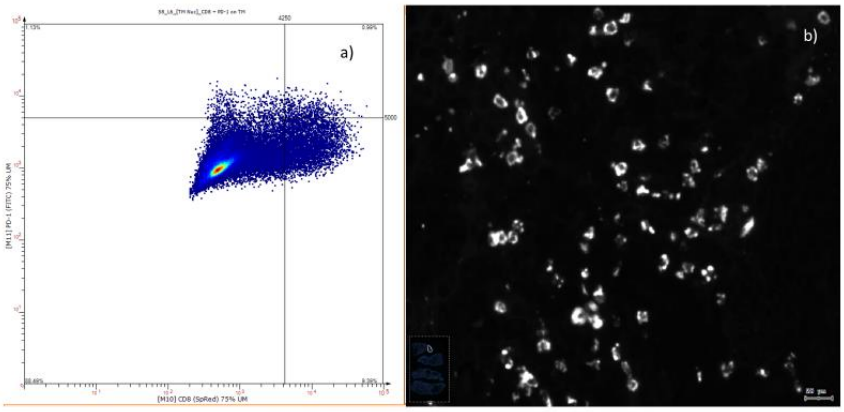

Figure 45. Lung Sample, participant of DREAM study. a) Scattergram PD-1 vs.CD8 expression, b) CD8 (SpRed) fluorophore channel.

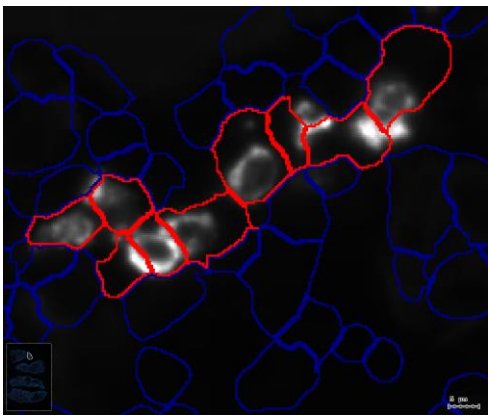

Figure 46. Lung Sample, participant. Nuclear segmentation layer overlaid onto CD8 (SpRed) channel: backward data viewed for positive right quadrants in scattergram 46. a). $CD8^{+}$ cells are segmented in red.

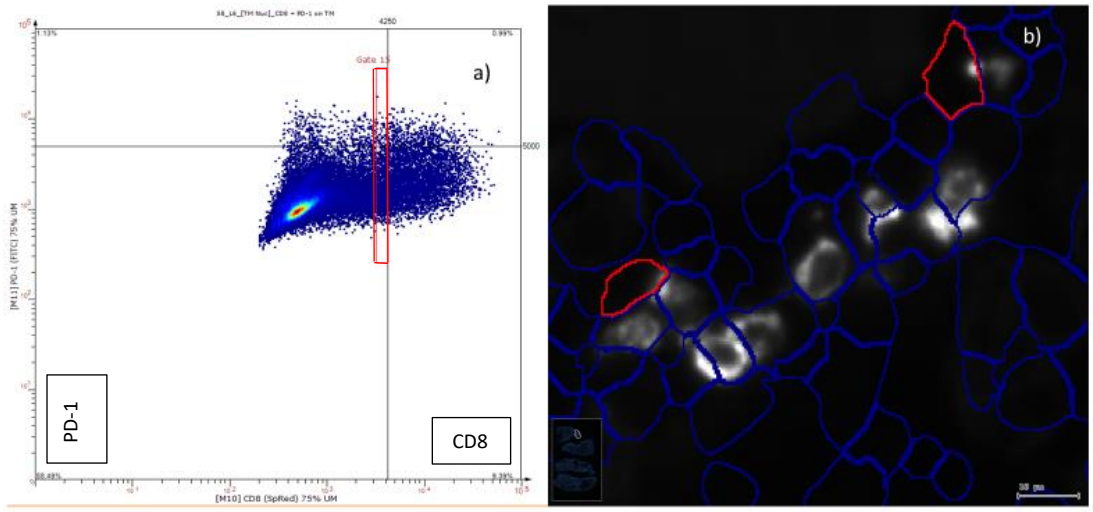

Figure 47. Lung sample, participant of DREAM study. a) Scattergram PD-1+ vs. CD8 cells, gated cell population just below CD8 cut-off. b) Nuclear segmentation layer overlaid onto CD8 (SpRed) channel: backward data for gated cell population in 47. a) indicated in red.

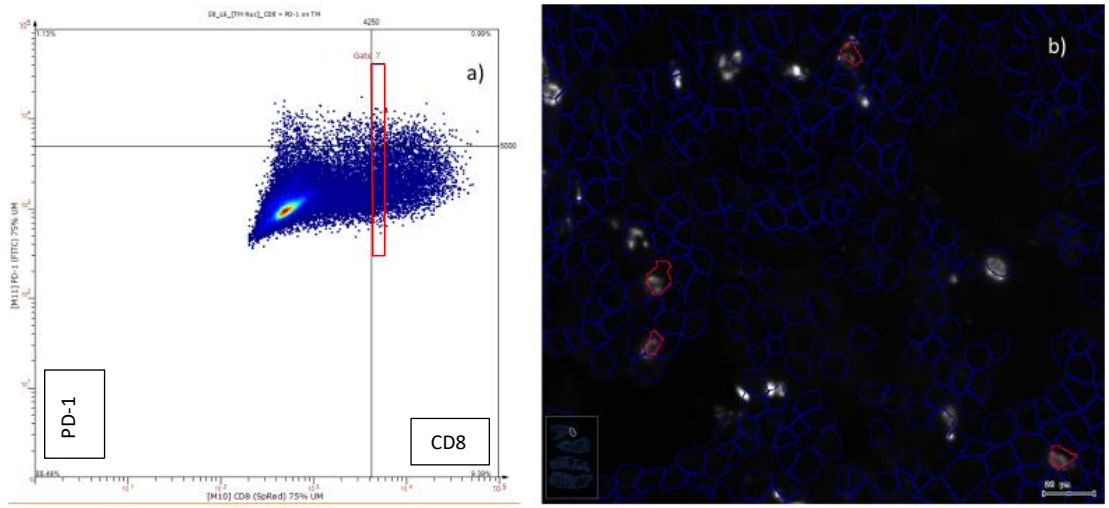

Figure 48. Lung sample, participant in DREAM study. a) Scattergram PD-1 vs. CD8 cells, gated cell population just above CD8 cut-off. b) Nuclear segmentation layer overlaid onto CD8 (SpRed) channel: backward data for gated cell population in 48. a) indicated in red.

Cytokeratin (SpGold) Channel

The cut-off for cytokeratin (SpGold) was determined using the same approach outlined for establishing PD-1 (FITC) cut-off values.

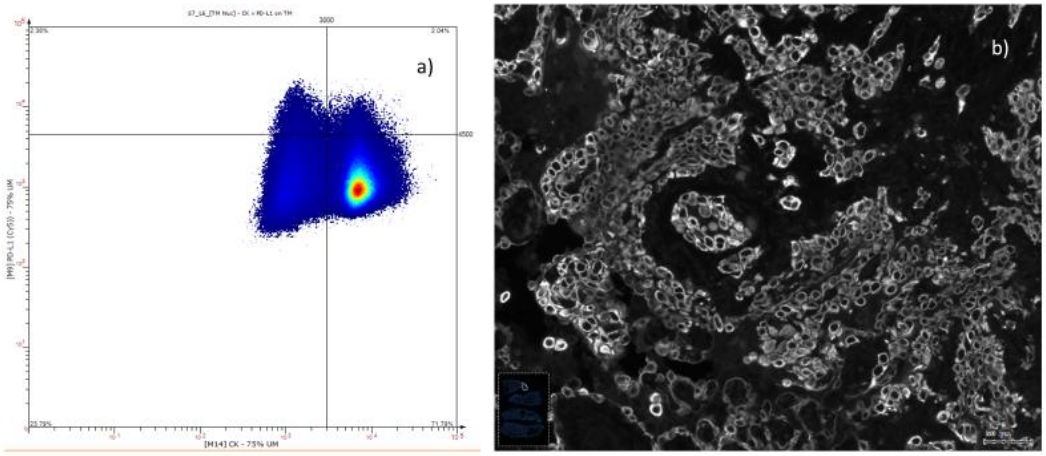

Figure 49. Lung sample, participant in DREAM study. a) Scattergram PD-L1 vs. Cytokeratin b) Cytokeratin (SpGold) fluorophore channel indicating tumour epithelium.

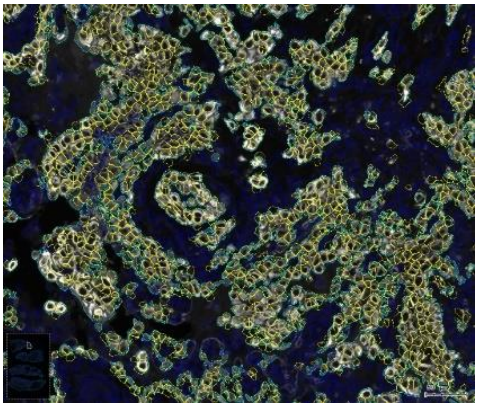

Figure 50. Lung Sample, participant in DREAM study. Nuclear segmentation layer overlaid onto epithelium mask detection layer, then overlaid onto cytokeratin (SpGold) channel. Backward data for right quadrants for scattergram in figure 49. a) is shown. Positive cytokeratin cells are in yellow and the aqua blue outline indicates epithelium mask.

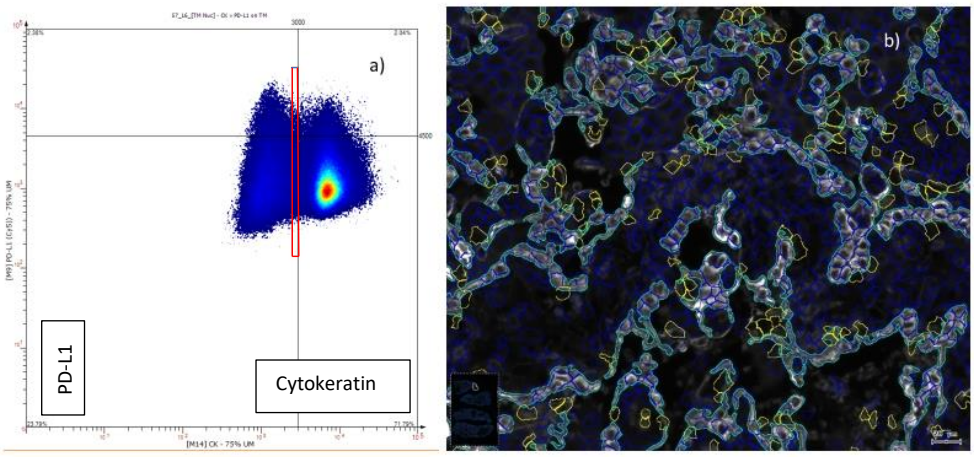

Figure 51. Lung sample, participant in DREAM study. a) Scattergram: PD-L1 vs. cytokeratin cells, gated population just below cytokeratin cut-off. b) Nuclear segmentation layer over laid onto epithelium mask detection layer then overlaid onto cytokeratin (SpGold) channel. Backward data for gated cell population showing cells just below the cytokeratin cut-off in yellow, aqua blue outline shows epithelium mask.

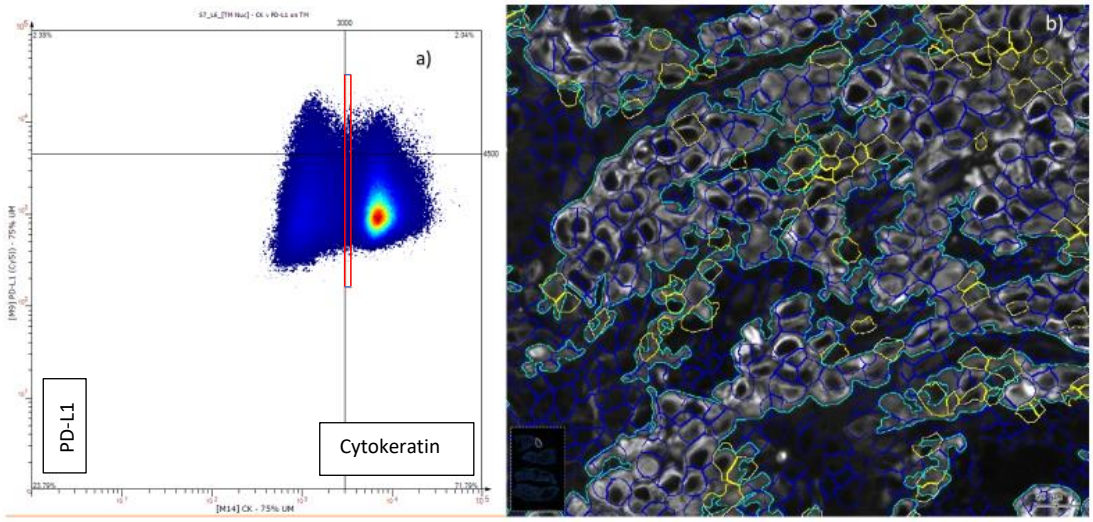

Figure 52. Lung sample, participant from DREAM study. a) Scattergram: PD-L1 vs. cytokeratin cells, showing gated cell population just above cytokeratin cut-off. b) Nuclear segmentation layer, over laid onto epithelium mask detection layer, overlaid onto cytokeratin (SpGold) channel. Backward data for gated cell population indicated in yellow, aqua blue outline shows epithelium mask.

3.7.10 Export statistics to excel

The data was normalised by area (cells/mm^2) to compare data readouts amongst samples.

3.8 CONTROLS

3.8.1 Biological controls

Positive, negative and antibody isotype control slides were included in each batch during the slide preparation and image acquisition stage. A single FFPE tissue block containing multiple TMA samples was used to produce serial sections for all control slides, in all batches. TMA tissue, as seen in figure 53 included:

Human tonsil – PD-1.

Placenta – PD-L1.

Skin – Cytokeratin.

Lung – Minimal PD-L1 & PD-1.

Graded lung cancer – PD-1, PD-L1, Cytokeratin and CD8.

Graded colorectal cancer – PD-1, PD-L1, Cytokeratin and CD8.

The positive control, seen in figure 54, showed positive signals in the appropriate fluorophore channels and the negative control, seen in figure 55, showed only DAPI staining alongside expected dim autofluorescence in the FITC channel. Isotype controls were used to set display levels for each fluorophore channel and determine any autofluorescence that may be present in each fluorophore channel (figures 56 – 59).

Note: In batch 4 which consisted of 5 samples, the PD-1 isotype control slide was damaged and was unable to scanned alongside the other slides. The positive and negative control slides were still scanned, and the positive slide showed appropriate PD-1 expression when compared to the negative slide. This indicates that the PD-1 channel has correctly detecting positive PD-1 fluorophore signal during scanning of slides.

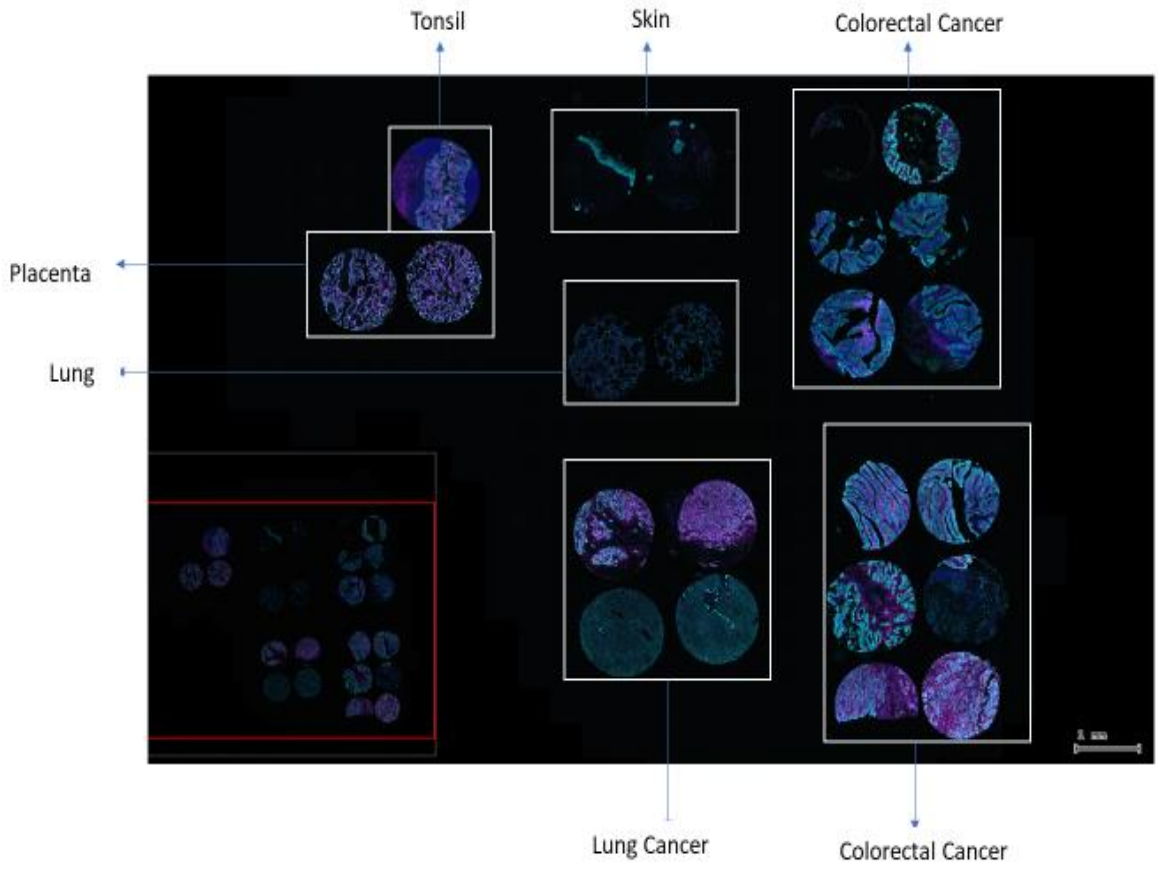

Figure 53. TMA control map.

Positive Control slides

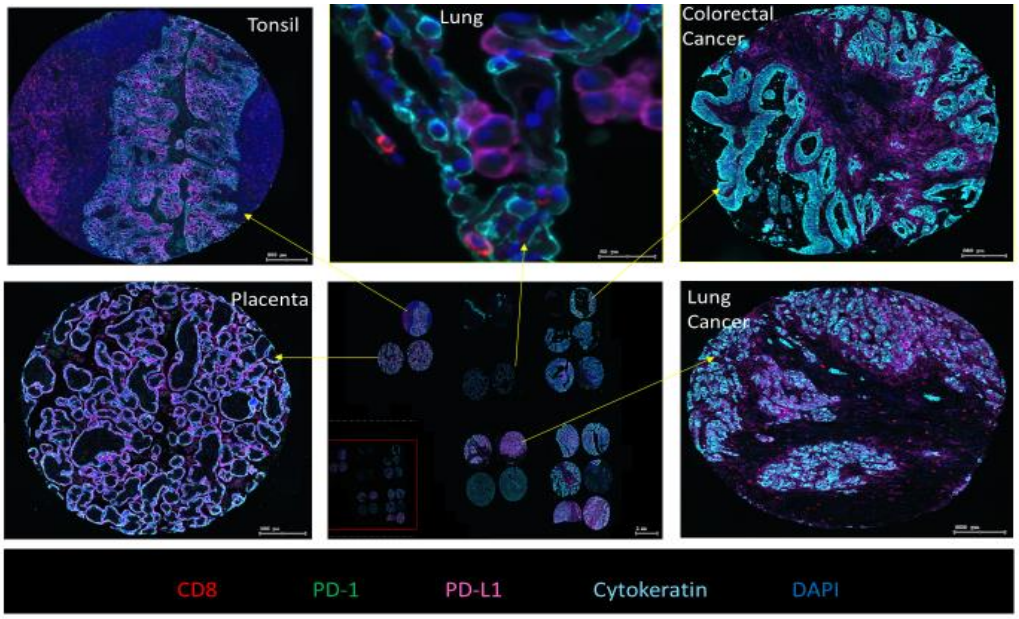

Figure 54. Positive control TMA map showing CD8, PD-1, PD-L1, cytokeratin and DAPI expression in tonsil, lung, placenta and colorectal cancer tissue.

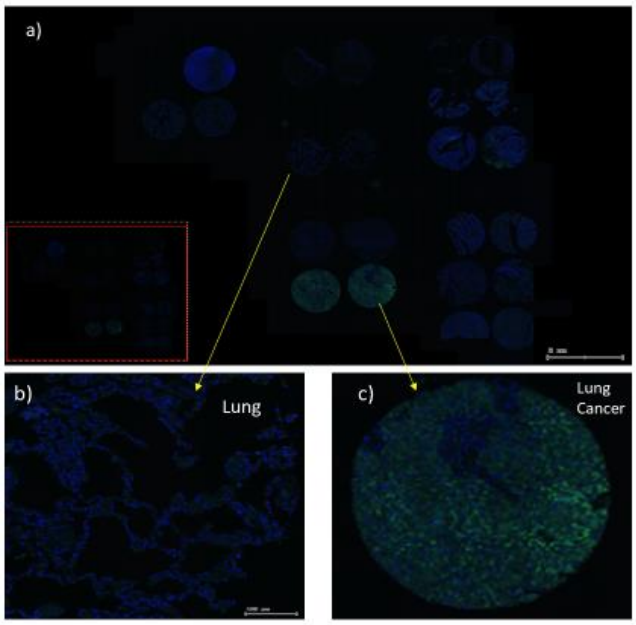

Figure 55. Negative Control. a) Overlay Channel: Negative Control TMA b) Overlay channel: Lung tissue c) Overlay channel: Lung cancer tissue: Autofluorescence present in PD-1 (FITC) channel.

Cytokeratin (SpGold) control slide

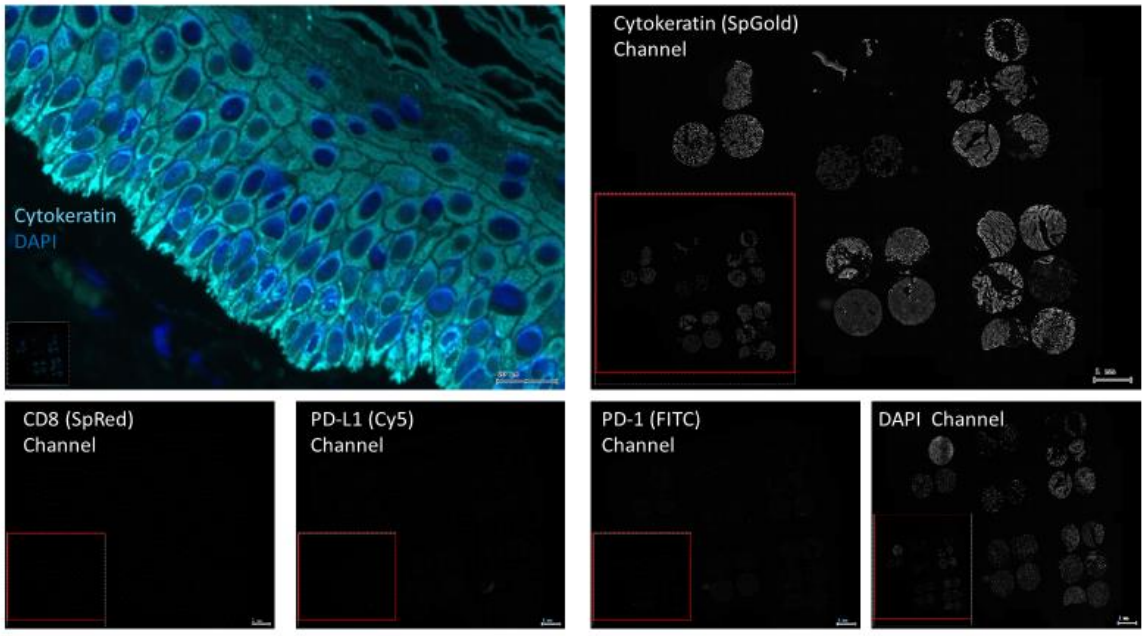

Figure 56. Cytokeratin antibody isotype control displaying cytokeratin expression in the CD8 channel, cytokeratin channel, PD-L1 channel, PD-1 channel and DAPI channel.

CD8 (SpRed) control slide

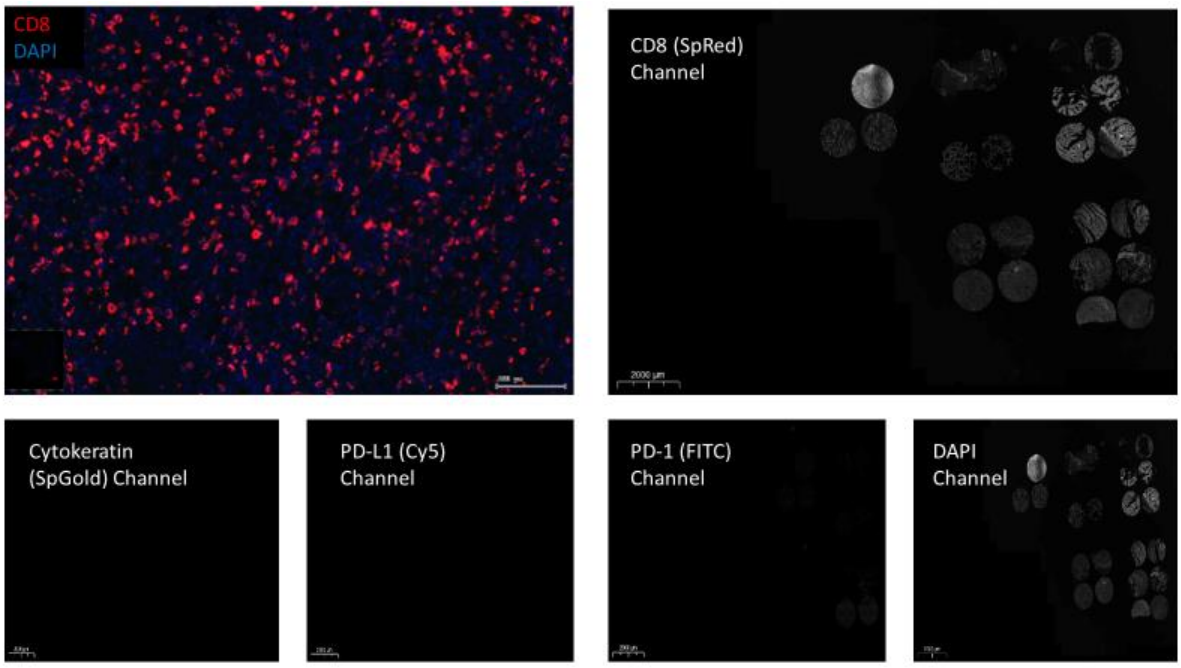

Figure 57. CD8 antibody isotype control displaying CD8 expression in the CD8 channel, cytokeratin channel, PD-L1 channel, PD-1 channel and DAPI channel.

PD-L1 (Cy5) control slide

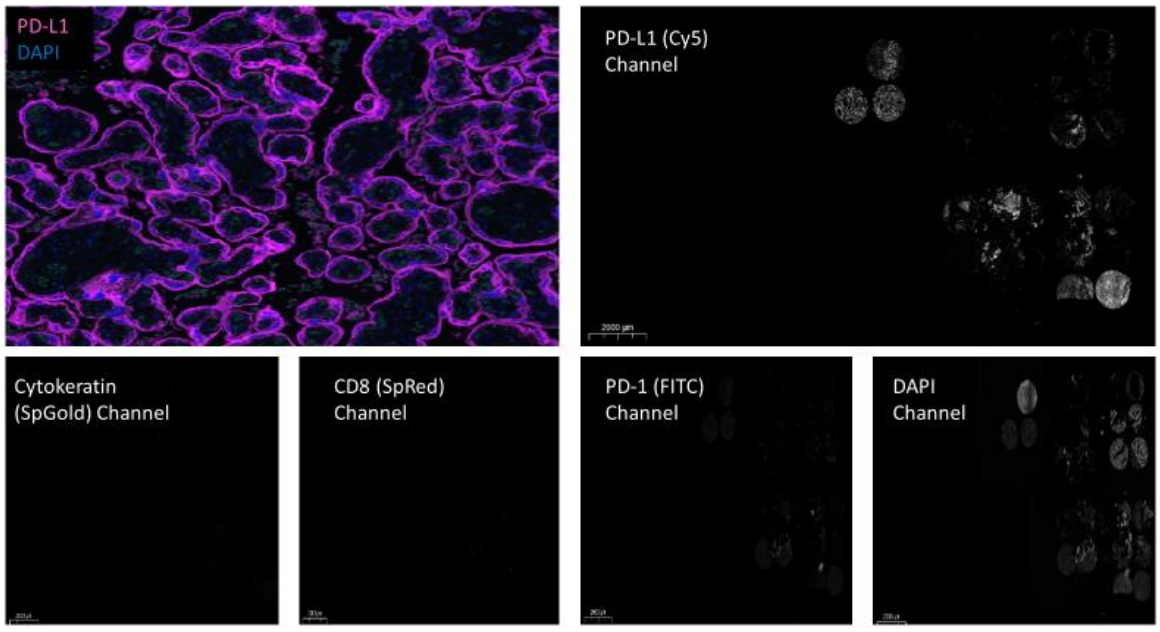

Figure 58. Cy5 antibody isotype control displaying Cy5 expression in the CD8 channel, cytokeratin channel, PD-L1 channel, PD-1 channel and DAPI channel.

PD-1 (FITC) control slide

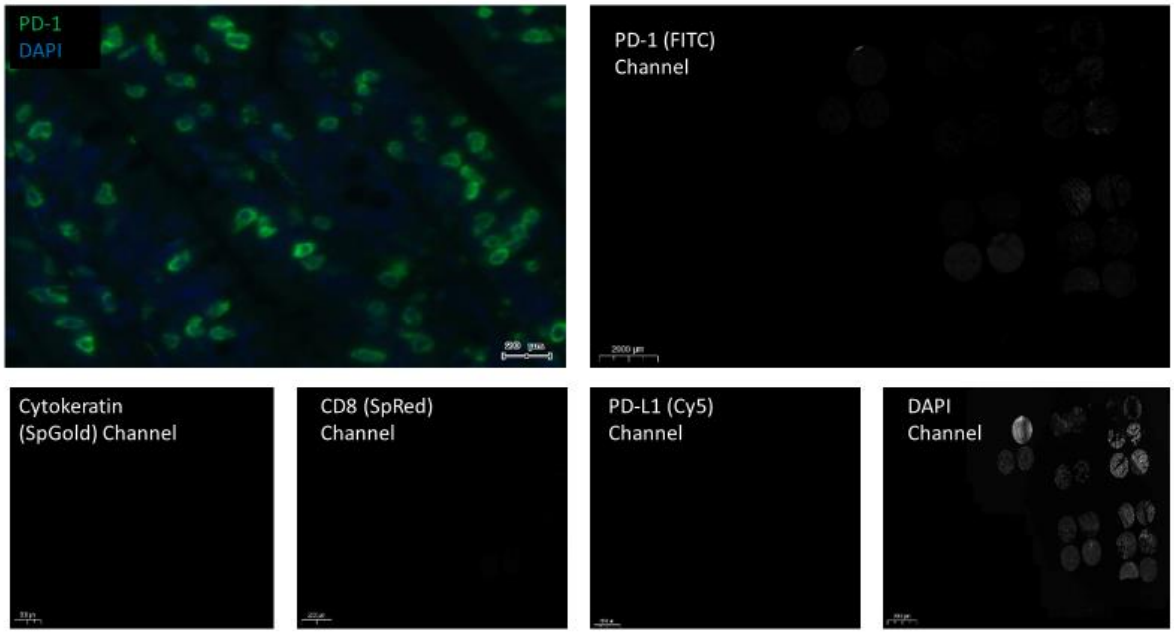

Figure 59. FITC antibody isotype control. a) Overlay channel b) PD-1 (FITC) channel c) CD8 (SpRed) channel d) Cytokeratin (SpGold) channel e) PD-L1 (Cy5) Channel f) nuclei (DAPI) channel.

3.8.2 Technical controls

- Excitation/emission filter sets used were kept constant for all slides within the same batch (table 7)

- Identical camera exposure times for fluorophore channels in same batch (table 8).

- Display levels: the same for each fluorophore channel within a batch (table 9).

- All samples across all batches were analysed using the same optimised thresholds set in the layer editor menu (table 10).

3.9 STATISTICAL ANALYSIS WORKFLOW

1. Correlate % of PD-L1 on the tissue mask to manual CPS.

- Linear regression, goodness of fit test – (GraphPad Prism 8.2.1).

(*Aim 1: Compare sensitivity of manual PD-L1 scoring against automated PD-L1 scoring).*

2. Compare CD8, PD-1 and PD-L1 markers between tumour epithelium, stromal cells and combined tissue.

- Mann U Whitney, test of difference (GraphPad Prism 8.2.1).
- Kruskal – Wallis, test – (GraphPad Prism 8.2.1).

(*Aim 2: Quantify tumour cells, stromal cells and combined tissue markers and associate to PD, SD & PR).*

3. Test for difference between CD8, PD-1 and PD-L1 expression in tumour cells, stromal cells and combined tissue and associate with PD, SD and PR.

- Mann U Whitney, test of difference (GraphPad Prism 8.2.1).
- Kruskal – Wallis, test – (GraphPad Prism 8.2.1).

(Aim 2: Quantify tumour cells, stromal cells and combined tissue markers and associate to PD, SD & PR).

4. Test the trend for % of PD-L1 expressed on tumour epithelium amongst PD, SD and PR groups.

- 2x2 matrix Fisher's exact, test of association – (GraphPad Prism 8.2.1).

(Aim 3: Hypothesize why patients are tipped into a new state phase (PR) and identify predictive biomarkers)

5. Correlate PD-L1 with CD8 and $CD8^{+}PD\text{-}1^{+}$ on tumour epithelium, stromal cells and combined tissue.

- Linear regression, goodness of fit test – (GraphPad Prism 8.2.1).

(*Aim 3: Hypothesize why patients are tipped into a new state phase (PR) and identify predictive biomarkers)*

6. Stratify participants into 1 of 4 tumour type groups (PD-L1^{+}HighCD8^{+}PD-1^{+}, PD-L1^{-}HighCD8^{+}PD-1^{+}, PD-L1^{+}LowCD8^{+}PD-1^{+} and PD-L1^{-}LowCD8^{+}PD-1^{+}), using ≥ 5% PD-L1 on tumour epithelium and associate tumour type to treatment response (PD, SD & PR).

- 2x2 matrix Fisher's exact, test of association – (GraphPad Prism 8.2.1).

(*Aim 3: Hypothesize why patients are tipped into a new state phase (PR) and identify predictive biomarkers)*

4 RESULTS

4.1 AUTOMATED PD-L1 SCORING HAS GREATER SENSITIVITY OVER MANUAL SCORING.

Automated PD-L1 scoring using digital image analysis software StrataQuest™ demonstrated increased sensitivity in detection of PD-L1 expression compared to manual pathologist visual estimation. Tissue sections cut from the same FFPE tissue sample blocks were processed using an IHC chromogen assay to stain PD-L1, slides were then manually scored by a pathologist using the CPS. Paired tissue sections were also processed using a multiplex immunofluorescence and analyzed digitally, the percentage of PD-L1 expressed on the tissue mask, which is analogous to the CPS was calculated. The results of both techniques were plotted against each other, and the goodness of fit test returned a significant R squared value of 0.6631 (figure 60), signaling variation between samples in approximately 1/3 of cases.

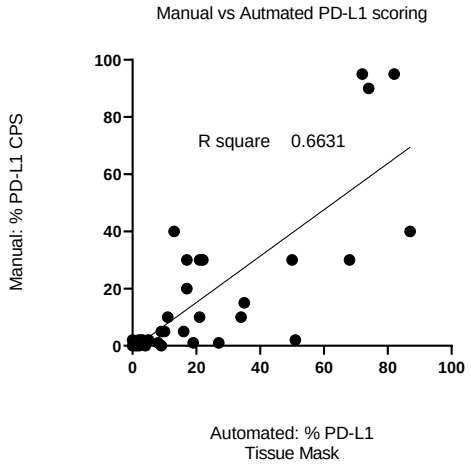

Figure 60. The % of PD-L1 expression is determined by manual CPS score versus % of PD-L1 expression on the tissue mask determined by digital image analysis for the DREAM study (n=48). Goodness of fit test returned an R square value of 0.6631.

Applying a 1% cut-off, manual scoring classified 8 (16.6%) of participants as having PD-L1 negative tumours, whom were later classified as PD-L1 positive using automated scoring. Repeating the comparison using a 5% cut-off, 5 (10.4%) of participants were classed as PD-L1 negative via manual scoring, whom were later deemed to be PD-L1 positive using automated scoring.

4.2 PD-L1 AND PD-1 EXPRESSION IS NOT SIGNIFICANTLY DIFFERENT BETWEEN TUMOUR, STROMA AND TISSUE MASKS.

There is no significant difference in PD-1 density on tumour epithelium or stromal cells, p value 0.2546 (figure 63). No significant difference is reported for PD-L1 measured in density, p value 0.4969 (figure 62) or as a % of area, p value 0.3501 (figure 61) between epithelium tumour or stromal cells. To gain insight into role PD-1 and PD-L1 have in the TME these markers need to be quantified with CD8 T cell expression.

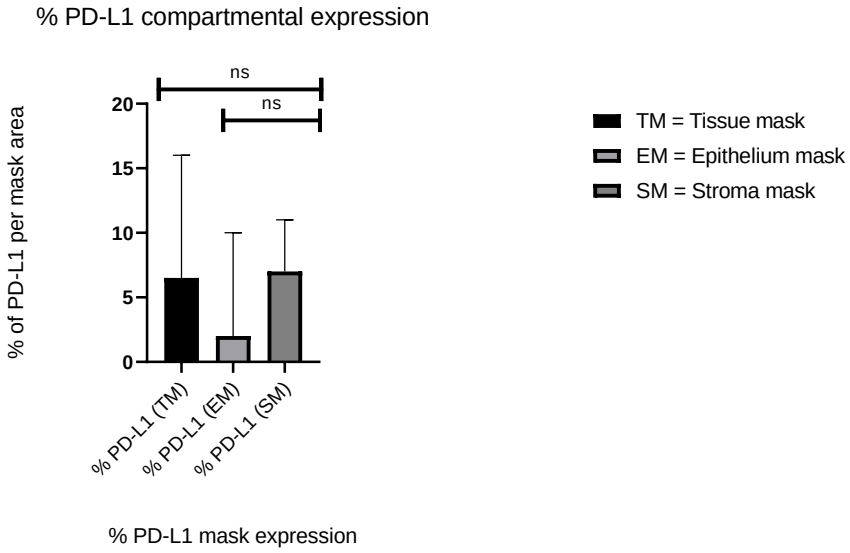

Figure 61. PD-L1 expression as a % of tissue, epithelial and stroma mask area, Mann-Whitney U, two-tailed test between EM and SM, p value 0.3501. Kruskal-Wallis, test between TM, EM and SM, p value 0.6252. Median PD-L1 on tissue mask 6.5%, epithelium mask 2% and stroma mask 7%.

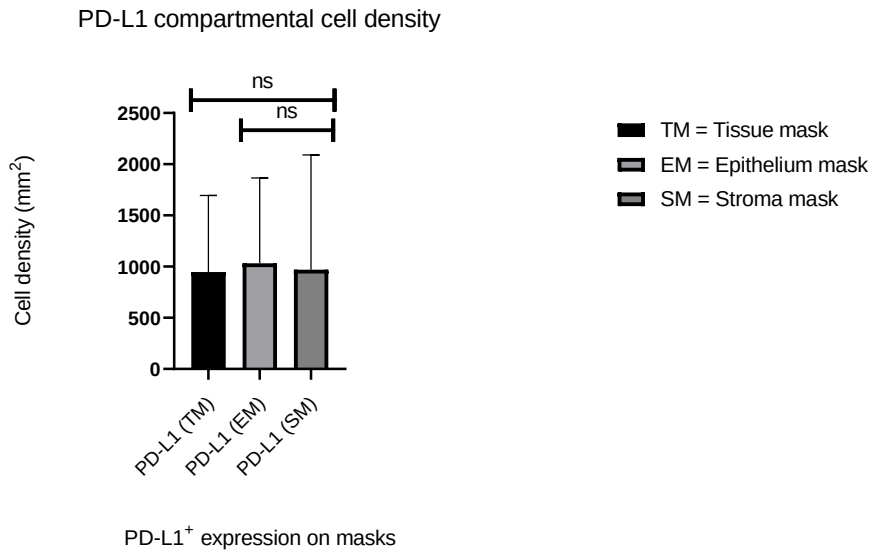

Figure 62. PD-L1 density on tissue, epithelial and stroma masks, Mann-Whitney U, two-tailed test between EM and SM, p value 0.4969. Kruskal-Wallis, test between TM, EM and SM, p value 0.6192. Median PD-L1 cell density on tissue mask is 946.0 mm², epithelial mask is 1031.5 mm²and stroma mask is 969.5 mm².

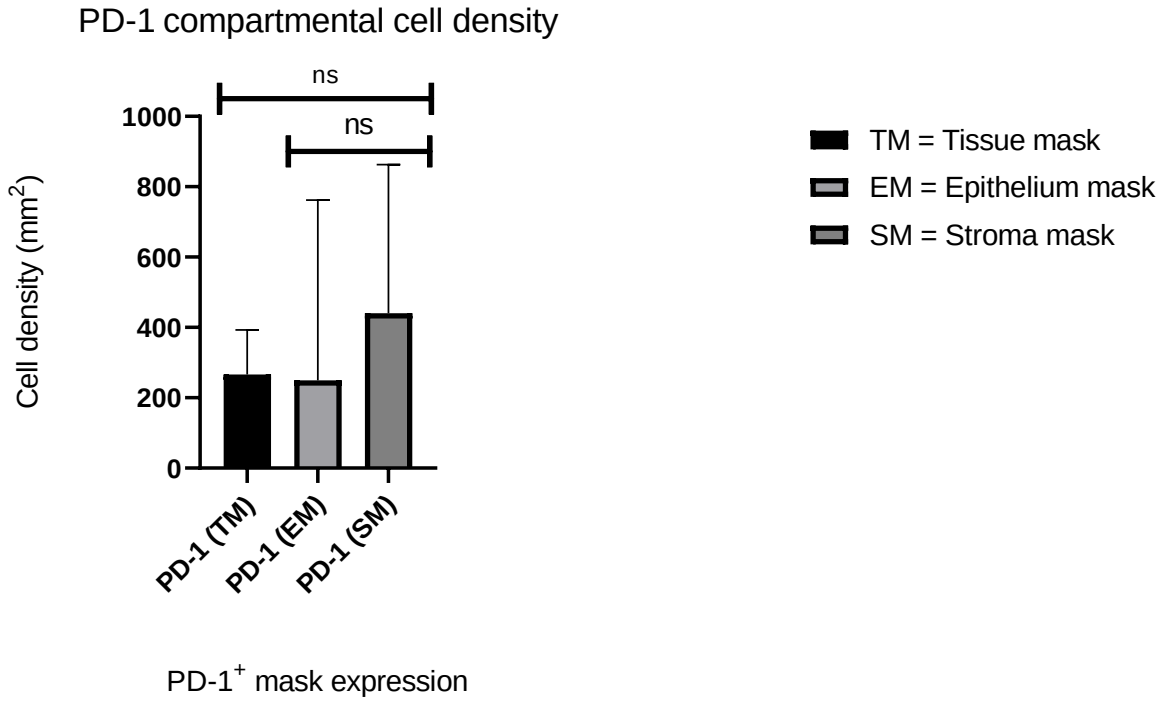

Figure 63. PD-1 cell density on tissue, epithelial and stroma mask, Mann Whitney U, two-tailed test between EM and SM, p value 0.2546. Kruskal-Wallis test between TM, EM and SM, p value 0.1942. Median PD-L1⁺ cell density on tissue mask is 266.5 mm², epithelium mask 249.5 mm² and stroma mask is 440.0 mm².

4.3 CD8 EXPRESSION IS SIGNIFICANTLY DIFFERENT BETWEEN TUMOUR, STROMAL AND COMBINED TISSUE.

Median density of stromal CD8 T cells is significantly higher compared to median epithelium CD8 T cells, 664.5 mm^2 vs 212.0 mm^2 respectively, p value 0.0006 (figure 64). Indicating that CD8 T cells are either not able to recognize and traffic to the tumour site, or there is a physical barrier preventing entry into the tumour. These findings are indicative of immune processes, to shed more light onto what these processes are cellular co-localization is measured.

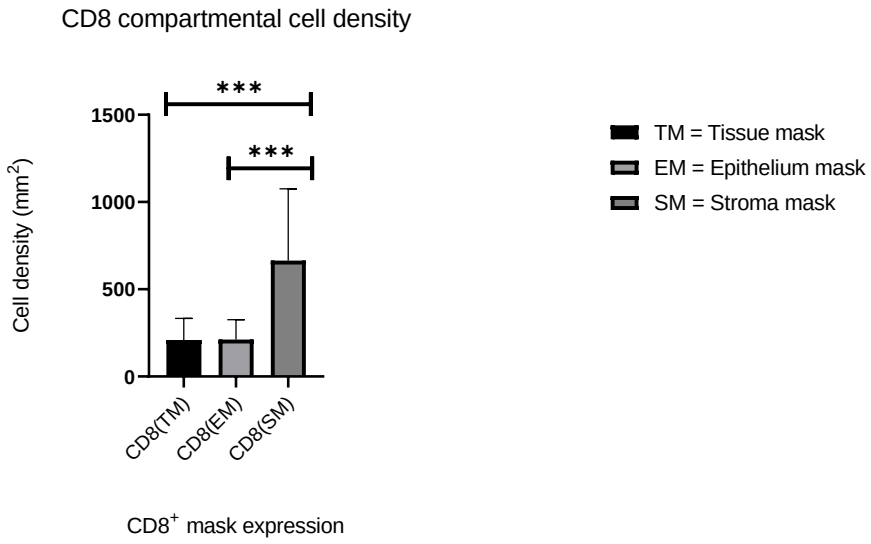

Figure 64. CD8 T cell density on tissue, epithelial and stroma mask, Mann Whitney U, two-tailed test between EM and SM, p value 0.0006. Kruskal-Wallis test between TM, EM and SM, p value 0.0007. Median $CD8^+$ cell density on tissue mask is 209.5 mm^2, epithelium mask 212.0 mm^2 and stroma mask is 664.5 mm^2.

4.4 PD-1^+ AND/OR PD-$L1^+$ CO-EXPRESSED WITH $CD8^+$ IS SIGNIFICANTLY DIFFERENT BETWEEN TUMOUR EPITHELIUM AND STROMAL CELLS.

PD-1 gains significance when colocalized with CD8 T cells, $CD8^+PD1^-$ cell density is significantly higher amongst stromal cells than tumour epithelium, p value 0.0435 (figure 65). $CD8^+PD\text{-}1^+PD\text{-}L1^+$ expression is also significantly different between tumour epithelium and stromal cells, p value 0.0226 (figure 66).

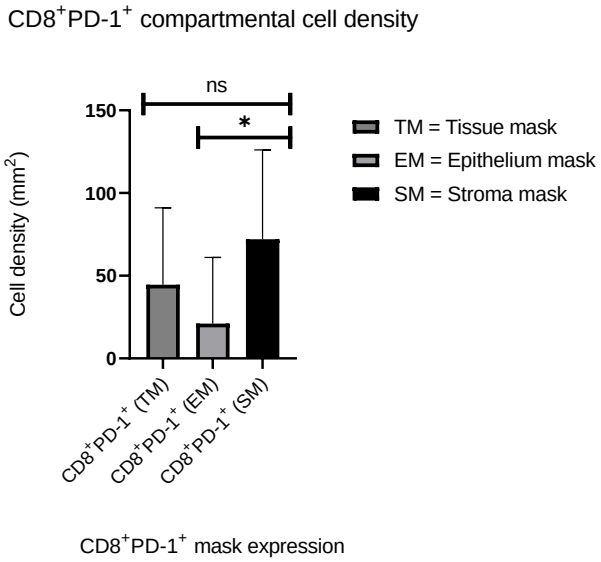

Figure 65. CD8⁺PD-1⁺ cell density on tissue, epithelial and stroma mask, Mann Whitney U, two-tailed test between EM and SM, p value 0.0435. Kruskal-Wallis test between TM, EM and SM, p value 0.1244. Median CD8⁺PD-1⁺ density on tissue mask is 44.5 mm², epithelium mask 21.0 mm² and stroma mask is 72.0 mm².

The ratio of $CD8^+PD\text{-}1^+$:CD8 is similar in both tumour epithelium and stroma cells, ~ 1:9 and ~ 1:10 respectively, with median densities of 21.0 mm^2:212.0 mm^2 and 72.0mm^2:664.5mm^2 respectively (figures 64 & 65). Median $CD8^+PD\text{-}1^+PD\text{-}L1^+$ cell density is lower on tumour epithelium than stromal cells (3.0 mm^2 vs. 18.5 mm^2 respectively), with the ratio of $CD8^+PD\text{-}1^+PD\text{-}L1^+$ to $CD8^+PD\text{-}1^+$ being ~ 1:7 and ~ 1:4, in the tumour epithelium and stromal cells respectively (figures 66 & 65). The ratio of potentially anergy inducing $CD8^+PD\text{-}1^+PD\text{-}L1^+$ T cells to activated $CD8^+PD\text{-}1^+$ is higher amongst stromal CD8 compared to tumour epithelium CD8. This could be suppressing CD8 T cell activation and migration to the tumour site. To look at these ratios in a different light, the ratio of $CD8^+PD\text{-}1^+$ to $CD8^+PD\text{-}1^+PD\text{-}L1^+$ for tumour epithelium is ~ 21:3 and, the ratio of $CD8^+PD\text{-}1^+$ to $CD8^+PD\text{-}1^+PD\text{-}L1^+$ for stromal cells is ~ 72:18.5, potentially an indication of less immunosuppression and higher activation on tumour cells. In order to tell if certain cell densities may be advantageous to treatment outcome, cell density is compared across PR, SD and PD groups.

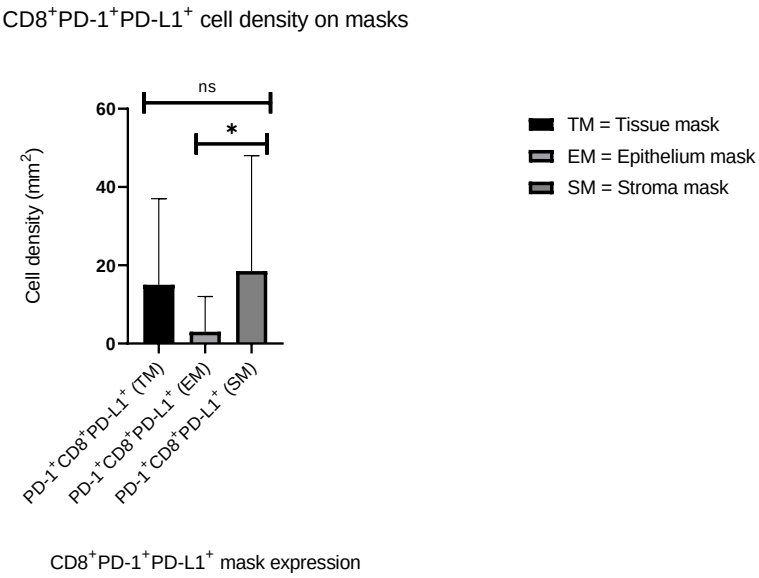

Figure 66. PD-1⁺CD8⁺PD-L1⁺ cell density on tissue, epithelial and stroma mask, Mann Whitney U, two-tailed test between EM and SM, p value 0.0226. Kruskal-Wallis test between TM, EM and SM, p value 0.0589. Median PD-1⁺CD8⁺PD-L1⁺ density on tissue mask is 15.0 mm², epithelium mask 3.0 mm² and stroma mask is 18.5 mm².

4.5 PD-L1 DENSITY ON THE EPITHELIUM MASK IS SIGNIFICANTLY DIFFERENT BETWEEN SD AND PR GROUPS

All cell markers when compared against other markers in that mask were significantly different (appendix 1). Cellular density of CD8, PD-1, CD8⁺PD-1⁺, PD-1⁺CD8⁺PD-L1⁺ and PD-1⁺PD-L1⁺ on tumour epithelium, stromal cells and combined tissue was not statistically different between PD, SD or PR groups (Appendix 2 – 7). There was a significant difference in PD-L1 density expressed on tumour epithelium between SD and PR groups (figure 67), that significance that was lost when expressed on stromal cells or combined tissue. Median PD-L1 density on tumour epithelium is higher in the PR group compared to the SD group, 2184.0 mm² vs 556.0 mm², p value 0.0214 (figure 67).

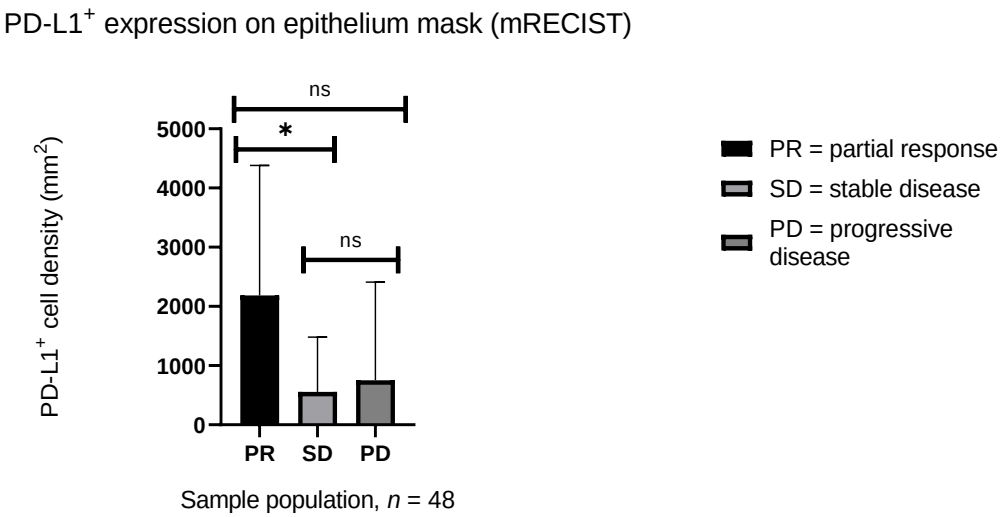

Figure. 67. PD-L1⁺ cell density between PR, SD and PD groups, Mann Whitney U, two-tailed test between PR and SD p value is 0.0214, between SD and PD p value is 0.6576 and between PD and PR p value is 0.2471. Kruskal-Wallis test between PD, SD and PR, p value 0.0589. Median PD-L1⁺ density on PR is 2184.0 mm², SD is 556.0 mm² and PD is 751.0 mm².

4.6 THE TREND FOR PD-L1 % ON TUMOUR EPITHELIUM IS ASSOCIATED WITH CLINICAL OUTCOMES

The significance of higher PD-L1 density on tumour epithelium for PR participants compared to SD participants was explored further. The trend for PD-L1 expressed on the epithelium mask between PR and SD groups was tested, using 1% and 5% PD-L1 cut-offs, p value 0.0135 (figure 68). Participants with ≥ 5% PD-L1 expression were more frequent in the PR group than SD group (64% vs 23%). The sample size was too small to repeat the trend using a 1% PD-L1 cut-off. Having established the significance of high tumour cell PD-L1 amongst PR compared to SD groups, correlations were performed with CD8 and CD8⁺PD-1⁺ to relate to immune activity.

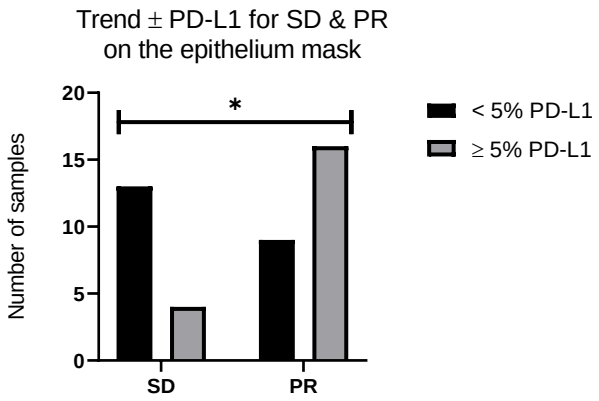

PD-L1± for SD vs PR

Data analyzed	< 5% PD-L1	≥ 5% PD-L1	Total
SD	13	4	17
PR	9	16	25
Total	22	20	42

Figure 68. Two-sided, fishers exact test, p value 0.0135, reported for trend above/below 5% PD-L1 and SD/PR.

4.7 $CD8^+PD\text{-}L1^+$ CORRELATION WITH PD-L1+ ON EPITHELIUM MASK FOR SD AND PR GROUPS

PD-L1 density was correlated with CD8 and $CD8^+PD\text{-}1^+$ on the epithelium mask (figures 69 & 70), correlations were also performed on the stroma mask to compare if finding were unique to tumour cell PD-L1 (appendix 9.b) & d)). There was no positive correlation of PD-L1 expression with either CD8 or $CD8^+PD\text{-}1^-$ cells for the PD group on the tumour, epithelium or stroma mask (appendix 10). Correlation between PD-L1 and CD8 T cells on tumour epithelium was strongest for the SD group in comparison to the PR group, R = 0.683 versus R = 0.001274, respectively (figure 70). This could be reflective of immunosuppressive factors other than PD-L1 preventing a PR.

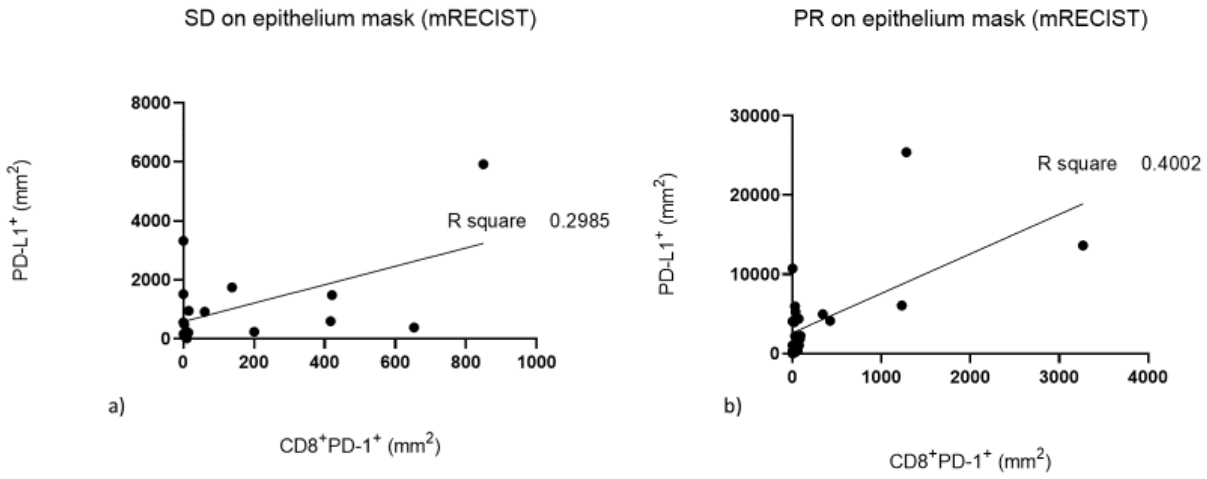

Figure 69. a) PD-L1 vs CD8⁺PD-1⁺ on tumour epithelium for SD, R squared 0.2985. b) PD-L1 vs CD8 on tumour epithelium for PR, R squared 0.40002.

The difference in R squared values for $CD8^+PD\text{-}1^+$ versus PD-L1, and CD8 versus PD-L1 on the epithelium mask for the PR group are, R = 0.402 vs R = 0.001274 respectively (figures 69. b) & 70. b).). This suggests that in the PR group, PD-L1 expression for some patients is correlated with the subpopulation $CD8^+PD\text{-}1^+$ T cells. It is tempting to speculate that for the proportion of patients for whom this correlation exists, the activated $CD8^+PD\text{-}1^+$ T cells secrete IFN-γ, driving increased PD-L1 expression on tumour cells, an adaptive immune resistance mechanism. Additionally, samples with high PD-L1 expression and minimal $CD8^+PD\text{-}1^+$ co-expression could be symbolic of oncogenic PD-L1 expression, a sign of innate immune resistance. This provides the rational to segregate participants into tumour types as proposed by Teng *et al*. based on CD8, $CD8^+PD\text{-}1^+$ and PD-L1 expression to identify those patients that when undergoing chemoimmunotherapy will be tipped into a new state and achieve PR(92).

4.8 CD8+ CORRELATION WITH PD-L1+ ON EPITHELIUM MASK FOR SD AND PR GROUPS

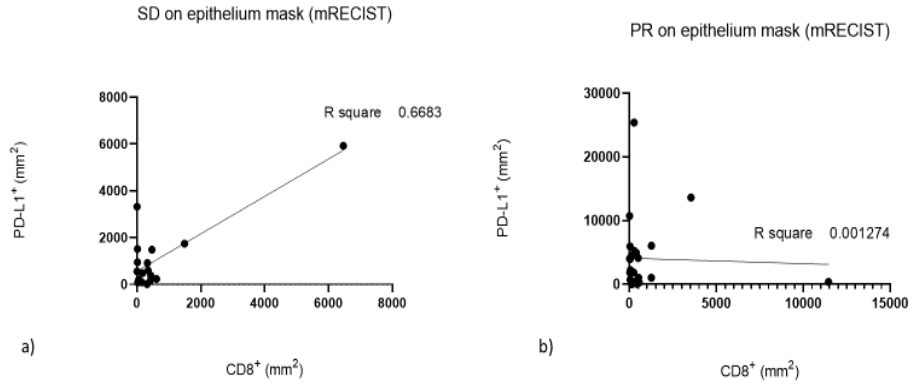

Figure 70. PD-L1 vs CD8 on tumour epithelium for SD, R squared 0.6683 b) PD-L1 vs CD8 on tumour epithelium for PR.

4.9 TUMOUR TYPE: PD-L1$^+$CD8$^+$PD-1$^+$HIGH TUMOUR TYPE IS STATISTICALLY ASSOCIATED WITH PR.

Adapting a model previously described by Taube *et. al*. patients were stratified into 4 groups based on positive or negative PD-L1 expression (above or below 5% expression on tumour epithelium), coupled with high/low CD8 or CD8$^+$PD-1$^+$ expression (above or below median density on tumour epithelium)(111). A 2x2 Fishers exact test examined the relationship between the two dimensions of the table (rows versus columns). The objective was to test for significance of association between patient response and tumour type determined by the expression of PD-L1 and CD8$^+$PD-1$^+$ TILs. There was a significant association in the PR group for PD-L1 and CD8$^+$PD-1$^+$ expression, p value 0.0099 (table 11), and no significant association for SD or PD groups. The null hypothesis that the two classifications (PD-L1 and CD8$^+$PD-1$^+$) are not different is rejected for the PR group. In the PR group type 1 tumours were significantly associated with PD-L1$^+$HighCD8$^+$PD-1$^+$, type 2 tumours were significantly associated with PD-L1$^-$LowCD8$^+$PD-1$^+$, type 3 tumours were significantly associated with PD-L1$^+$LowCD8$^+$PD-1$^+$and type 4 tumours were significantly associated with PD-L1$^-$HighCD8$^+$PD-1$^+$. Interestingly in the PR group 87% of PD-L1$^+$ participants had high CD8$^+$PD-1$^+$ expression.

Table 11. 2 sided, 2x2 matrix fisher exact test, for association between PD-L1 (< 5% & ≥ 5%) expression and CD8⁺PD-1⁺ density for patient response including PD, SD and PR (p value 1.00, p value 0.6029 and p value 0.0099 respectively).

PD (p value 1.00)

	PD-L1+	PD-L1-
HighCD8+PD-1+	Type 1 *0*	Type 4 *1*
LowCD8+PD-1+	Type 3 *2*	Type 2 *3*

SD (p value 0.6029)

	PD-L1+	PD-L1-
HighCD8+PD-1+	Type 1 *1*	Type 4 *6*
LowCD8+PD-1+	Type 3 *3*	Type 2 *7*

PR (p value 0.0099)

	PD-L1+	PD-L1-
HighCD8+PD-1+	Type 1 *14*	Type 4 *3*
LowCD8+PD-1+	Type 3 *2*	Type 2 *6*

		Number of samples/total samples (%)				
Patient Response	**Total**	PD-L1⁻ (<5%)		PD-L1⁺ (≥5%)		P value
		CD8⁺PD-1⁺ High Type 4 tumour	CD8⁺PD-1⁺ Low Type 2 tumour	CD8⁺PD-1⁺ High Type 1 tumour	CD8⁺PD-1⁺ Low Type 3 tumour	
PD	6	1/4 (25)	3/4 (75)	0/2 (0)	2/2 (100)	Ns
SD	17	6/13(46)	7/13(53)	1/4 (25)	3/4 (75)	Ns
PR	25	3/9(33)	6/9(66)	14/16 (87)	2/16 (50)	**
All	48	10/26 (38)	16/26 (61)	15/22 (63)	7/22 (36)	

The findings reported in this study for the DREAM population are that 56% of PRs have PD-L1⁺HighCD-8⁺PD-1⁺ tumours, 12% have PD-L1⁻HighCD-8⁺PD-1⁺ tumours, 24% have PD-L1⁻LowCD-8⁺PD-1⁺ tumours and 8% have PD-L1⁺LowCD-8⁺PD-1⁺ tumours (p value 0.009)(Table 11). This would indicate the patients most likely to respond to treatment would have the PD-L1⁺HighCD-8⁺PD-1⁺ tumour signature. In the SD group 5% of patients have PD-L1⁺HighCD-8⁺PD-1⁺ tumours, 35% have PD-L1⁻HighCD-8⁺PD-1⁺ tumours, 41% have PD-L1⁻LowCD-8⁺PD-1⁺ tumours and 17% have PD-L1⁺LowCD-8⁺PD-1⁺ tumours, this is not statistically significant (p value 0.602)(Table 11). In the PD group interestingly 0% of PDs have PD-L1⁺CD-8⁺PD-1⁺High tumours, 50% have PD-L1⁻CD-8⁺PD-1⁺High tumours, 16% have PD-L1⁻LowCD-8⁺PD-1⁺ tumours and 33% have PD-L1⁺LowCD-8⁺PD-1⁺ tumours, this was not statistically significant (p value 1.000) (Table11).

To establish that PD-L1 expression on the epithelium mask originated from tumour cells and not PD-L1 expressing immune cells, the percentage of cytokeratin^{+}PD-L1^{+} cells on the epithelium mask (median expression 96.5%) was calculated. The percentage of cytokeratin^{+}PD-L1^{+} was used to set positive PD-L1 cut-off thresholds (≥ 5%). Positive PD-L1 (≥ 5%) expression on tumour epithelium and association between High CD8^{+}PD-1^{+} and PD-L1 in the PR group adds weight to the hypothesis that strong adaptive immune resistance is required to tip patients from a pre-transitioned phase into a new state phase. These results do not prove the hypothesis true, instead they achieve the research aim of generating hypothesis driven by marker quantification of the TME.

4.10 TUMOUR TYPE: CD8 T CELLS AND PD-L1 ARE NOT STATISTICALLY ASSOCIATED WITH TREATMENT RESPONSE

Table 12. 2 sided, 2x2 matrix fisher exact test, for association between PD-L1 (< 5% & ≥ 5%) expression and CD8^{+} density for patient response including PD, SD and PR (p value 0.4667, p value 0.2941 and p value 1.00 respectively).

Patient Response	Total	PD-L1^{-} (<5%)		PD-L1^{+} (≥5%)		P value
		CD8^{+} High	CD8^{+} Low	CD8^{+} High	CD8^{+} Low	
PD	6	2/4 (50)	2/4 (50)	0/2 (0)	2/2 (100)	Ns
SD	17	8/13 (61)	5/13 (38)	1/4 (25)	3/4 (75)	Ns
PR	25	5/9 (55)	4/9 (44)	8/16 (50)	8/16 (50)	Ns
All	48	15/26 (57)	11/26 (42)	9/22 (40)	13/22 (59)	

Association for PD-L1 was also compared against CD8 T cells, however to significant association was reported with clinical outcomes. In this comparison 32% of PRs have PD-L1^{+}HighCD-8^{+} tumours, 20% have PD-L1^{-}HighCD-8^{+} tumours, 16% have PD-L1^{-}LowCD-8^{+}PD-1^{+} tumours and 32% have PD-L1^{+}LowCD-8^{+}PD-1^{+} tumours(Table 12).

4.11 TUMOUR TYPES: PD-L1, CD8 & PD-1 EXPRESSION

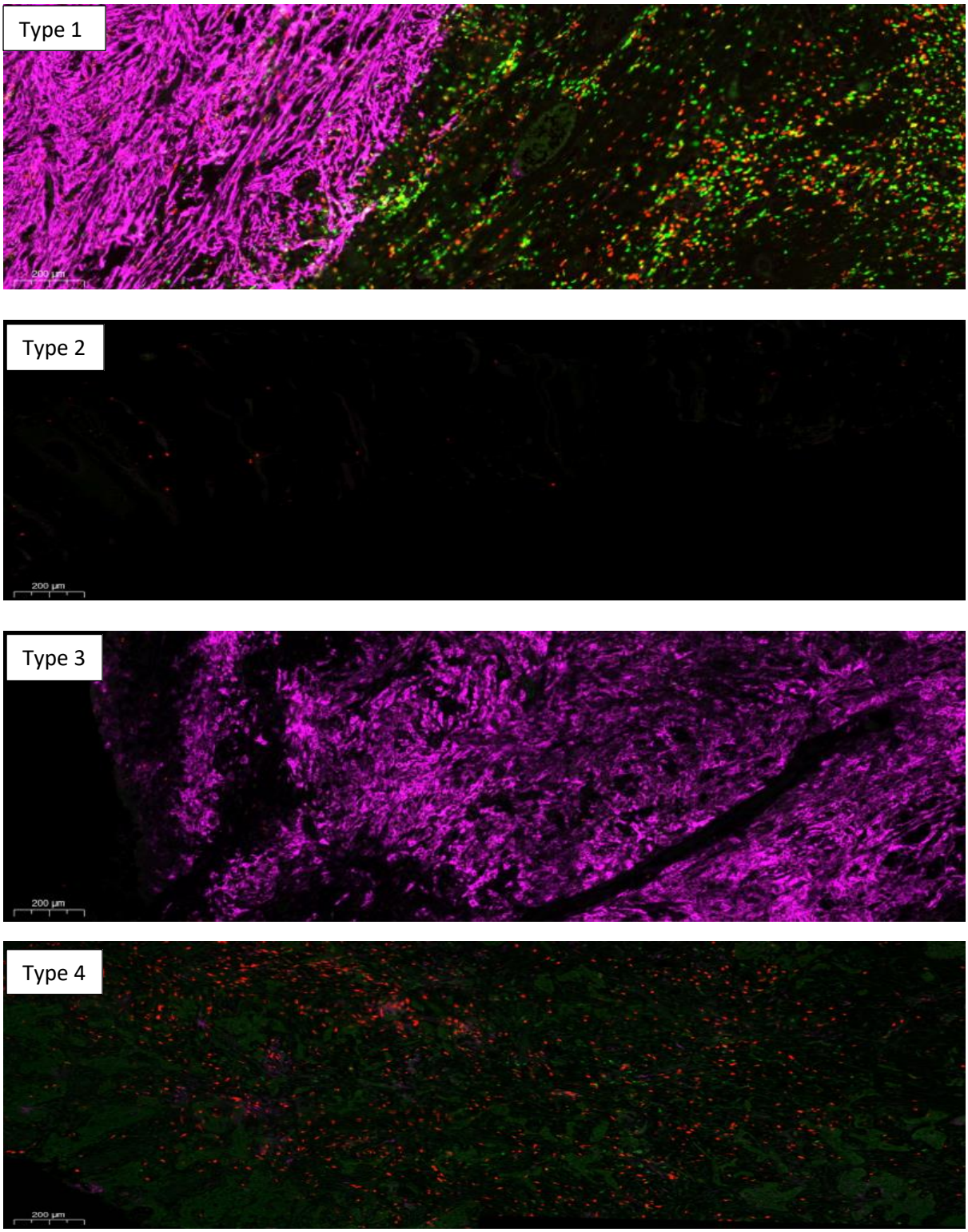

Figure 71. Overlay of PD-L1, CD8 & PD-1 fluorophore channel, displaying lung tissue samples of four different tumour types from DREAM study participants. Type 1 = PD-L1^{+}CD8^{+}PD-1^{+}High, Type 2 = PD-L1^{-}CD8^{+}PD-1^{+}Low, Type 3 = PD-L1^{+}CD8^{+}PD-1^{+}Low & Type 4 = PD-L1^{-}CD8^{+}PD-1^{+}High. PD-L1, CD8 & PD-1.

4.12 TUMOUR TYPES: PD-L1 EXPRESSION

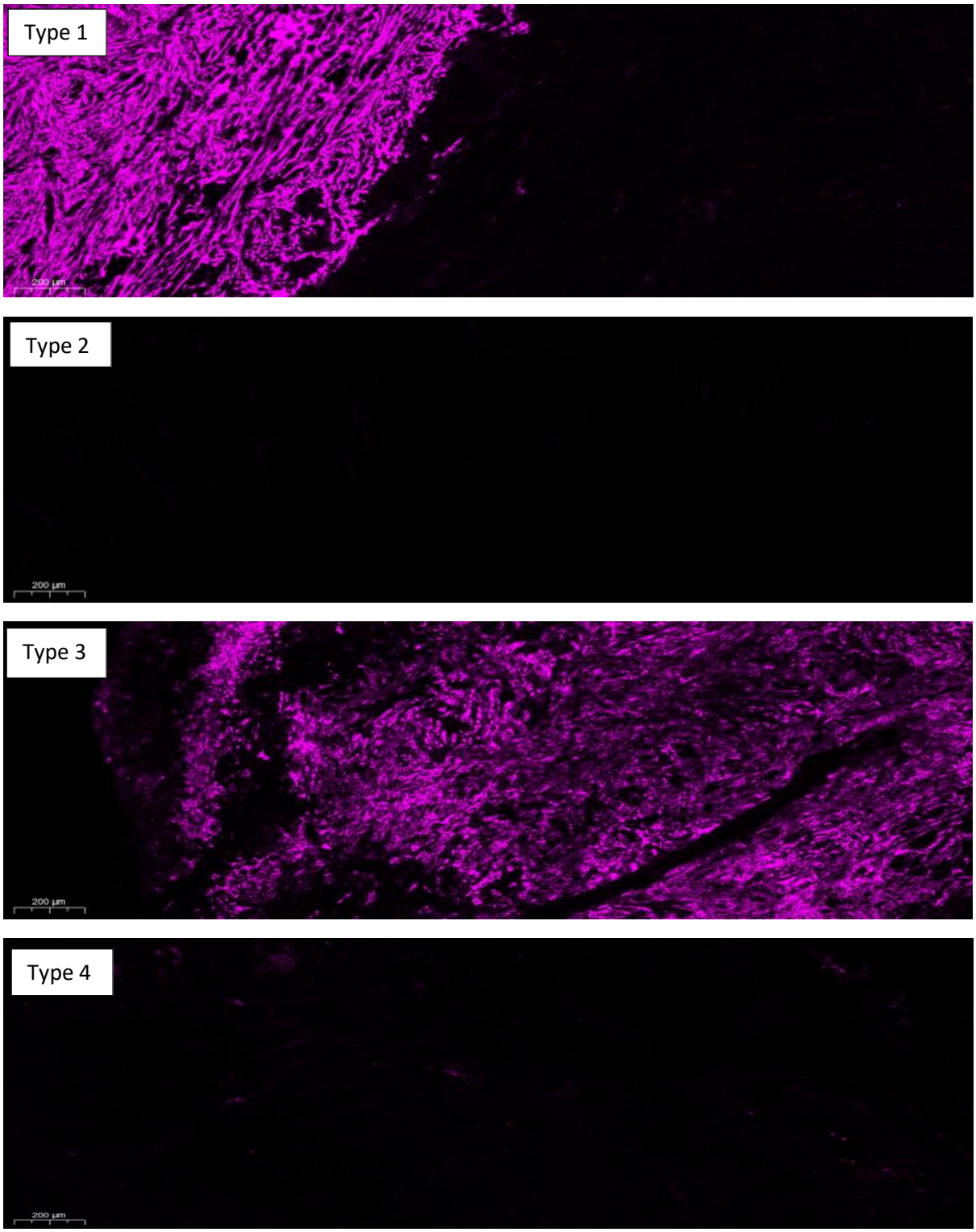

Figure 72. PD-L1 fluorophore channel, displaying lung tissue samples of four different tumour types from DREAM study participants. Type 1 = PD-L1⁺CD8⁺PD-1⁺High, Type 2 = PD-L1⁻CD8⁺PD-1⁺Low, Type 3 = PD-L1⁺CD8⁺PD-1⁺Low & Type 4 = PD-L1⁻CD8⁺PD-1⁺High. PD-L1.

4.13 TUMOUR TYPES: CD8 & PD-1 EXPRESSION

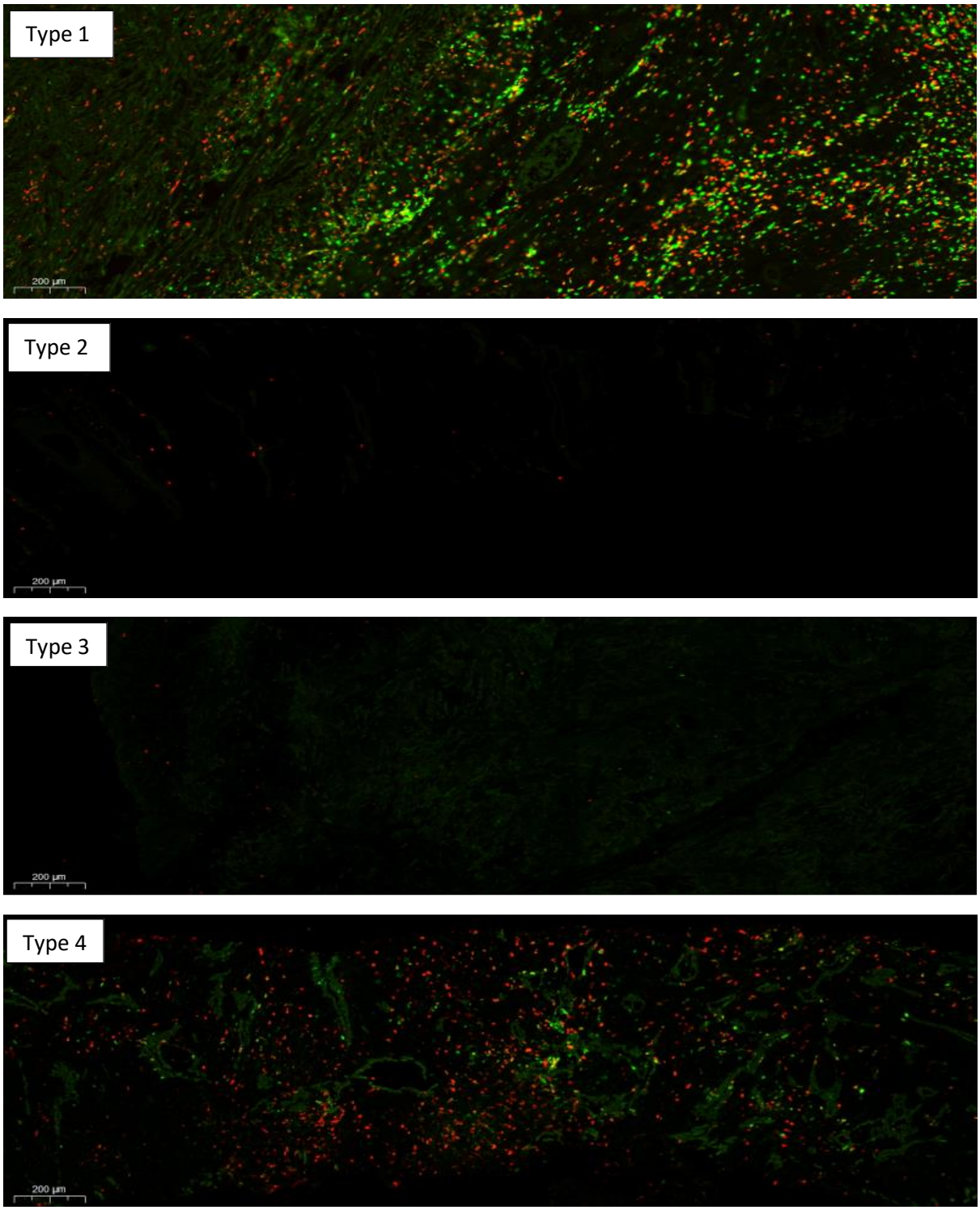

Figure 73. Overlay of CD8 & PD-1 fluorophore channel, displaying lung tissue samples of four different tumour types from DREAM study participants. Type 1 = PD-L1^{+}CD8^{+}PD-1^{+}High, Type 2 = PD-L1^{-}CD8^{+}PD-1^{+}Low, Type 3 = PD-L1^{+}CD8^{+}PD-1^{+}Low & Type 4 = PD-L1^{-}CD8^{+}PD-1^{+}High. CD8 & PD-1.

5 DISCUSSION

5.1 AUTOMATED IMAGE ANALYSIS: STANDARDIZING & STREAMLINING

Digital pathology software has a workflow similar to flow cytometry and offers a high level of precision, to the quantification of tissue architecture that has yet to be fully realized. Automation can provide, standardization and reproducibility by eliminating interobserver variability, and improved accuracy by eliminating human error. IHC chromogen stained slides from the DREAM study were manually scored for PD-L1 using the CPS, the results were correlated to the % of PD-L1 expressed on paired digitally analyzed multiplex immunofluorescent slides (figure 60). The goodness of fit variation returned an R squared value of 0.6631. The variation could be attributed to higher automated detection of PD-L1, or differing assays. The more likely scenario to explain the degree of variation is that the comparable tissue scored, while being representative was not an exact match between samples. A recent study comparing manual and automated image analysis by Widmaier *et al*. compared exactly aligned tissue samples of 47 archived NSCLC patients(128). PD-L1 expression was quantified using 4 commercially available IHC assays and a high rate of concordance was found between manual pathologist reference scores and automated expression(128). The high level of precision was recorded with a F1 score of 0.8 to 0.9 across a range of PD-L1 cut-off values(128).

Importantly, this study shows automated analysis offers improved sensitivity to detect low abundance PD-L1 expression. In the DREAM study, manual scoring using a 5% cut-off value, classified 5 (10.4%) of participants as negative, whom when scored digitally, were classified PD-L1 positive. A study of 93 MPM patients (48 from Switzerland and 45 from Australia) found PD-L1 expression was present in 71% of patients. PD-L1 expression was grouped based on staining with negative being <5%, intermediate being 5 - 49% and high being ≥ 50% staining of cell membrane(129). It found that 68% of patients were negative, 18% intermediate and in the 14% in the high group. A cut off value set at 5% would exclude 68% of patients from treatment even though they would have benefited from immune checkpoint blockade. As PD-L1 scoring may guide the selection of treatment options, being classified as either PD-L1 positive or negative from the patient's perspective is important.

5.2 NON-IMMUNOGENIC TUMOURS CULTIVATE A "COLD" TME

It is reported that immune excluded tumours are characterized by a high volume of well-organized peritumoural stroma that creates a physical barrier, blocking entry of cytotoxic T cells into tumour parenchyma(68) Tumour cells can also suppress the appropriate chemokines required to traffic cytotoxic T cells to the tumour site(71). TAMs have been shown in murine and human models to promote immune system "escape" by tumour cells. Peranzoni *et al*. using a mouse tumour model showed in lung squamous carcinoma, macrophages trapping CD8 T cells in stroma tissue for long time periods, prevented CD8 T cells reaching tumour cells(130). This could be one explanation as to why CD8 and $CD8^{+}PD\text{-}1^{+}$ T cell density is higher on stromal cells compared to tumour epithelium (figures 64 & 65). Interestingly CD8 is correlated with tumour epithelium for the SD group, R squared 0.6683, but not for the PR group, R squared 0.00124 (figure 70), pointing at other mechanisms working counter to adaptive immune resistance. Alternatively, the high R squared value of 0.6683 (figure 70) could be due to outliers present in data.

MPM tumours are notoriously non-immunogenic and suggested to be dominated by a "cold" phenotype. It is not surprising, given these are pre-treatment samples taken from a chemotherapy naïve population, that there would be a lower density of CD8 and $CD8^{+}PD\text{-}1^{+}$ T cells on the tumour epithelium compared to stromal tissue. It could even be suggested the higher density of $CD8^{+}PD\text{-}1^{+}PD\text{-}L1^{+}$ cells on stromal cells vs tumour cells (figure 66) is the result of a tumour induced feedback mechanism to aid induction of T cell anergy. The interplay between CD8, PD-1 & PD-L1 characterizes different immune responses present in the pre-treatment TME. PD-L1 expression is regulated differently, gaining knowledge about PD-L1/CD8 T cell interaction gives an indication of potential mechanisms deployed by the cancer to escape immunosurveillance.

PD-L1 upregulation can be a reactive response to activated CD8 cells that express PD-1, or a non-reactive upregulation driven by cancer cell intrinsic mechanisms. Potential host immune mechanisms can be derived by measuring pre-treatment PD-L1 not in isolation but in relation to CD8 cells and $CD8^{+}PD\text{-}1^{+}$ cells on either tumour epithelium or stromal cells. This is evident by the fact that PD-1 and PD-L1 expression is not significant in either tumour or stromal cells (figures 61, 62 & 63), however once combined with CD8 these markers are significant (figures 65 & 66). Immune cells measured in combination with PD-L1 also provides a likelihood of treatment outcomes as tumour responses are

governed not by antibodies per say but effector CD8 T cells. The next logical step is to examine if cellular expression on either tumour epithelium, stromal cells or combined tissue is significantly different across PD, SD and PR groups. This could be indicative of patterns of immune interplay responsible for determining an individual's response to treatment.

5.3 PD-L1 EXPRESSION ON TUMOUR EPITHELIUM IS PREDICTIVE FOR PR OVER SD

Statistically higher tumour PD-L1 density for the PR vs SD group (figure 67) is relevant as the higher density could be indicative of stronger "adaptive immune resistance" response occurring the PR group. Previous lung cancer studies have shown in combination therapies PD-L1 is no longer predictive, the exact reason why PD-L1 is not predictive for combination therapy is unknown(131). It has been reported that chemotherapy can induce PD-L1 expression, making pre-treatment PD-L1 status a redundant measurement(131). The keynote 021 study measured ORR of chemotherapy plus pembrolizumab vs chemotherapy alone in NSCLC(131). The study reported 57% of participants in the combination arm, with a TPS < 1% of PD-L1 had an ORR of 57%, compared to the ORR of 55% for all participants in the combination arm(131). In this instance the comparison being tested is, did a patient respond or not respond to treatment, and was PD-L1 significant for that response. In the context of mesothelioma, SD could still be thought of as a positive, albeit weaker clinical outcome compared to PR, what is being tested is a weak versus strong response. The predictive power is not associated with non-responder's vs responders, it is associated with predicting patients that can be tipped from a pre-transitioned disease state (SD) to a new disease state (PR).

In monotherapeutic anti PD-1/L1 treatments, higher PD-L1 expression is generally associated improved clinical outcomes. The JAVELIN trial reported higher ORR (19% vs 7%) and PFS (5.3 vs 1.7 months) for PD-L1^{+} tumours (PD-L1 ≥ 5% tumour epithelium) vs PD-L1^{-} tumours in response to avelumab in MPM(15). The Chicago phase II trial of pembrolizumab in patients with previously treated mesothelioma reported that there was a trend towards higher response rates in PD-L1^{+} (≥ 1% TPS) vs PD-L1^{-} tumours (28% vs 7%)(53). The response rate for PD-L1 expression < 1% was 7%, for PD-L1 expression 1 – 49% response was 26% and for PD-L1 expression ≥ 50% response was 31%(53). In the DREAM cohort the trend towards ≥ 5% PD-L1 expression was greatest for the PR group over the SD group (64% vs 23%) (figure 68).

5.4 CORRELATION OF PD-L1$^+$ WITH CD8$^+$ & CD8$^+$PD-1$^+$ DENSITY.

The strongest correlation between PD-L1 and activated CD8$^+$PD-1$^+$ T cells occurs for the PR group, R squared 0.4002, the SD group has a slightly lower correlation of 0.2985 (figure 69). It is possible this correlation could be due to outliers; however, the stronger correlation may be due to a stronger adaptive immune resistance in PR participants, responsible for tipping a patient from the pre-transitioned phase into the new state phase (PR). The SD group while not achieving a reduction in tumour size, have still managed to avoid PD over the duration of the trial, possibly due to a weaker adaptive immune resistance. In the SD group CD8 vs PD-L1 is also highly correlated on stromal cells with an R squared value of 0.6557 (appendix 9.d), it is possible the strength of immunosuppressive PD-L1 expressed in the stroma is preventing this group being tipped from the pre-transitioned state into a new state.

Studies have shown CD8$^+$PD-1$^+$ expression to be a double-edged sword in predicting clinical outcomes, high levels indicate poor outcomes in liver, pancreatic and head and neck cancers(40). In contrast elevated CD8$^+$PD-1$^+$ expression is associated with improved treatment outcomes in lung cancer, following anti PD-1 treatment(132). Mazzaschi *et al*. reported in a study of NSCLC patients treated with nivolumab, that patients with low PD-1 expression among CD8 T cells were associated with PFS(114). Kamphorts *et al.* reported in lung cancer patients being treated with anti PD-1, that 70% of patients that experienced PD had absent or delayed CD8$^+$PD-1$^+$ T cell response(132). This underlines the importance of CD8$^+$PD-1$^+$ T cells to promote immune responses through feedback mechanisms, patients may not respond to treatment if they express additional dominant or concurrent immune checkpoints. PD-L1 antibodies block PD-1 and CD80 binding PD-L1 but not PD-L2 which is expressed on APCs in lymph nodes, maintaining the PD-1/PD-L2 pathway would preserve lymphoid organ immune tolerance(133). It has also been reported that some tumours express PD-L2, potentially also maintaining a degree of peripheral immune tolerance(133).

5.5 TUMOUR TYPE PD-L1$^+$HIGHCD8$^+$PD-1$^+$ SIGNATURE IS ASSOCIATED WITH PR

The signature PD-L1$^+$HighCD8$^+$PD-1$^+$ is characteristic of a type 1 tumour (figures 71 - 73) and was associated with PR for DREAM study participants (table 11). This is consistent with findings in other immunologically “hot” tumour types, including NSCLC and metastatic melanoma in which the data is

most mature. It is likely that in response to chemoimmunotherapy "cold" tumours such as mesothelioma become "hot" tumours. The change required to tip a patient from the pre-transition phase into a new state phase may be very small. Patients that have shown a certain level of adaptive immune resistance, may with the compounding effect of chemoimmunotherapy may be pushed over the tipping point and achieve PR. Taube *et al*. first reported a strong association with 98% of PD-L1^{+} tumours being associated with TILs, compared with 28% on PD-L1^{-} tumours in melanoma(34). Teng *et al*., reported that ~ 38% of patients with a PD-L1^{+}TIL^{+} tumour type in melanoma, responded to anti-PD-1 treatment(92). The combination of CD8 and PD-L1 to predict response to anti PD-1 therapy in NSCLC was highly significant as reported by fumet *et al*. in response to RNA sequencing and IHC techniques(134).

5.6 CD8 DENSITY AT INVASIVE TUMOUR MARGIN

A study published by Jiang *et al*., stratified Chinese lung squamous cell carcinoma into 4 tumour types based on PD-L1+/- and high/low CD8 TIL density, and found no correlation to clinical outcomes in response to immunotherapy(135). CD8 density specifically at the tumour invasive margin was not able to able to be measured in the DREAM study, nor was it measured by Jiang *et. al.* this could explain the lack of significant findings. A study by Tumeh *et al*. showed metastatic tumour regression in melanoma following anti-PD-1 treatment, occurred in pre-treatment samples containing a high density of CD8 T cells in close proximity to tumour epithelium(60). This is similar to what is seen in DREAM study participants with a type 1 tumour (figures 71 – 73).

Numerous studies have reported measuring CD8 cell density at the invasive tumour margin can be predictive for treatment outcomes, as opposed to general CD8 T cell density across entire tissue sections(60)(113)(136). A limitation of this study is that it was not possible to distinguish the invasive tumour margin due to insufficient material in the biopsy samples. This resulted in CD8 T cell density being measured across entire mask areas, it is possible that if CD8 T cell density was determined within the smaller area of the invasive tumour margin, associated clinical outcomes may have been significant. As the density of CD8^{+}PD-1^{+} cells on tumour epithelium is comparatively small, it would have been beneficial to have measured CD8^{+}PD-1^{+} at the invasive tumour margin. If adaptive immune resistance is the prevalent mechanism that tips patients into the PR group in response to chemoimmunotherapy, then it would be logical to assume a higher density of CD8^{+}PD-1^{+} cells at the

invasive tumour margin. This measurement could have improved association and stratification of patients into respective tumour types based on PD-L1 and $CD8^+$ $PD\text{-}1^+$ cells.

5.7 Future Research

In order to test the hypothesis, that pre-treatment adaptive immune resistance is predictive for achieving PR to chemoimmunotherapy in MPM, it would be necessary to test IFN-γ levels in proximity to $CD8^+PD\text{-}1^+$ and tumour PD-L1. Commercially available IFN-γ can be applied to IHC assays and used alongside CD8, PD1, PD-L1 and cytokeratin. Digital image analysis software can, slide quality permitting, quantify density and measure distance between markers. If adaptive immune resistance is the mechanism causing PR, then the question becomes, what can be done to either generate adaptive immune resistance or overcome the lack of adaptive immune resistance in the SD group? The correlation and relationship of PD-L1 to PD-1 (in the absence of CD8 could be explored) in the TME, an area that was not explored in this thesis due to time restraints.

The data set used in this thesis was restricted to measure only three primary clinicopathological variables from the DREAM study including PD, SD and PR. An approach well suited to the research aims of this thesis to assess pre-treatment immune contexture between SD and PR groups, and to identify potential mechanisms that explain clinical outcomes and identify predictive biomarkers. Also, the variables available to measure was limited due to confidentiality surrounding unpublished data. Following this initial analysis, it would be beneficial to add additional secondary variables to further enhance statistical analysis including toxicity rates and OS. A limitation to this approach is that other potential cofounding variables, i.e. age were omitted from analysis.

5.8 Limitations

Indeterminable invasive tumour margins – as previously mentioned.

Heterogeneity – as previously mentioned.

Immunosuppressant molecules excluding the PD-1/PD-L1 axis – as previously mentioned.

Limited antibody binding sites – detecting PD-L1 expression in FFPE tissue is difficult as the PD-L1 protein contains only two small hydrophobic regions which limits the number of available antigen binding sites(28).

Variation in fixation – the denaturant effect of formalin fixation can compromise antigen staining during IHC. Tissue samples were collected from 10 different sites, and as such different samples would have been placed in fixative of varying times and differing ratios could modulate PD-L1, PD-1 and CD8 staining.

Autofluorescence – biological autofluorescence occurs in human cells due to flavin co-enzymes FAD & FMH (absorption 450nm/emission 575 nm) and reduced pyridine nucleotide (absorption 340nm/emission 460nm)(137).

Statistics –the study is concerned with correlations between variables, however it is possible that some of the associations are not causative but occur purely by chance.

Technical controls –the first filter cube is exposed to a higher quantity of photons, the positions of the FITC and DAPI filter cubes, were switched after scanning batch 1, to reduce the intensity of the FITC signal and enhance DAPI expression. There was also variation in exposure times for some filters between batches i.e. Cy5 (PD-L1) filter has an exposure time 22 seconds in batch 1 and 7 seconds for batches 2, 3 and 4. Ideally technical controls should be constant across all batches, however this is not always possible, as setting are kept constant for all slides within each batch the technical controls are still valid.

6 ACKNOWLEDGEMENTS:

I would like to acknowledge and thank the whole NCARD team and the University of Western Australia, for the opportunity to carry out this research. Particularly Anna Nowak who oversaw the DREAM study, and my primary supervisor Alistair Cook for his guidance. I would also like to thank:

Andrew Currie – Murdoch University Co-supervisor

Tracey Lee-Pullen – St John of God, Cancer Research Group

Chidozie Anyaegbu – St John of God, Cancer Research Group

Timothy Miller – St John of God, Cancer Research Group

Connull Leslie – PathWest

Tamara Abel – Telephon Kids Institute

To the participants of the DREAM study, for their consent and provision of invaluable samples.

Finally, to my wonderful family for all their love and support.

To the memory of my late father, a very special person who taught me many things.

Importantly I thank God for the many blessings and strength to carry out this project.

7 APPENDIX

Appendix 1.

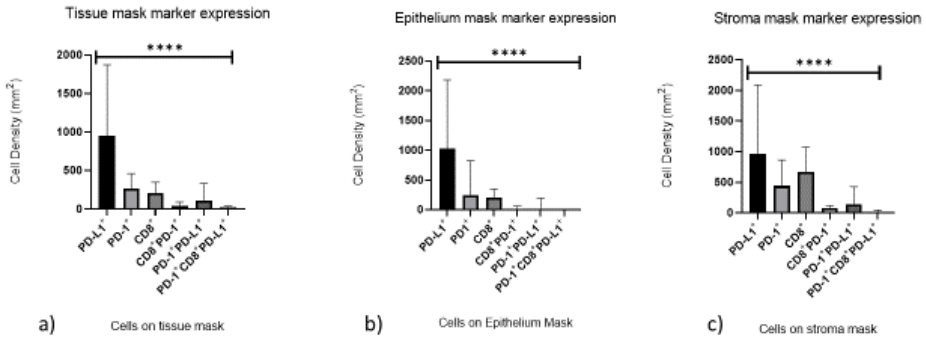

Median cell density: PDL1: 946 mm2, PD-1: 2665 mm2, CD8: 209.5 mm2, CD8PD-1: 44.5 mm2, PD-1PD-L1: 106 mm2 and PD-1CD8PD-L1: 15 mm2. Kruskal-Wallis Test p value < 0.0001.

Median cell density: PDL1: 1031.5 mm2, PD-1: 249.5 mm2, CD8: 212 mm2, CD8PD-1: 21 mm2, PD-1PD-L1: 21 mm2 and PD-1CD8PD-L1: 3 mm2. Kruskal-Wallis Test p value < 0.0001.

Median cell density: PDL1: 969.5 mm2, PD-1: 440 mm2, CD8: 664 mm2, CD8PD-1: 72 mm2, PD-1PD-L1: 142 mm2 and PD-1CD8PD-L1: 18.5 mm2. Kruskal-Wallis Test p value < 0.0001.

Appendix 2.

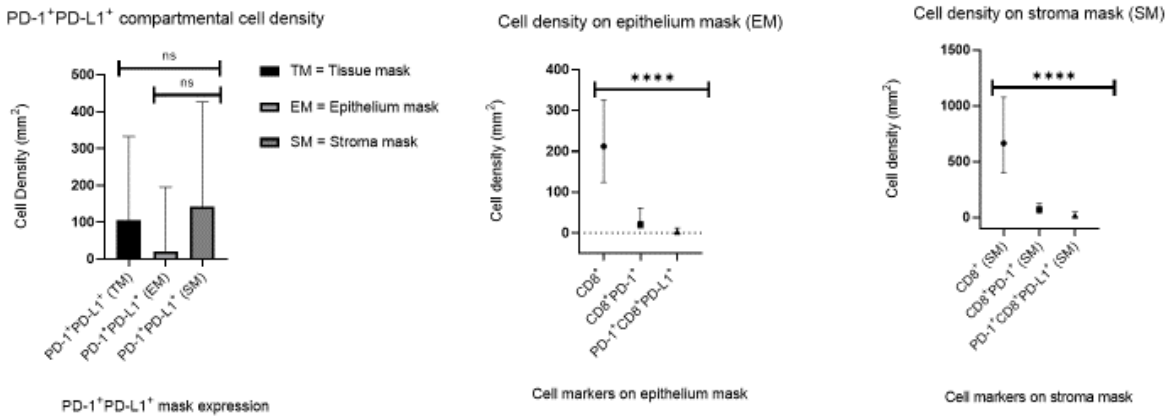

a) Mann U Whitney test between EM & SM PD-L1, p value 0.0594. Kruskal-Wallis test between TM, EM & SM, value 0.1564

b) Kruska-Wallis test between CD8, CD8PD-1 and PD-1CD8PD-L1, p value <0.0001.

c) Kruska-Wallis test between CD8, CD8PD-1 and PD-1CD8PD-L1, p value <0.0001.

Appendix 3.

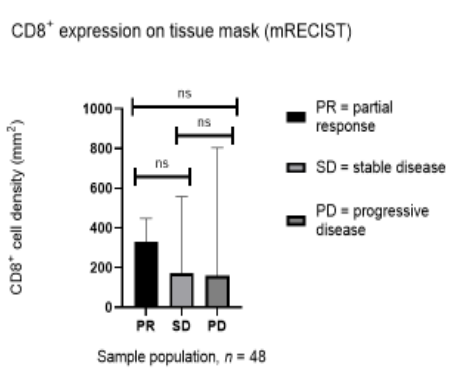

a) Mann U Whitney test: PR vs SD, p value 0.2766; PD vs. PR, p value 0.2962; PD vs SD, p value 0.9186. Kruskal-Wallis test: PR, SD & PD, p value, 0.4018.

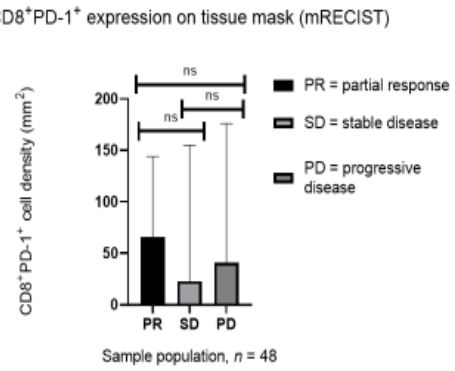

b) Mann U Whitney test: PR vs SD, p value 0.5294; PD vs. PR, p value 0.6725; PD vs SD, p value 0.9615. Kruskal-Wallis test: PR, SD & PD p value, 0.7808.

Appendix 4.

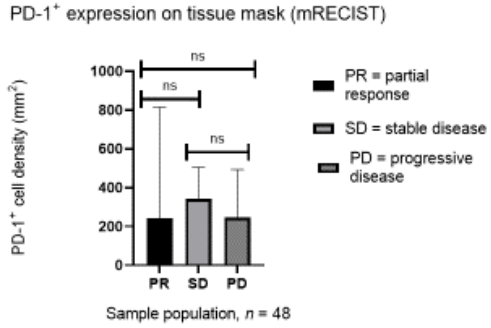

a) Mann U Whitney test: PR vs SD, p value 0.8841; PD vs. PR, p value 0.6695; PD vs SD, p value 0.5617. Kruskal-Wallis test: PR, SD & PD, p value, 0.8504.

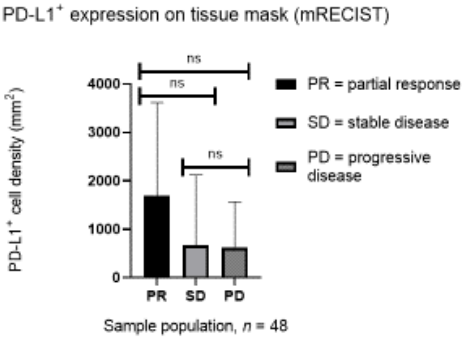

b) Mann U Whitney test: PR vs SD, p value 0.2627; PD vs. PR, p value 0.2271; PD vs SD, p value 0.88115 Kruskal-Wallis test: PR, SD & PD, p value, 0.3340.

Appendix 5.

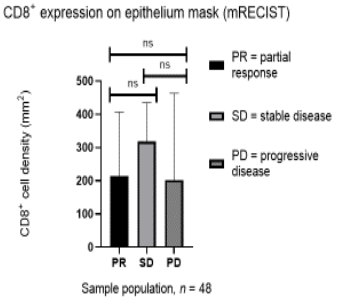

a) Mann U Whitney test: PR vs SD, p value 0.9042; PD vs. PR, p value 0.8202; PD vs SD, p value 0.8648. Kruskal-Wallis test: PR, SD & PD, p value, 0.9627.

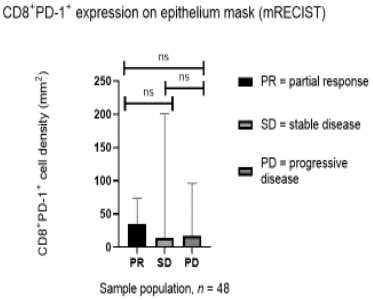

b) Mann U Whitney test: PR vs SD, p value 0.5461; PD vs. PR, p value 0.3703; PD vs SD, p value 0.8643. Kruskal-Wallis test: PR, SD & PD, p value, 0.6725.

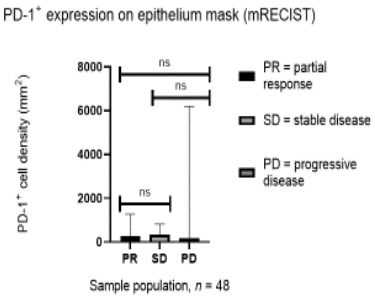

c) Mann U Whitney test: PR vs SD, p value 0.7370; PD vs. PR, p value 0.> 0.9999; PD vs SD, p value 0.9186. Kruskal-Wallis test: PR, SD & PD, p value, 0.9186.

Appendix 6.

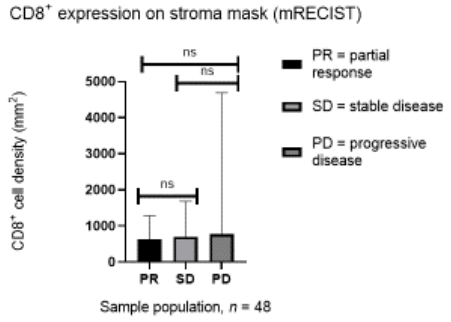

a) Mann U Whitney test: PR vs SD, p value 0.8642; PD vs. PR, p value 0.9418; PD vs SD, p value 0.9186. Kruskal-Wallis test: PR, SD & PD, p value, 0.9787.

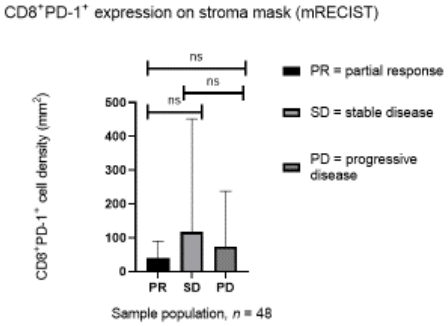

b) Mann U Whitney test: PR vs SD, p value 0.0653; PD vs. PR, p value 0.7613; PD vs SD, p value 0.3187. Kruskal-Wallis test: PR, SD & PD, p value, 0.1655.

Appendix 7.

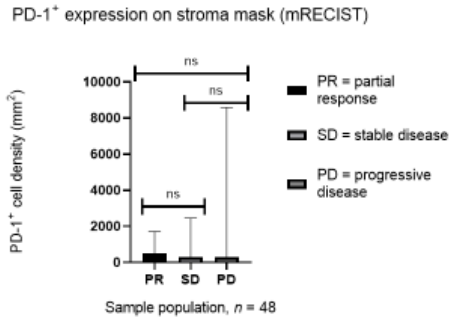

a) Mann U Whitney test: PR vs SD, p value 0.5943; PD vs. PR, p value >0.9999; PD vs SD, p value 0.9729. Kruskal-Wallis test: PR, SD & PD, p value, 0.8838.

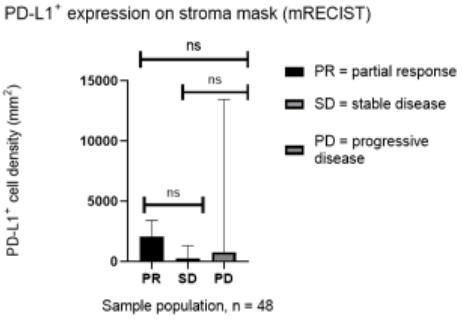

b) Mann U Whitney test: PR vs SD, p value 0.0910; PD vs. PR, p value 5095; PD vs SD, p value 0.3917. Kruskal-Wallis test: PR, SD & PD, p value, 0.1999.

Appendix 8.

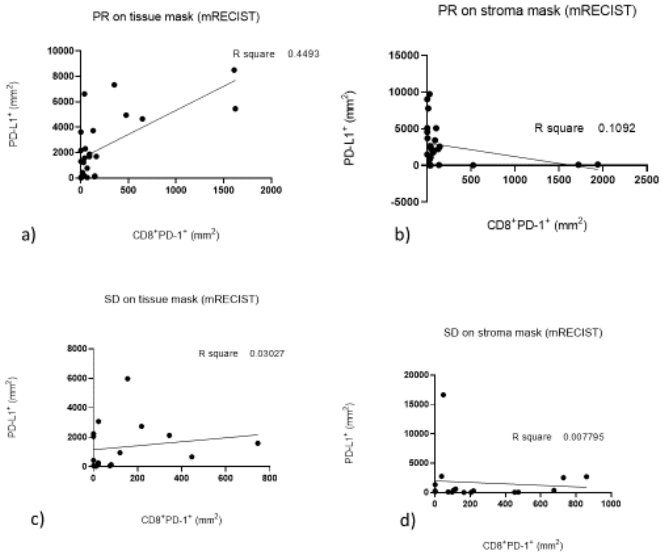

Appendix 9.

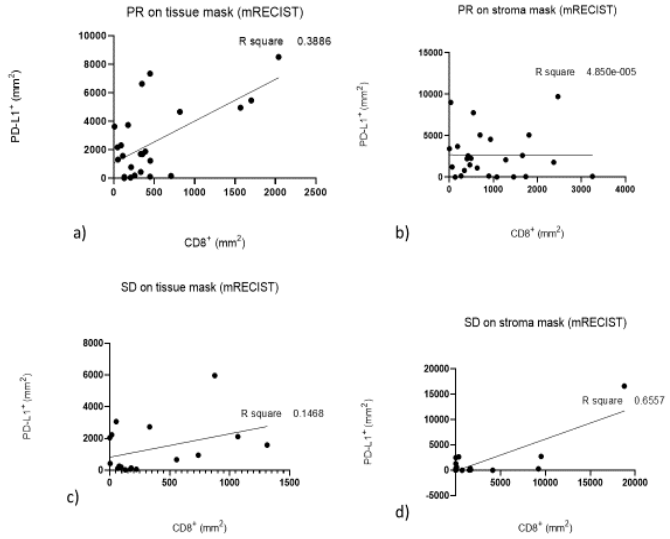

Appendix 10.

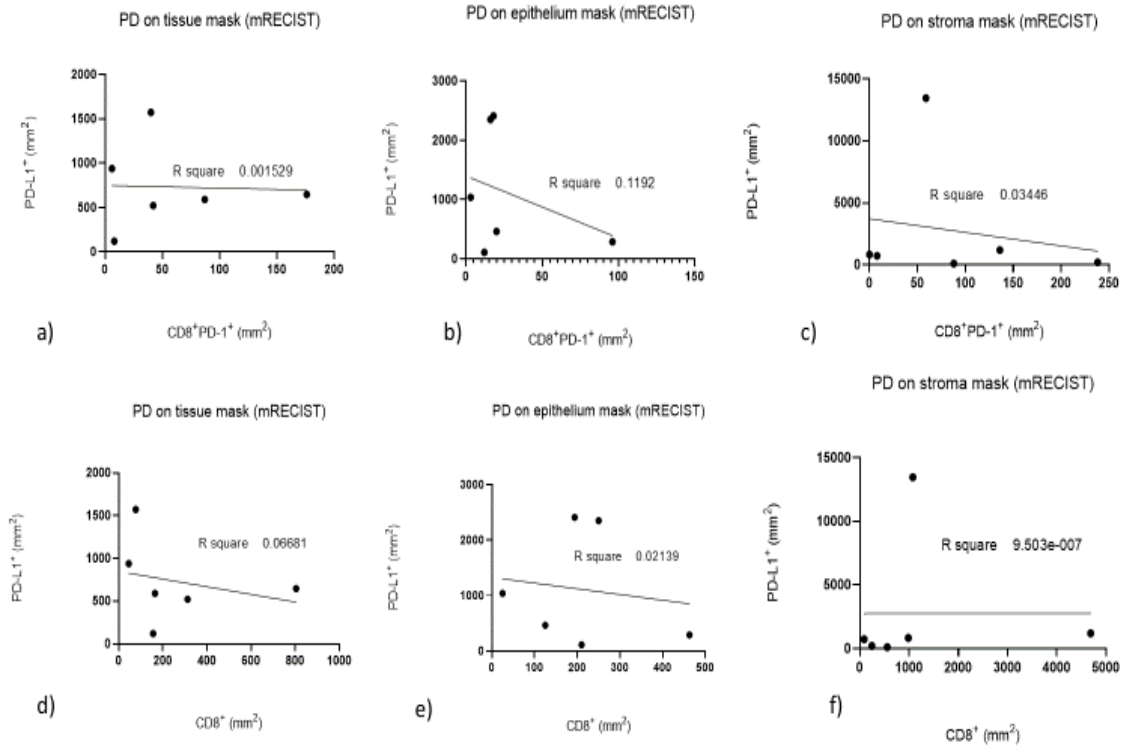

REFERENCES:

1. McCambridge AJ, Napolitano A, Mansfield AS, Fennell DA, Sekido Y, Nowak AK, et al. Progress in the Management of Malignant Pleural Mesothelioma in 2017. J Thorac Oncol. 2018;13(5):606–23.

2. Bibby AC, Tsim S, Kanellakis N, Ball H, Talbot DC, Blyth KG, et al. Malignant pleural mesothelioma: An update on investigation, diagnosis and treatment. Eur Respir Rev [Internet]. 2016;25(142):472–86. Available from: http://dx.doi.org/10.1183/16000617.0063-2016

3. Rossini M, Rizzo P, Bononi I, Clementz A, Ferrari R, Martini F, et al. New Perspectives on Diagnosis and Therapy of Malignant Pleural Mesothelioma [Internet]. Vol. 8, Frontiers in Oncology . 2018. p. 91. Available from: https://www.frontiersin.org/article/10.3389/fonc.2018.00091

4. Robinson BM. Malignant pleural mesothelioma: an epidemiological perspective. Ann Cardiothorac Surg [Internet]. 2012;1(4):491–6. Available from: http://www.pubmedcentral.nih.gov/articlerender.fcgi?artid=3741803&tool=pmcentrez&rendertype=abstract

5. Frank AL, Joshi TK. The global spread of asbestos. Ann Glob Heal. 2014;80(4):257–62.

6. Pasello G, Zago G, Lunardi F, Urso L, Kern I, Vlacic G, et al. Malignant pleural mesothelioma immune microenvironment and checkpoint expression: Correlation with clinical-pathological features and intratumor heterogeneity over time. Ann Oncol. 2018;29(5):1258–65.

7. McCoy MJ, Nowak AK, Lake RA. Chemoimmunotherapy: An emerging strategy for the treatment of malignant mesothelioma. Tissue Antigens. 2009;74(1):1–10.

8. Ying S, Jiang Z, He X, Yu M, Chen R, Chen J, et al. Serum HMGB1 as a Potential Biomarker for Patients with Asbestos-Related Diseases. Dis Markers. 2017;2017:1–9.

9. Bianchi C, Bianchi T. Global mesothelioma epidemic: Trend and features. Indian J Occup Environ Med. 2014;18(2):82.

10. Soeberg M, Vallance DA, Keena V, Takahashi K, Leigh J. Australia's ongoing legacy of asbestos: Significant challenges remain even after the complete banning of asbestos almost fifteen years ago. Int J Environ Res Public Health. 2018;15(2):1–14.

11. Lancet T, Medicine R. Editorial Pleural mesothelioma : tackling a deadly cancer. Lancet Respir [Internet]. 2018;7(2):99. Available from:

http://dx.doi.org/10.1016/S2213-2600(19)30004-9

12. R.K. G. Review of pemetrexed in combination with cisplatin for the treatment of malignant pleural mesothelioma. Ther Clin Risk Manag [Internet]. 2008;4(1):205–11. Available from: http://www.embase.com/search/results?subaction=viewrecord&from=export&id=L351460944

13. Husain AN, Colby T V, Ordóñez NG, Krausz T, Borczuk A, Cagle PT, et al. Guidelines for Pathologic Diagnosis of Malignant Mesothelioma: A Consensus Statement from the International Mesothelioma Interest Group. Arch Pathol Lab Med [Internet]. 2009 Aug 1;133(8):1317–31. Available from: https://www.archivesofpathology.org/doi/abs/10.1043/1543-2165-133.8.1317

14. Minnema-Luiting J, Vroman H, Aerts J, Cornelissen R. Heterogeneity in immune cell content in malignant pleural mesothelioma. Int J Mol Sci. 2018;19(4).

15. Hassan R, Thomas A, Nemunaitis JJ, Patel MR, Bennouna J, Chen FL, et al. Efficacy and Safety of Avelumab Treatment in Patients with Advanced Unresectable Mesothelioma: Phase 1b Results from the JAVELIN Solid Tumor Trial. JAMA Oncol. 2019;5(3):351–7.

16. Inai K. Pathology of mesothelioma. Environ Health Prev Med. 2008;13(2):60–4.

17. Hjerpe A, Abd-Own S, Dobra K. Cytopathologic diagnosis of epithelioid and mixed-type malignant mesothelioma: Ten years of clinical experience in relation to international guidelines. Arch Pathol Lab Med. 2018;142(8):893–901.

18. John T, Russell PA, Thapa B, S MBB. Is Mesothelioma in China Rare or Misdiagnosed ? J Thorac Oncol [Internet]. 2017;12(4):607–9. Available from: http://dx.doi.org/10.1016/j.jtho.2017.02.004

19. Watanabe T, Okuda K, Moriyama S, Haneda H, Yokota K, Tatematsu T, et al. P2.06-37 Four Immunohistochemical Assays to Measure the PD-L1 Expression in Malignant Pleural Mesothelioma. J Thorac Oncol. 2018;13(10):S757.

20. Ricciardi S, Cardillo G, Zirafa CC, Carleo F, Facciolo F, Fontanini G, et al. Surgery for malignant pleural mesothelioma : an international guidelines review. 2018;10(4):285–92.

21. Vogelzang NJ, Rusthoven JJ, Symanowski J, Denham C, Kaukel E, Ruffie P, et al. Phase III study of pemetrexed in combination with cisplatin versus cisplatin alone in patients with malignant pleural

mesothelioma. J Clin Oncol. 2003;21(14):2636–44.

22. Rimner A, Zauderer MG, Gomez DR, Adusumilli PS, Parhar PK, Wu AJ, et al. Phase II study of hemithoracic intensity-modulated pleural radiation therapy (IMPRINT) as part of lung-sparing multimodality therapy in patients with malignant pleural mesothelioma. J Clin Oncol. 2016;34(23):2761–8.

23. Eberst G, Anota A, SCHERPEREEL A, Mazieres J, Margery J, Greillier L, et al. Health-related Quality of Life Impact from Adding Bevacizumab to Cisplatin-Pemetrexed in Malignant Pleural Mesothelioma in the MAPS IFCT-GFPC-0701 Phase III Trial. Clin Cancer Res [Internet]. 2019;clincanres.2860.2018. Available from: http://clincancerres.aacrjournals.org/lookup/doi/10.1158/1078-0432.CCR-18-2860

24. Zitvogel L, Kroemer G. Targeting PD-1/PD-L1 interactions for cancer immunotherapy. Oncoimmunology. 2012;1(8):1223–5.

25. Aston WJ, Fisher SA, Khong A, Mok C, Nowak AK, Lake RA, et al. Combining chemotherapy and checkpoint blockade in thoracic cancer: how to proceed? Lung Cancer Manag. 2014;3(6):443–57.

26. Freeman GJ, Wherry EJ, Ahmed R, Sharpe AH. Reinvigorating exhausted HIV-specific T cells via PD-1–PD-1 ligand blockade. J Exp Med. 2006;203(10):2223–7.

27. Reiser J, Banerjee A. Effector, Memory, and Dysfunctional CD8 + T Cell Fates in the Antitumor Immune Response . J Immunol Res. 2016;2016:1–14.

28. Sznol, M. Chen L. Antagonist antibodies to PD-1 and B7-H1 (PD-L1) in the treatment of advanced human cancer. Clin Cancer Res. 2013;19(5):1021–34.

29. Nelson D, Fisher S, Robinson B. The “Trojan Horse” Approach to Tumor Immunotherapy: Targeting the Tumor Microenvironment. J Immunol Res. 2014;2014:1–14.

30. Romano E, Romero P. The therapeutic promise of disrupting the PD-1/PD-L1 immune checkpoint in cancer: Unleashing the CD8 T cell mediated anti-tumor activity results in significant, unprecedented clinical efficacy in various solid tumors. J Immunother Cancer. 2015;3(1):1–5.

31. Zerdes I, Matikas A, Bergh J, Rassidakis GZ, Foukakis T. Genetic, transcriptional and post-translational regulation of the programmed death protein ligand 1 in cancer: biology and clinical correlations. Oncogene [Internet]. 2018;37(34):4639–61. Available from: http://dx.doi.org/10.1038/s41388-018-0303-3

32. Constantinidou A, Alifieris C, Trafalis DT. Targeting Programmed Cell Death -1 (PD-1) and Ligand (PD-L1): A new era in cancer active immunotherapy. Pharmacol Ther. 2019;194:84–106.

33. Pfirschke C, Engblom C, Rickelt S, Cortez-retamozo V, Garris C, Pucci F, et al. Blockade Therapy. 2017;44(2):343–54.

34. Taube JM, Klein A, Brahmer JR, Xu H, Pan X, Kim JH, et al. Association of PD-1, PD-1 ligands, and other features of the tumor immune microenvironment with response to anti-PD-1 therapy. Clin Cancer Res. 2014;20(19):5064–74.

35. Kumar S, Sharawat SK. Epigenetic regulators of programmed death-ligand 1 expression in human cancers. Transl Res [Internet]. 2018;202(401):129–45. Available from: https://doi.org/10.1016/j.trsl.2018.05.011

36. Parra ER, Behrens C, Rodriguez-Canales J, Lin H, Mino B, Blando J, et al. Image analysis-based assessment of PD-L1 and tumor-associated immune cells density supports distinct intratumoral microenvironment groups in non-small cell lung carcinoma patients. Clin Cancer Res. 2016;22(24):6278–89.

37. De Lara PT, Cecconi V, Hiltbrunner S, Yagita H, Friess M, Bode B, et al. Gemcitabine synergizes with immune checkpoint inhibitors and overcomes resistance in a preclinical model and mesothelioma patients. Clin Cancer Res. 2018;24(24):6345–54.

38. Schildberg FA, Klein SR, Freeman GJ, Sharpe AH. Coinhibitory Pathways in the B7-CD28 Ligand-Receptor Family. Immunity. 2016;44(5):955–72.

39. Kinter AL, Godbout EJ, Mcnally JP, Sereti I, Roby GA, Shea MAO, et al. Audrey L. Kinter, 1 Emily J. Godbout, Jonathan P. McNally, Irini Sereti, Gregg A. Roby, Marie A. O'Shea, and Anthony S. Fauci. J Immunol. 2008;1–9.

40. Yeong J, Chun J, Lim T, Lee B, Li H, Chong C, et al. Prognostic value of CD8 + PD-1 + immune infiltrates and PDCD1 gene expression in triple negative breast cancer. J Immunother Cancer. 2019;7:34.

41. Tsushima F, Yao S, Shin T, Flies A, Flies S, Xu H, et al. Interaction between B7-H1 and PD-1 determines initiation and reversal of T-cell anergy. Blood. 2007;110(1):180–5.

42. Kwon HJ, Yang JM, Lee JO, Lee JS, Paik JH. Clinicopathologic implication of PD-L1 and phosphorylated STAT3 expression in diffuse large B cell lymphoma. J Transl Med [Internet]. 2018;16(1). Available from: https://doi.org/10.1186/s12967-018-1689-y

43. E.R. P, C. B, J. R-C, H. L, B. M, J. B, et al. Image analysis-based assessment of PD-L1 and tumor-associated immune cells density supports distinct intratumoral microenvironment groups in non-small cell lung carcinoma patients. Clin Cancer Res [Internet]. 2016;22(24):6278–89. Available from: http://clincancerres.aacrjournals.org/content/22/24/6278.full-text.pdf%5Cnhttp://ovidsp.ovid.com/ovidweb.cgi?T=JS&PAGE=reference&D=emed18b&NEWS=N&AN=613783402

44. Maimela NR, Liu S, Zhang Y. Fates of CD8+ T cells in Tumor Microenvironment. Comput Struct Biotechnol J [Internet]. 2019;17:1–13. Available from: http://www.ncbi.nlm.nih.gov/pubmed/30581539%0Ahttp://www.pubmedcentral.nih.gov/articlerender.fcgi?artid=PMC6297055

45. Embgenbroich M, Burgdorf S. Current concepts of antigen cross-presentation. Front Immunol. 2018;9(JUL).

46. McDonnell AM, Nowak AK, Lake RA. Contribution of the immune system to the chemotherapeutic response. Semin Immunopathol. 2011;33(4):353–67.

47. Cook AM, Lesterhuis WJ, Nowak AK, Lake RA. Chemotherapy and immunotherapy: Mapping the road ahead. Curr Opin Immunol [Internet]. 2016;39:23–9. Available from: http://dx.doi.org/10.1016/j.coi.2015.12.003

48. Seliger, Barbara. Marincola, Francesco. Ferrone, Soldano. Abken H. The complex role of B& molecules in tumor immunolgy. Trends Mol Med. 2009;14(12):550–9.

49. Quispel-Janssen J, van der Noort V, de Vries JF, Zimmerman M, Lalezari F, Thunnissen E, et al. Programmed Death 1 Blockade With Nivolumab in Patients With Recurrent Malignant Pleural Mesothelioma. J Thorac Oncol [Internet]. 2018;13(10):1569–76. Available from: https://doi.org/10.1016/j.jtho.2018.05.038

50. Manuscript A, Onlinefirst P. Downloaded from clincancerres.aacrjournals.org on September 17, 2019. © 2019 American Association for Cancer Research. 2019;

51. Scherpereel A, Mazieres J, Greillier L, Lantuejoul S, Dô P, Bylicki O, et al. Nivolumab or nivolumab plus ipilimumab in patients with relapsed malignant pleural mesothelioma (IFCT-1501 MAPS2): 2019;20(February):239–53.

52. Alley EW, Lopez J, Santoro A, Morosky A, Saraf S, Piperdi B, et al. Clinical safety and activity of pembrolizumab in patients with malignant pleural mesothelioma (KEYNOTE-028): preliminary results from a non-randomised , open-label , phase 1b trial. Lancet Oncol [Internet].

18(5):623–30. Available from: http://dx.doi.org/10.1016/S1470-2045(17)30169-9

53. Desai A, Karrison T, Rose B, Tan Y, Hill B, Pemberton E. October 2018 Abstracts Phase II Trial of Pembrolizumab (NCT02399371) In Previously-Treated Malignant Mesothelioma (MM): Final Analysis Tumour Suppressor MicroRNAs Modulate Drug Resistance by Targeting Anti-Apoptotic Pathways in Malignant Pleural Mesot. J Thorac Oncol [Internet]. 2018;13(10):S339. Available from: https://doi.org/10.1016/j.jtho.2018.08.277

54. Disselhorst MJ, Quispel-Janssen J, Lalezari F, Monkhorst K, de Vries JF, van der Noort V, et al. Ipilimumab and nivolumab in the treatment of recurrent malignant pleural mesothelioma (INITIATE): results of a prospective, single-arm, phase 2 trial. Lancet Respir Med [Internet]. 2019 Mar 1 [cited 2019 Jun 18];7(3):260–70. Available from: http://www.ncbi.nlm.nih.gov/pubmed/30660511

55. Wang B, Gong C, Roskos L, Milberg O, Narwal R, Vicini P, et al. A computational multiscale agent-based model for simulating spatio-temporal tumour immune response to PD1 and PDL1 inhibition. J R Soc Interface. 2017;14(134):20170320.

56. Fear VS, Tilsed C, Chee J, Forbes CA, Casey T, Solin JN, et al. Combination immune checkpoint blockade as an effective therapy for mesothelioma. Oncoimmunology. 2018;7(10).

57. Wu L, de Perrot M. Radio-immunotherapy and chemo-immunotherapy as a novel treatment paradigm in malignant pleural mesothelioma. Transl Lung Cancer Res. 2017;6(3):325–34.

58. Guo G, Chmielecki J, Goparaju C, Heguy A, Dolgalev I, Carbone M, et al. Whole-exome sequencing reveals frequent genetic alterations in BAP1, NF2, CDKN2A, and CUL1 in malignant pleural mesothelioma. Cancer Res. 2015;75(2):264–9.

59. Alexandrov LB, Nik-Zainal S, Wedge DC, Aparicio SAJR, Behjati S, Biankin A V., et al. Signatures of mutational processes in human cancer. Nature. 2013;500(7463):415–21.

60. Tumeh PC, Harview CL, Yearley JH, Shintaku IP, Taylor EJM, Robert L, et al. PD-1 blockade induces responses by inhibiting adaptive immune resistance. Nature [Internet]. 2014;515(7528):568–71. Available from: http://www.ncbi.nlm.nih.gov/pubmed/25428505%0Ahttp://www.pubmedcentral.nih.gov/articlerender.fcgi?artid=PMC4246418

61. Saruwatari K, Sato R, Nakane S, Sakata S, Takamatsu K, Jodai T, et al. The Risks and Benefits of Immune Checkpoint Blockade in Anti-AChR Antibody-Seropositive Non-Small Cell Lung Cancer Patients. Cancers

(Basel). 2019;11(2):140.

62. Wong RM, Ianculescu I, Sharma S, Gage DL, Olevsky OM, Kotova S, et al. Immunotherapy for malignant pleural mesothelioma current status and future prospects. Am J Respir Cell Mol Biol. 2014;50(5):870–5.

63. Cornelissen R, Heuvers ME, Maat AP, Hendriks RW, Hoogsteden HC, Aerts JGJ V., et al. New Roads Open Up for Implementing Immunotherapy in Mesothelioma. Clin Dev Immunol. 2012;2012:1–13.

64. Thapa B, Watkins DN, John T. Immunotherapy for malignant mesothelioma: reality check. Expert Rev Anticancer Ther [Internet]. 2016;16(11):1167–76. Available from: http://dx.doi.org/10.1080/14737140.2016.1241149

65. Onishi Y, Fehervari Z, Yamaguchi T, Sakaguchi S. Foxp3+ natural regulatory T cells preferentially form aggregates on dendritic cells in vitro and actively inhibit their maturation. Proc Natl Acad Sci U S A. 2008;105(29):10113–8.

66. Nguyen BH, Montgomery R, Fadia M, Wang J, Ali S. PD-L1 expression associated with worse survival outcome in malignant pleural mesothelioma. Asia Pac J Clin Oncol. 2018;14(1):69–73.

67. Silva MA, Ryall KA, Wilm C, Caldara J, Grote HJ, Patterson-Kane JC. PD-L1 immunostaining scoring for non-small cell lung cancer based on immunosurveillance parameters. PLoS One. 2018;13(6):1–15.

68. Kowanetz M, Zou W, Gettinger SN, Koeppen H, Kockx M, Schmid P, et al. Differential regulation of PD-L1 expression by immune and tumor cells in NSCLC and the response to treatment with atezolizumab (anti–PD-L1). Proc Natl Acad Sci [Internet]. 2018;115(43):E10119–26. Available from: http://www.pnas.org/lookup/doi/10.1073/pnas.1802166115

69. Xu-Monette ZY, Zhang M, Li J, Young KH. PD-1/PD-L1 blockade: Have we found the key to unleash the antitumor immune response? Front Immunol. 2017;8(DEC).

70. Joost Lesterhuis W, Bosco A, Millward MJ, Small M, Nowak AK, Lake RA. Dynamic versus static biomarkers in cancer immune checkpoint blockade: Unravelling complexity. Nat Rev Drug Discov. 2017;16(4):264–72.

71. Gebremeskel S, Johnston B. Concepts and mechanisms underlying chemotherapy induced immunogenic cell death : impact on clinical studies and considerations for combined therapies. 2015;6(39).

72. Wang Y, Fletcher R, Yu J, Zhang L. ScienceDirect Immunogenic effects

of chemotherapy- induced tumor cell death. Genes Dis [Internet]. 2018;5(3):194–203. Available from: https://doi.org/10.1016/j.gendis.2018.05.003

73. Emens LA, Middleton G. The Interplay of Immunotherapy and Chemotherapy: Harnessing Potential Synergies. Cancer Immunol Res [Internet]. 2015;3(5):436–43. Available from: http://cancerimmunolres.aacrjournals.org/lookup/doi/10.1158/2326-6066.CIR-15-0064

74. Gotwals P, Cameron S, Cipolletta D, Cremasco V, Crystal A, Hewes B, et al. Prospects for combining targeted and conventional cancer therapy with immunotherapy. Nat Rev Cancer. 2017;17(5):286–301.

75. Krysko O, Aaes TL, Bachert C, Vandenabeele P, Krysko D V. Many faces of DAMPs in cancer therapy. 2013;1–7.

76. Wu J, Waxman DJ. Immunogenic chemotherapy: Dose and schedule dependence and combination with immunotherapy. Cancer Lett. 2019;210–21.

77. Luo Q, Zhang L, Luo C, Jiang M. Emerging strategies in cancer therapy combining chemotherapy with immunotherapy. Cancer Lett [Internet]. 2019;454(March):191–203. Available from: https://doi.org/10.1016/j.canlet.2019.04.017

78. Lin W, Chen M, Hong L, Zhao H, Chen Q. Crosstalk Between PD-1/PD-L1 Blockade and Its Combinatorial Therapies in Tumor Immune Microenvironment: A Focus on HNSCC. Front Oncol. 2018;8(November):1–16.

79. Iglesias VS, Giuranno L, Dubois LJ, Theys J, Vooijs M, Vooijs M. Drug Resistance in Non-Small Cell Lung Cancer : A Potential for NOTCH Targeting ? 2018;8(July).

80. Alizadeh D, Larmonier N. Chemotherapeutic targeting of cancer-induced immunosuppressive cells. Cancer Res. 2014;74(10):2663–8.

81. Rollins KD, Lindley C, Hill C, Carolina N. New Drug Pemetrexed : A Multitargeted Antifolate. 2005;

82. Chen J. Critical appraisal of pemetrexed in the treatment of NSCLC and metastatic pulmonary nodules. 2014;937–45.

83. Marcq E, Siozopoulou V, de Waele J, Van Audenaerde J, Zwaenepoel K, Santermans E, et al. Prognostic and predictive aspects of the tumor immune microenvironment and immune checkpoints in malignant pleural mesothelioma. Oncoimmunology. 2017;6(1):1–10.

84. Schaer D, Geeganage S, Amaladas N, Lu ZH, Rasmussen E, Sonyi A,

et al. P1.04-07 Pemetrexed Enhances Anti-Tumor Efficacy of PD-L1 blockade by Promoting Intra-Tumor Immune Response via Tumor and T Cell-Intrinsic Mechanisms. J Thorac Oncol. 2018;13(10):S527.

85. Bezu L, Gomes-da-Silva LC, Dewitte H, Breckpot K, Fucikova J, Spisek R, et al. Combinatorial strategies for the induction of immunogenic cell death. Front Immunol. 2015;6(APR):1–11.

86. Xu D, Liang S, Yang H, Lüthi U, Riether C, Berezowska S, et al. Increased sensitivity to apoptosis upon endoplasmic reticulum stress-induced activation of the unfolded protein response in chemotherapy-resistant malignant pleural mesothelioma. Br J Cancer [Internet]. 2018;(April). Available from: http://dx.doi.org/10.1038/s41416-018-0145-3

87. Nowak AK, Lesterhuis WJ, Hughes BGM, Brown C, Kok PS, O'Byrne KJ, et al. DREAM: A phase II study of durvalumab with first line chemotherapy in mesothelioma—First results. J Clin Oncol [Internet]. 2018 May 20;36(15_suppl):8503. Available from: https://doi.org/10.1200/JCO.2018.36.15_suppl.8503

88. Cedrés S, Ponce-Aix S, Zugazagoitia J, Sansano I, Enguita A, Navarro-Mendivil A, et al. Analysis of expression of programmed cell death 1 ligand 1 (PD-L1) in malignant pleural mesothelioma (MPM). PLoS One. 2015;10(3):1–12.

89. Duan J, Wang Y, Jiao S. Checkpoint blockade-based immunotherapy in the context of tumor microenvironment: Opportunities and challenges. Cancer Med. 2018;7(9):4517–29.

90. Hunter KA, Socinski MA, Villaruz LC. PD-L1 tesing in guiding patient selection for PD-1/PD-L1 inhibitor therapy in lung cancer. Mol Diagn Ther. 2019;22(1):1–10.

91. Langer CJ, Gadgeel SM, Borghaei H, Papadimitrakopoulou VA, Patnaik A, Powell SF, et al. Carboplatin and pemetrexed with or without pembrolizumab for advanced, non-squamous non-small-cell lung cancer: a randomised, phase 2 cohort of the open-label KEYNOTE-021 study. Lancet Oncol [Internet]. 2016;17(11):1497–508. Available from: http://dx.doi.org/10.1016/S1470-2045(16)30498-3

92. Teng MWL, Ngiow SF, Ribas A, Smyth MJ. Classifying cancers basedon T-cell infiltration and PD-L1. Cancer Res. 2015;75(11):2139–45.

93. Lievense LA, Sterman DH, Cornelissen R, Aerts JG. Checkpoint blockade in lung cancer and mesothelioma. Am J Respir Crit Care Med. 2017;196(3):274–82.

94. Igarashi T, Teramoto K, Ishida M, Hanaoka J, Daigo Y. Scoring of PD-L1

expression intensity on pulmonary adenocarcinomas and the correlations with clinicopathological factors. 2016;1–8.

95. Conroy JM, Pabla S, Nesline MK, Glenn ST, Papanicolau-sengos A, Burgher B, et al. Next generation sequencing of PD-L1 for predicting response to immune checkpoint inhibitors. 2019;5:1–11.

96. Velcheti V, Tumor S, Clinic C, Schalper KA, Haven N, Carvajal DE, et al. HHS Public Access. 2018;94(1):107–16.

97. Hirsch FR, Mcelhinny A, Stanforth D, Ranger-moore J, Jansson M, Kulangara K, et al. PD-L1 Immunohistochemistry Assays for Lung Cancer : Results from Phase 1 of the Blueprint PD-L1 IHC Assay Comparison Project. J Thorac Oncol [Internet]. 2017;12(2):208–22. Available from: http://dx.doi.org/10.1016/j.jtho.2016.11.2228

98. Brunnström H, Johansson A, Westbom-fremer S, Backman M, Djureinovic D, Patthey A, et al. PD-L1 immunohistochemistry in clinical diagnostics of lung cancer : inter-pathologist variability is higher than assay variability. Nat Publ Gr [Internet]. 2017;30(10):1411–21. Available from: http://dx.doi.org/10.1038/modpathol.2017.59

99. Rimm DL, Han G, Taube JM, Yi ES. A prospective, multi-institutional assessment of four assays for PD-L1 expresssion in NSCLC by immunohistochemistry. JAMA Oncol. 2017;3(8):1051–8.

100. Althammer S, Tan TH, Spitzmüller A, Rognoni L, Wiestler T, Herz T, et al. Automated image analysis of NSCLC biopsies to predict response to anti-PD-L1 therapy. J Immunother Cancer. 2019;7(1):1–12.

101. Tsao MS, Kerr KM, Kockx M, Beasley M, Borczuk AC, Botling J, et al. PD-L1 Immunohistochemistry Comparability Study in Real-Life Clinical Samples : Results of Blueprint Phase 2 Project. J Thorac Oncol [Internet]. 2018;13(9):1302–11. Available from: https://doi.org/10.1016/j.jtho.2018.05.013

102. Fehrenbacher L, Spira A, Ballinger M, Kowanetz M, Vansteenkiste J, Mazieres J, et al. Atezolizumab versus docetaxel for patients with previously treated non-small-cell lung cancer (POPLAR): a multicentre , open-label , phase 2 randomised controlled trial. Lancet [Internet]. 2016;387(10030):1837–46. Available from: http://dx.doi.org/10.1016/S0140-6736(16)00587-0

103. Mcnamara G, Difilippantonio M, Ried T, Bieber FR. Microscopy and Image Analysis. 2017;(July):1–89.

104. Waters JC. Accuracy and precision in quantitative fluorescence microscopy. 2009;185(7):1135–48.

105. Adan A, Alizada G, Kiraz Y, Baran Y, Nalbant A, Baran Y, et al. Critical Reviews in Biotechnology Flow cytometry : basic principles and applications. 2017;8551.

106. Pateria A, Vyas V, Minu MS. Enhanced Image Capturing using CNN. 2019;(April).

107. Gong C, Anders RA, Zhu Q, Taube JM, Green B, Cheng W, et al. Quantitative Characterization of CD8+ T Cell Clustering and Spatial Heterogeneity in Solid Tumors. Front Oncol. 2019;8(January):1–14.

108. Portland F, Toronto G, Madrid C, Nijmegen UK, Medicine T. Cancer classification using the Immunoscore : a worldwide task force Cancer classification using the Immunoscore : a worldwide task force.

109. December N, Galon J, Lugli A, Bifulco C, Pages F, Masucci G, et al. World - Wide Immunoscore Task Force : meeting report from the " Melanoma Bridge ",. J Transl Med. 2017;1–8.

110. Tosolini M, Camus M, Berger A, Wind P, Lagorce-page C. References and Notes 1. 2006;313(September):1960–5.

111. Taube JM, Anders RA, Young GD, Xu H, Sharma R, Mcmiller TL, et al. Taube_2012_SciTranslatMed_Clin.pdf. 2013;4(127):1–22.

112. Duan J, Xie Y, Qu L, Wang L, Zhou S, Wang Y, et al. A nomogram-based immunoprofile predicts overall survival for previously untreated patients with esophageal squamous cell carcinoma after esophagectomy 11 Medical and Health Sciences 1107 Immunology. J Immunother Cancer. 2018;6(1):1–15.

113. Berry S, Danilova L, Cheever M, Stein JE, Ramchurren N, Yearley JH, et al. Multidimensional, quantitative assessment of PD-1/PD-L1 expression in patients with Merkel cell carcinoma and association with response to pembrolizumab. J Immunother Cancer. 2018;1–11.

114. Mazzaschi G, Madeddu D, Falco A, Bocchialini G, Goldoni M, Sogni F, et al. Low PD-1 expression in cytotoxic CD8 þ tumor-Infiltrating lymphocytes confers an immune-privileged tissue microenvironment in NSCLC with a prognostic and predictive value. Clin Cancer Res. 2018;24(2):407–19.

115. Chang YH, Heo YJ, Cho J, Song SY, Lee J, Kim KM. Computational measurement of tumor immune microenvironment in gastric adenocarcinomas. Sci Rep. 2018;8(1):1–8.

116. Johnson DB, Bordeaux J, Kim JY, Vaupel C, Rimm DL, Ho TH, et al. Quantitative spatial profiling of PD-1/PD-L1 interaction and HLA-DR/IDO-1 predicts improved outcomes of anti-PD-1 therapies in

metastatic melanoma. Clin Cancer Res. 2018;24(21):5250–60.

117. Liu P, Xiao Q, Zhou B, Dai Z, Kang Y. Prognostic Significance of Programmed Death Ligand 1 Expression and Tumor-Infiltrating Lymphocytes in Axial Osteosarcoma. World Neurosurg [Internet]. 2019; Available from: https://doi.org/10.1016/j.wneu.2019.05.121

118. Gros A, Robbins PF, Yao X, Li YF, Turcotte S, Tran E, et al. PD-1 identi fi es the patient-speci fi c in fi ltrating human tumors. J Clin Invest. 2014;124(5):2246–59.

119. Lin J, Long J, Wan X, Chen J, Bai Y, Wang A, et al. Classification of gallbladder cancer by assessment of CD8+ TIL and PD-L1 expression. BMC Cancer. 2018;18(1):1–10.

120. Dakos V, Matthews B, Hendry AP, Levine J, Loeuille N, Norberg J, et al. Ecosystem tipping points in an evolving world. Nat Ecol Evol. 2019;3(3):355–62.

121. Faget L. Tyramide Signal Amplification for immunofluorescent enhancement. In:Hnasto R. (ed) ELISA. Hnasko R. Protocols S, editor. New York.: Humana Press, New York; 2015. 1318 p.

122. Zhang W, Hubbard A, Jones T, Racolta A, Bhaumik S, Cummins N, et al. Fully automated 5-plex fluorescent immunohistochemistry with tyramide signal amplification and same species antibodies. Nat Publ Gr [Internet]. 2017;97(7):873–85. Available from: http://dx.doi.org/10.1038/labinvest.2017.37

123. Anyaegbu CC, Lee-Pullen TF, Miller TJ, Abel TN, Platell CF, McCoy MJ. Optimisation of multiplex immunofluorescence for a non-spectral fluorescence scanning system. J Immunol Methods. 2019;

124. Valm AM, Oldenbourg R, Borisy GG. Multiplexed Spectral Imaging of 120 Different Fluorescent Labels. 2016;1–17.

125. Rth ANO, Hosh RING, Ilson EMMARW, Imothy T, Oughney D, Rown HAB, et al. Super-multiplexed fluorescence microscopy via photostability contrast. 2018;9(7):2943–54.

126. Anyaegbu CC, Lee-Pullen TF, Miller TJ, Abel TN, Platell CF, McCoy MJ. Optimisation of multiplex immunofluorescence for a non-spectral fluorescence scanning system. J Immunol Methods. 2019;

127. Stack EC, Wang C, Roman KA, Hoyt CC. Multiplexed immunohistochemistry, imaging, and quantitation: A review, with an assessment of Tyramide signal amplification, multispectral imaging and multiplex analysis. Methods [Internet]. 2014;70(1):46–58. Available from: http://dx.doi.org/10.1016/j.ymeth.2014.08.016

128. Widmaier M, Wiestler T, Walker J, Barker C, Scott ML, Sekhavati F, et al. Comparison of continuous measures across diagnostic PD-L1 assays in non-small cell lung cancer using automated image analysis. Mod Pathol [Internet]. 2019; Available from: http://dx.doi.org/10.1038/s41379-019-0349-y

129. Metaxas Y, Rivalland G, Mauti LA, Klingbiel D, Kao S, Schmid S, et al. Pembrolizumab as Palliative Immunotherapy in Malignant Pleural Mesothelioma. J Thorac Oncol [Internet]. 2018;13(11):1784–91. Available from: http://www.sciencedirect.com/science/article/pii/S1556086418309651

130. Peranzoni E, Lemoine J, Vimeux L, Feuillet V, Barrin S. Macrophages impede CD8 T cells from reaching tumor cells and limit the efficacy of anti – PD-1 treatment. 2018;115(17):4041–50.

131. Langer CJ, Gadgeel SM, Borghaei H, Papadimitrakopoulou VA, Patnaik A, Powell SF, et al. Carboplatin and pemetrexed with or without pembrolizumab for advanced , non-squamous non-small-cell lung cancer : a randomised , phase 2 cohort of the open-label KEYNOTE-021 study. Lancet Oncol [Internet]. 2016;17(11):1497–508. Available from: http://dx.doi.org/10.1016/S1470-2045(16)30498-3

132. Kamphorst AO, Pillai RN, Yang S, Nasti TH, Akondy RS, Wieland A. Proliferation of PD-1 + CD8 T cells in peripheral blood after PD-1 – targeted therapy in lung cancer patients. 2020;114(19):4993–8.

133. Riaz N, Wolden SL, Gelblum DY, Eric J. HHS Public Access. 2016;118(24):6072–8.

134. Fumet J, Richard C, Ledys F, Klopfenstein Q, Joubert P, Routy B, et al. Prognostic and predictive role of CD8 and PD-L1 determination in lung tumor tissue of patients under anti-PD-1 therapy. Br J Cancer [Internet]. 2018;(July). Available from: http://dx.doi.org/10.1038/s41416-018-0220-9

135. Jiang T, Shi J, Dong Z, Hou L, Zhao C, Li X, et al. Genomic landscape and its correlations with tumor mutational burden , PD-L1 expression , and immune cells infiltration in Chinese lung squamous cell carcinoma. 2019;1:1–13.

136. Koh J, Ock C-Y, Kim JW, Nam SK, Kwak Y, Yun S, et al. Clinicopathologic implications of immune classification by PD-L1 expression and CD8-positive tumor-infiltrating lymphocytes in stage II and III gastric cancer patients. Oncotarget. 2017;8(16):26356–67.

137. Heikal A. Intracellular coenzymes as natural biomarkers for metabolic activities and mitochondrial anomalies. Biomark Med. 2011;4(2):241–63.